Indirect imaging of AM Herculis-stars

vorgelegt von
Diplom-Physiker
Andreas Staude
aus Berlin

Von der Fakultät II – Mathematik und Naturwissenschaften
der Technischen Universität Berlin
zur Erlangung des akademischen Grades

Doktor der Naturwissenschaften
– Dr. rer. nat. –

genehmigte Dissertation

Promotionsausschuß:

Vorsitzender: Prof. Dr. A. Hese
Berichter: PD Dr. A. Schwope
Berichter: Prof. Dr. E. Sedlmayr

Tag der wissenschaftlichen Aussprache: 28. November 2005

Berlin 2005
D 83

Zusammenfassung

AM Herculis-Sterne sind enge Doppelsterne, die aus einem weißen Zwerg mit starkem Magnetfeld und einem Hauptreihenstern bestehen. Letzterer verliert Materie an den weißen Zwerg, wobei das Magnetfeld die Materie zu den Magnetpolen leitet, wo die freigesetzte potentielle Energie abgestrahlt wird – hauptsächlich als Röntgen- und UV-Strahlung. Diese Doppelsternsysteme sind so klein, daß sie mit derzeitigen Instrumenten nicht räumlich aufgelöst beobachtet werden können.

Indirekte bildgebende Verfahren können Informationen rekonstruieren, die in Beobachtungsdaten nur noch als Projektionen in einen Unterraum existieren. Solche tomographischen Verfahren kennt man aus der Medizin, aber sie können auch auf astronomische Daten angewandt werden, wenn eine Reihe von Messungen als Ansichten des selben Systems unter verschiedenen Blickwinkeln interpretiert werden kann.

In dieser Arbeit werden zeitaufgelöste Spektren von AM Herculis-Sternen mit tomographischen Methoden analysiert. Spektrallinien mit Ursprung in den verschiedenen Bestandteilen der Systeme sind deutlich sichtbar Doppler-verschoben. Die Doppler-Verschiebung ist abhängig vom Blickwinkel auf die Rotationsachse des Systems und verändert sich mit der Phase des Bahnumlaufs.

Mit Zeitreihen von eindimensionalen Daten (Spektren) können zweidimensionale Intensitätskarten in Geschwindigkeitskoordinaten (Doppler-Tomographie) oder Karten des Linienflusses auf der angenommenen Oberfläche des Hauptreihensterns (Roche-Tomographie) aus der Veränderung des Linienprofils errechnet werden. Die Orbitalvariation der Linien mit Ursprung auf dem Hauptreihenstern ist abhängig von wesentlichen Parametern des Systems: dem Bahnneigungswinkel und den Massen der Sterne. Benutzt man eine Maximum-Entropie-Methode zur Erzeugung der Karten, kann die für verschiedene Parameterkombinationen zum Schluß erreichte Entropie dazu benutzt werden, die wahrscheinlichsten Werte zu ermitteln.

Beide tomographischen Methoden wurden auf optische Spektren zweier AM-Herculis-Sterne angewandt – AM Her selbst und QQ Vul.

Für die Roche-Tomographie wurde ein Programm benutzt („AStRoTom“), das zur Optimierung Evolutionsstrategie verwendet und von mir geschrieben wurde. Für gegebene Systemparameter konnte das Programm Intensitätskarten der Emissions- und Absorptionslinen, die auf den Hauptreihensternen entstehen, erzeugen. Versuche der genaueren Bestimmung der Systemparameter für

beide Objekte führten zu keiner Verbesserung der schon veröffentlichten Werte. Wahrscheinlich ist die Qualität der Beobachtungsdaten dafür zu gering.
Durch Doppler-Tomographie von Emissionslinien konnten detaillierte Karten der Verteilung des Linien-Flusses in den Systemen erzeugt werden. Im Falle von AM Her zeigen die Karten (und auch die Spektren) deutliche Veränderungen von Nacht zu Nacht. Die Art der Strukturen und die Geschwindigkeit ihrer Veränderung können nicht mit dem Standard-Modell des Roche-Volumen-„Überlaufens“ erklärt werden. Stattdessen wird ein Modell vorgeschlagen, in dem die Materie an einem anderen Punkt als dem Lagrange-Punkt den Hauptreihenstern verläßt, möglicherweise verbunden mit magnetischer Aktivität. Die Doppler-Karten von QQ Vul zeigen unterschiedliche Orte der Emissionsmaxima für die verschiedenen betrachteten Linien. Die Wasserstofflinien zeigen eine helle Komponente, die auf der röntgenbestrahlten Hemisphäre des Hauptreihensterns ensteht, und einen deutlich erkennbaren Akkretionsstrom. Das Verhalten der Heliumlinien ist komplizierter und kann am besten durch eine zusätzliche Energiequelle für die Anregung der Linien in der Region, in der der frei fallende Materiestrom vom Magnetfeld eingefangen wird, erklärt werden. Besonders im Falle der Linie des ionisierten Heliums kann Bestrahlung als Hauptursache der Anregung ausgeschlossen werden.

Abstract

AM Herculis stars (or 'polars') are close binaries consisting of a white dwarf with a strong magnetic field and a main sequence star (the 'secondary') which is losing mass to the white dwarf. The magnetic field channels the matter to the magnetic poles, where the released potential energy is radiated away – mainly in X-rays and the UV. The spatial structure of these objects cannot be observed directly, because their apparent size is too small.

Indirect imaging methods are capable of restoring information which is only contained in observational data as projections onto a sub-space. These tomographic methods are known from medicine, but can also be applied to astronomical data, when a number of measurements can be regarded as views of the same object under different aspect angles.

In this work tomographic methods are applied to time-resolved spectroscopic data of polars. Spectral lines seen in the radiation emitted by the constituents of these systems are notably Doppler-shifted. The Doppler-shift is depending on the viewing angle of the system ('inclination') and is varying with orbital phase.

Time-series of one-dimensional data (spectra) can be used to create a two-dimensional map of the intensity distribution in velocity-space (Doppler-tomography), or a map of the line-flux on the assumed surface of the mass-losing star (Roche-tomography) from the line profile changes. The orbital variation of lines originating on the secondary is strongly depending on the main system parameters, inclination and the stars' masses. Using a Maximum-Entropy-Method for the creation of the maps, the final entropy of reconstructions with differing parameter combinations allows to determine the most probable values.

Both indirect imaging methods are applied to optical spectra of two polars – AM Her and QQ Vul.

For Roche-tomography, AStRoTom, a code invoking Evolution Strategy for the optimisation written by me, was used. For given system parameters, intensity maps of emission and absorption lines arising on the secondaries were calculated. The determination of the system parameters lead to no improvement of previously published values for both, AM Her and QQ Vul. The reasons for this are most probably the too low quality of the input data.

Doppler-tomography of the emission lines lead to detailed maps of the line-flux distribution in the systems. For AM Her, the maps (and also the spectra) show strong variations from night to night. The structures seen, and the speed of variation, cannot be explained with the standard model of Roche-lobe overflow. Instead a model is suggested, in which the matter is streaming-off at a different location on the secondary's surface than the L_1, probably connected with magnetic activity of the star. The Doppler-maps of QQ Vul show different locations for the emission maxima of the considered lines. The hydrogen lines have a strong component arising on the secondary's X-ray-irradiated hemisphere and a clearly detected accretion stream. The behaviour of the helium lines is more complicated and can best be explained by an additional energy source for excitation of the lines in the region where the ballistically moving matter is captured by the magnetic field of the white dwarf. Especially for the lines of ionised helium, irradiation can be ruled out as the major source of excitation.

Contents

Chapter 1

Introduction

Cataclysmic variable stars (CVs) are close binary stars consisting of a white dwarf and a main sequence star. Both stars are so close to each other, that matter is transferred from the main sequence star to the white dwarf. The potential energy of the matter being accreted is set free as radiation. In the case of polars – a sub-class of CVs, in which the motion of the matter is dominated by the magnetic field of the white dwarf – a large fraction of the released energy ($L_{acc} \sim 10^{33}\,\mathrm{erg\,s^{-1}}$) is emitted in the X-ray and UV regime.

CV systems are very small – with an orbital separation of the order of the solar radius – and further away than to be able to obtain spatially resolved images. In the emitted light, the constituents of the systems can be traced in their Doppler-shifted spectral lines. This is possible because of the vastly differing excitation conditions caused partly by the irradiation with high-energy photons, and the time-dependency of the Doppler-shift. Information on the spatial structure can thus be obtained from time-resolved spectra by indirect imaging methods.

In this work I present data obtained in a coordinated campaign in August 2000, using the Calar Alto 3.5m-telescope for time-resolved spectroscopy, and the 70cm-telescope of the AIP for simultaneous photometry. Two objects were observed: AM Her, the prototype of a subclass of CVs called polars, and another member of this group, QQ Vul.
In the following, I first give an introduction to CVs with the focus on polars, and to indirect imaging techniques. Afterwards I describe the techniques I utilised for the analysis of the spectroscopic data – Doppler- and Roche-tomography – in detail.
The data and the results obtained from them are shown and discussed. Concluding remarks close this work.

1.1 Polars – a sub-class of cataclysmic variable stars

1.1.1 The standard model of CVs

Polars, which are also called AM Herculis stars (after the prototype), form a subclass of the cataclysmic variables (CVs). CVs are close binary stars, consisting of a white dwarf and a companion star, which loses mass to the white dwarf. This companion is in most cases a late-type main-sequence star, but also evolved stars are present, e.g. a helium star – the core of a former red giant – in the case of AM CVn. The source of mass transfer is in the standard model explained as Roche-lobe over-flow by the companion, the so-called secondary star. This Roche lobe is the volume inside the smallest equipotential-surface enclosing both stars, inside which the attraction from the secondary is higher than the one of the white dwarf (Fig. 1.1, left panel).

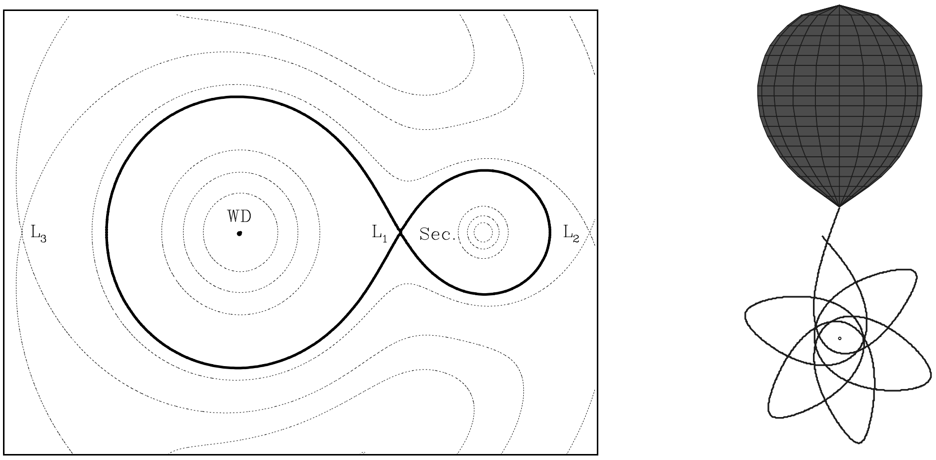

Figure 1.1: *left*: Equipotential surfaces in the orbital plane of two rotating point-sources (kindly provided by Matthias Schreiber). The Roche-lobe is defined by the equipotential surface consisting L_1. *right*: The trajectory of a free-falling particle in the potential of two rotating point-sources, starting with $v_0 \simeq 0$ at the L_1 – the ballistic trajectory (view from above, truncated after a limited time). The system is rotating counter-clockwise.

The potential in kartesian coordinates in the co-rotating frame is given by Eq. (1.1), and consists of the gravitational potentials of two mass-points and the coriolis force.

$$\Phi = -\frac{GM_1}{\sqrt{x^2+y^2+z^2}} - \frac{GM_2}{\sqrt{(x-a)^2+y^2+z^2}} - \frac{1}{2}\Omega_{orb}^2[(x-\mu a)^2+y^2] \quad (1.1)$$

(With $\mu = M_2/(M_1+M_2)$ and $\Omega_{orb}^2 = \frac{G(M_1+M_2)}{a^3} = (\frac{2\pi}{P})^2$. a is the distance between the two stars with masses M_1 and M_2. P is the orbital period, and G the gravitational constant.)

The overflowing matter originating from the secondary gets under the influence of the white dwarf. The current model of CVs assumes the matter streaming-off over the Lagrange point one (L_1), the minimum of the potential between the two stars. The matter being accreted is expected to have an initial velocity of roughly the sound speed in the gas, $\sim 10\,\mathrm{km/s}$. (There are hints that other mechanisms of mass transfer like stellar winds may also play a role.) After crossing the L_1, the motion of the matter is dominated by the white dwarf's gravitation. The accreted matter follows a ballistic trajectory which does not intercept the white dwarf because of the coriolis-force (Fig. 1.1, right panel).

According to the literature, two extreme scenarios are possible now:

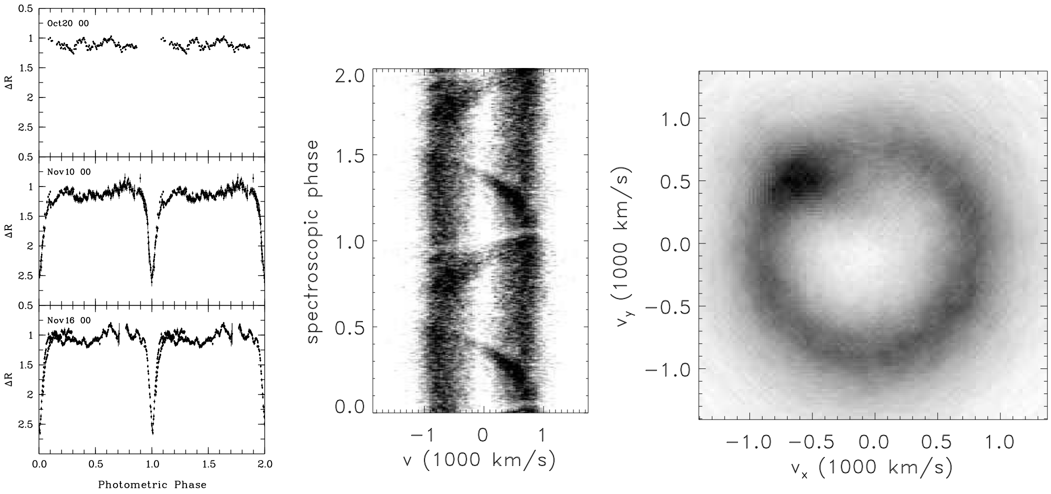

Figure 1.2: Observational evidence for accretion disks in CVs: *left*: Light curves of the eclipsing system HS0455+8315 (see Gänsicke et al., 2002), obtained with the AIP 70cm-telescope: The highly symmetric eclipse, which doesn't have a flat bottom, is a signature of a partially obscured accretion disk. The accretion disk is similarly bright at different orbital phases, causing the low level of variability outside the eclipse. Shortly before the eclipse the system becomes a little bit brighter. Then the region where the ballistic stream hits the rim of the accretion disk is best visible. *middle*: Trailed spectrum around Hα and Doppler tomogram (*right*) of the disk-system WZ Sge (from Spruit and Rutten, 1998) The double-peaked line profile is a clear signature of an accretion disk and transforms to the ring in the Doppler-map (see 2.1.2). The sinosoidal component in the spectrum arises from the impact region of the ballistic stream in the accretion disk and transforms to the bright spot in the tomogram. The ballistic stream is not visible, because the accretion disk is emitting much stronger and is also shielding the stream from irradiation.

If the accreted matter is not ionised, or the magnetic field of the white dwarf is not strong enough to force the matter to move along magnetic field lines, the matter-density in the white dwarf's Roche-lobe is increasing, at some point leading to non-negligible friction. This forces the matter to exchange momentum, until (most of) the matter is rotating around the primary at a constant radius determined by the angular momentum of the matter at L_1, the circularisation radius.

Due to the friction, exchange of angular momentum is now possible, leading to matter loosing angular momentum, thus falling onto the white dwarf, and matter gaining it, allowing it to leave the binary system. This constellation is called an accretion disk. Accretion disks leave clear signatures in optical light curves and time resolved spectra (Fig. 1.2). The optical broad-band light-curves are dominated by continuum emission from the accretion disk. The most prominent spectral lines are those of the hydrogen Balmer-series in emission.

In the case of polars, the matter is ionised and the white dwarf has a strong magnetic field. At one point the ram-pressure of the accretion stream is outrun by the magnetic pressure and thus the matter is forced to move along the magnetic field-lines until it hits the white dwarf near a magnetic pole (Fig. 1.3). The line profiles of emission lines from polars don't show any signature of an accretion disk. Instead the accretion stream is clearly seen. In some cases the ballistic and magnetic parts could be identified. In optical spectra also secondary stars are detected, both in absorption lines from the undisturbed far hemisphere and in emission lines from the irradiated one (see Fig. 1.6).

The broad-band light-curves in the optical regime are dominated by continuum and line emission from the accretion stream, and by cyclotron radiation from the accretion column. Thus the light-curves are much more irregular than in the case of disk-systems.

This is, of course, a strongly simplified model. First of all, the magnetic field of the primary will be deviating from a dipolar shape, so that probably there are not just two accreting poles. Further, the model with magnetic and ram-pressure works for single particles without interaction only. The real physical situation is more complex: Caused by the magnetic pressure, the stream may fragment into blobs, in which electric currents can shield the effects of the magnetic field, at least until the magnetic pressure exceeds a certain value. Depending on their size, the blobs will be forced to follow the magnetic field lines from different points on. The physical processes in the coupling region are still not understood well. A magneto-hydrodynamic model is required but not yet available.

Anyway, the interaction between the matter and the magnetic field somehow happens, and the falling matter, consisting of blobs and 'normal' gas, is focussed onto small regions, where the magnetic field is strongest. The kinetic energy of the stream is set free when it either penetrates the white dwarf surface and heats it in the case of the dense blobs, due to a shock-front forming in the so-called accretion column (the dense, decelerated matter just above the white dwarf) or by cylotron radiation from fast electrons.

The shock-front leads to the emission of hard X-rays, whereas the heating of the primary's surface by penetrating matter to temperatures of the order of $\gtrsim 10^5\,\mathrm{K}$ results in emitted soft X-rays and UV photons. These high-energy

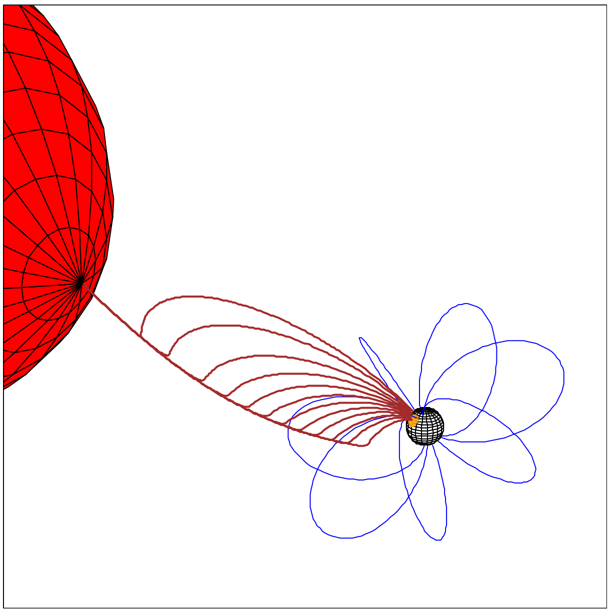

Figure 1.3: Schematic view of a polar, showing the Roche-lobe filling secondary, the stream of the accreted matter, starting at L_1 and coupling onto different magnetic field-lines later, and the white dwarf with the hot accretion spot.

photons are ionising and heating the matter being accreted, and, when hitting the secondary star, are changing the temperature structure of the irradiated hemisphere, leading to the formation of emission lines instead of the absorption features typical for late-type stars. Magnetic CVs can clearly be identified by the presence of emission lines of He II with a line flux comparable to the one in Hα and Hβ. Contrary to the non-magnetic CVs, the accretion spot emits UV photons with an energy high enough to ionise the helium atoms.

Because of tidal interactions, the rotation of the secondary is expected to be synchronised with its orbital motion. In the case of the polars, the strong magnetic field of the primary is thought to lead to a synchronisation of its rotation with the orbit as well, because of the interaction with a likely magnetic field of the secondary.

The two cases described so far can be considered the extrema of a dominating or negligible magnetic field. In-between, the existence of the magnetic field can disturb the formation of an accretion disk by disrupting the ballistic stream but not being able to capture the matter completely. Or the magnetic field of the primary is not strong enough to enforce the synchronisation of its rotation with the orbital motion, leading to a fast-rotating white dwarf inside an accretion disk, which accretes via a so-called accretion curtain. These objects in-between the extrema are called intermediate polars (IPs, or DQ Herculis stars).

1.1.2 Mass transfer and evolution

The amount of energy released during the accretion process is the kinetical energy gained by the matter when falling from the L_1 onto the white dwarf, which can be estimated by falling from infinity:

$$L_{acc} \approx \frac{GM_1\dot{M}}{R_{wd}}, \tag{1.2}$$

with L_{acc} being the luminosity of the accretion spot, G the gravitational constant, M_1 the mass of the white dwarf, and R_{wd} the latter's radius. $\dot{M}$ is the accretion rate.

In CVs the mass transfer occurs on a level low enough to be possible for a long time ($\dot{M} \sim 10^{-13}..10^{-10}\,M_\odot/yr$), so that the probability to observe such a system is not vanishing, and it is large enough to set free the necessary amount of radiation to make it distinguishable from non-accreting binaries.

To allow (pseudo)-stable mass transfer, the accretor has to be more massive than the donor (mass ratio $Q = M_1/M_2 \gtrsim 1$). In this case the accreted matter moves to a point closer to the center of mass, leading to a reduced angular momentum. But angular momentum is conserved in an isolated system. Thus the stars move further away from each other to obey this law. This causes the accretion process to stop, because now the volumes of the Roche-lobes are larger, and the secondary is no longer over-filling his part.

To keep a CV running, angular momentum has somehow to be expelled from the system. Two mechanisms to do this are considered currently: magnetic breaking and gravitational radiation.

Magnetic breaking is thought to be caused by stellar wind arising from the secondary star. This stellar wind consists of charged particles which interact with magnetic fields. If the magnetic field of the secondary is strong enough, it forces the particles to co-rotate with it while moving outwards. They thus gain angular momentum which will be lost for the secondary's spin. But the secondary's spin is locked to the orbital motion, so the energy is supplied by the latter one. Particle winds could also be arising from an accretion disk or from the white dwarf, but normally these are not considered for angular momentum losses.

Gravitational radiation arises – according to the theory of General Relativity – when two masses orbit each other. The energy for the gravitational wave is taken from the orbital motion.

The accretion rates which can be reached with the two mechanisms are estimated as

$$\dot{M}_{\rm mag} = 2.0 \times 10^{-11}\; P_{\rm orb}^{3.7}\,({\rm h})\; M_\odot\;{\rm yr}^{-1}\;(P_{\rm orb} > 2.7\,{\rm h}) \tag{1.3}$$

(McDermott and Taam, 1989),

$$\dot{M}_{\mathrm{grav}} = 2.4 \times 10^{15} \, \frac{M_1^{2/3} \, (M_\odot) \; P_{\mathrm{orb}}^{-1/6}(\mathrm{h})}{(1 - \frac{15}{19}\, q)(1+q)^{1/3}} \; \mathrm{g \; s^{-1}} \; (P_{\mathrm{orb}} \lesssim 9\,\mathrm{h}) \qquad (1.4)$$

(Warner, 1995, Eq. (9.20); $q = M_2/M_1$).

For a system with $P_{\mathrm{orb}} = 3\,\mathrm{h}$, $Q = M_1/M_2 = 1.75$, $M_1 = 0.5\mathrm{M}_\odot$ both values are equal at a value of $\dot{M} \sim 5 \times 10^{-10} M_\odot/\mathrm{yr}$. For longer orbital periods the angular momentum loss by magnetic braking is much larger, dominating the effects of gravitational radiation. For smaller orbital periods the contribution of magnetic braking to the angular momentum loss becomes negligible. (The value of angular momentum loss by gravitational radiation depends only weakly on the orbital period.)

When inspecting the distribution of orbital periods, a region with a reduced number of CVs is seen in the range between 2 and 3 hours – the so-called 'period gap'. The explanation for the 'period gap' is that the mechanism of magnetic braking becomes ineffective when the CVs are evolving to $M_2 \sim 0.3$ and thus becoming fully convective. This corresponds to an orbital period of $P_{\mathrm{orb}} \sim 3\,\mathrm{h}$. The M-star at this point is considered to have been out of thermal equilibrium due to the accretion process, and is now approaching it again. This causes the star to shrink, so that no mass-overflow happens during the time when gravitational radiation reduces P from 3 to 2 h. Around $P \sim 2\,\mathrm{h}$ the star fills its Roche-lobe again, and the mass transfer is continued with the rate supplied by gravitational radiation.

Nowadays there is discussion, whether this 'gap' really exists or what other mechanisms could cause it, the measured activity of single M-stars didn't show a discontinuity when becoming fully convective. The amount of angular momentum loss given by the equations above is also questioned, so that other mechanisms for creating the period gap have to be considered (see e.g. Andronov and Pinsonneault, 2004).

Another possibility for stable mass-transfer would be given when the secondary star evolves into a red giant. This would cause its radius to grow and thus always being able to fill its growing Roche-lobe. But the secondary stars in CVs are mostly of very late type (M), which stay longer on the main sequence than the universe is old according to current theories.

However, there are publications which report on secondary stars, which fill a much larger Roche-lobe than it should be possible for a main-sequence star with the observed spectral type. Causes for this discrepancy can be that heavy elements have been transported from the primary to the secondary in the past – during its giant phase – or that the mass-radius-relation for main-sequence stars doesn't apply to gravitationally disturbed stars.

If the mass ratio Q were below one, the mass transfer would be catastrophic, because the accreted matter would gain angular momentum by moving from the heavier donor star (which is closer to the center of mass) to the accretor. Thus the separation and the size of the Roche-lobes would shrink, leading to faster accretion. Although such objects are possible, the chance of finding one would be rather low, because of their short life-time.

CVs are thought to form out of binaries with a distance of a few hundred solar radii. The orbital period is of the order of 10 years. One star has to be heavier than $1\,\mathrm{M}_\odot$, the other one lighter. At the end of the main-sequence phase the heavier star evolves into a red giant, which will at some point fill its Roche-lobe. Further expansion will result in mass transfer to the lighter companion and thus to a reduction of the binary separation. The resultant catastrophic mass transfer will soon fill the Roche-lobe of the companion star, but the matter cannot be accreted because the mass transfer is much faster than to allow thermal equilibrium to be reached. The matter will thus overflow both Roche-lobes, forming a 'common envelope' of both stars. In this common envelope the friction will transfer angular momentum from the orbital energy of both stars to the surrounding matter, causing the distance of both stars to shrink and the surrounding matter to gain enough energy to escape the system and to form a planetary nebula. On a time-scale of 1000 years the binary separation will be reduced to $\sim 1\,\mathrm{R}_\odot$, and the primary star will have lost most of its atmosphere, leaving a white dwarf.

If the binary separation is small enough, a CV is the result. Otherwise a detached binary has formed, which may evolve to a CV by angular momentum loss due to magnetic braking or gravitational radiation.

Those CVs with a main-sequence star as companion to the white dwarf are found with orbital periods between $\sim 12\,\mathrm{h}$ and $\sim 78\,\mathrm{min}$. These upper and lower limits are explained by evolutionary arguments: For orbits longer than $\sim 12\,\mathrm{h}$, the main-sequence secondaries cannot fill their Roche-lobe, so accretion is impossible. The lower limit is thought to originate from the special behaviour of degenerate stars: While approaching the white dwarf, the secondary has lost most of its matter and is in a degenerate state. This means that it will become larger when it loses mass. By losing mass it will move further away from the white dwarf, which results in a longer orbital period, but still with mass transfer.

Over-all, there are more than 1000 known CVs. The orbital periods range from less than half an hour (AM CVn, with a helium secondary) to 460 days (RS Oph, with a red giant as companion).

Most Cataclysmic Variables are disk systems. Polars form only a small fraction of the CVs, ~ 80. They have orbital periods of 78 to 480 minutes. For some systems the magnetic field strength was determined. It is in the range between 7 and 230 MG (Schwope, 2000).

The number of known IPs is even lower – only $\sim$ 23 are known today (see e.g. the compilation of K. Mukai at *http://lheawww.gsfc.nasa.gov /users/mukai/iphome/iphome.html*).

1.1.3 The emitted radiation

The name 'cataclysmic variables' (*kataklysmos* (greek) = diluvian, the flood connected with the story of Noah in the Bible) originates from the drastic brightness variations which were observed in CVs as (dwarf-) novae.
When the technology improved, observations of the stars which were detected during a nova revealed their binary nature (e.g. DQ Her, the Nova Her 1934, Walker, 1954). Other CVs, like AM Her, were discovered as variable stars in photographic plate surveys. Their binary nature was revealed later by spectroscopy. New CVs are found as X-ray sources, as optically variable stars, as blue objects in blue-excess surveys, and as emission-line objects in Quasar surveys.

The light curves and spectra of polars are highly complex, which can be understood when considering the origin of light in these systems (see Fig. 1.4): The two stars contribute the spectra of a white dwarf and a late-type dwarf,

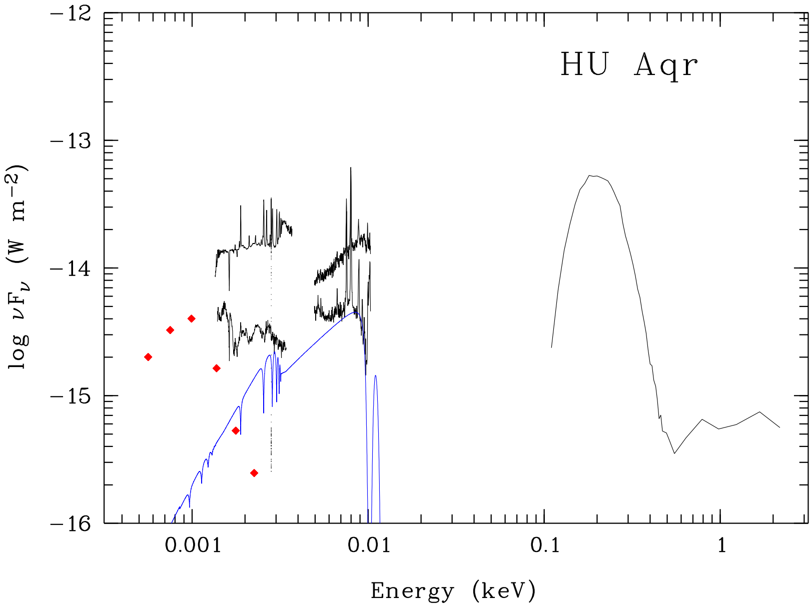

Figure 1.4: Spectral energy distribution of a polar (HU Aqr, from Schwope 2000). The black lines show observational data, in the optical (< 0.004 keV), the UV (0.005..0.01 keV), and in the X-ray regime (above 0.1 keV). In the visual range, spectra obtained during a high and a low accretion state are plotted, the UV spectra were taken at orbital bright and faint phase during an intermediate accretion state, the X-ray data are from the orbital bright phase during a high state. The blue line shows the modelled contribution from the white dwarf, the red dots the flux level of the secondary star.

where the latter one may be partly irradiated and thus emitting a different spectrum on the irradiated hemisphere. The accreted matter has a certain temperature and is additionally irradiated, thus emitting continuum and line emission of both, neutral and ionised species. Near the white dwarf surface

the velocity of the falling matter becomes high and the magnetic field strength increases, leading to cyclotron radiation from fast electrons. Further, there is the high-energy contribution from the accretion column and its surrounding material.
The shares of all these components on the over-all emission vary with the changes of visibility and projected areas of the emitting regions during the orbital cycle. This causes the light-curves of both, continuum and lines, to be highly variable in all wavelength regions (Fig. 1.5).

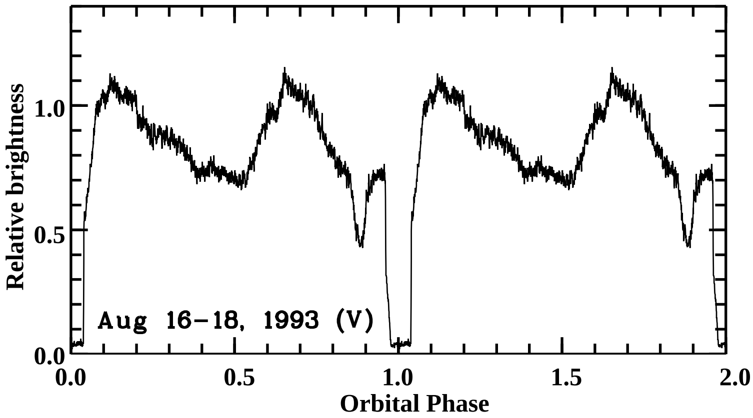

Figure 1.5: Light-curve of the eclipsing polar HU Aqr in V during a high accretion state (from Schwope et al., 2001): The data is phase folded on the orbital period and plotted twice, the brightness is calculated with respect to a $V = 14\overset{\mathrm{m}}{.}7$ comparison star. The deep eclipse around phase 0 is caused by the complete obscuration of the white dwarf and the accretion stream by the secondary star. The white dwarf enters the eclipse first (the rapid decrease in brightness at phase 0.95). The gradual decrease afterwards is caused by the accretion stream, which is obscured successively. The white dwarf leaves the eclipse first, the accretion stream later. The modulation outside the eclipse is dominated by cyclotron-beaming of the accretion region on the white dwarf. The dip at phase 0.87 is caused by the obscuration of the white dwarf by the magnetically guided accretion stream.

In the spectral lines of some polars the signatures of the secondary star and the accretion stream/curtain can be identified (Fig. 1.6).

Polars are not only variable due to changing aspects, but also intrinsically. On time-scales of a few orbital cycles or even within one orbit they can change their brightness by a few magnitudes (see e.g. the long-time light-curves of AM Her in Götz (1993) and Hessman et al. (2000), which show changes of up to $\sim$ 1 mag within one day and of more than 3 mag within a few days). Since there is no accretion disk in which the released energy can rise dramatically by enhanced viscosity due to a magneto-hydrodynamic instability, and the time the matter needs to reach the white dwarf is of the order of one orbit, these changes have to be variations of the accretion rate. In Fig. 1.4 one sees that during a low accretion state the main contributions to the optical continuum

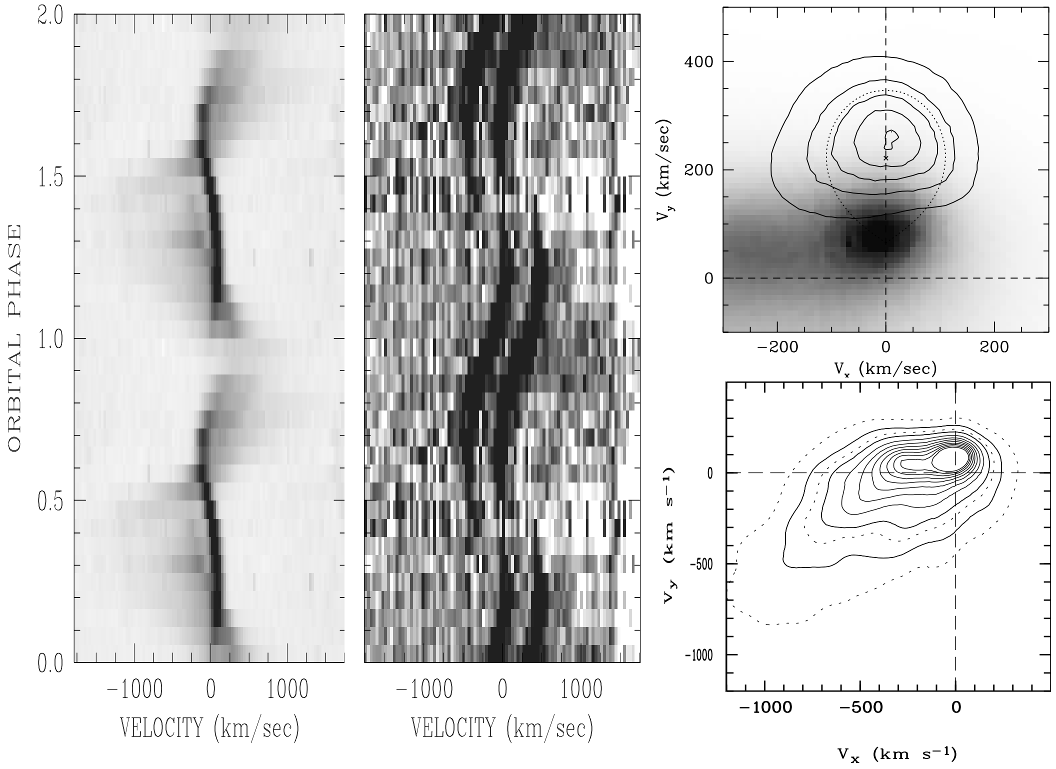

Figure 1.6: Time-resolved spectral line profiles of the polar QQ Vul (He II in emission (*left*) and Na I in absorption (*middle*)) and the resulting Doppler-tomograms (from Schwope et al., 2000). The brightest component of the emission line is the narrow emission line component (NEL). Additionally, there is emission with a higher velocity amplitude. The absorption lines have a higher velocity amplitude than the NEL and the brightness maxima and minima are shifted by ∼ 0.5 phases. The Doppler-tomograms (*right*, see 2.1.2) support the interpretation, that the NEL is arising at the irradiated hemisphere of the secondary star, while the absorption lines are originating from the unirradiated hemisphere. Orbital phase zero is *per definitionem* at lower conjunction of the secondary. In the tomogram on top the He II line emission is plotted as grayscale, while the absorption is plotted as contour lines. Overplotted is the calculated outline of the Roche-lobe for the assumed system parameters in velocity coordinates. The lower tomogram shows the He II emission in a larger velocity range as contour lines. From the position of the NEL there is a horizontal part of the stream at the expected position of the ballistic trajectory. Around $v_x \sim -300$ km/s the emission region bends down to the lower left quadrant, probably following the magnetically guided accretion stream.

flux are the ones from the two stars, while during a high state these are completely outshone by stream-emission end emission from the accretion spot.
Currently, the favoured explanation for accretion rate changes are magnetic fields on the secondary. Due to the short rotational period a dynamo could be powered. Also, at several single M-stars flares and coronal emission lines were detected, which are tracers of magnetic activity. Somehow there has to be a working dynamo, but there is no model yet for a dynamo in three dimensions,

which is necessary because of the highly asymmetric and fastly rotating star. The magnetic field could either redistribute the angular momentum within the secondary star, thus changing the orbital separation slightly. This would change the mass transfer rate until the angular momentum is distributed again as it was before, or until the system lost some of it due to magnetic braking. Or the magnetic field could result in star-spots with a reduced height of the photosphere within. Estimates performed for AM Her (Hessman et al., 2000) showed, that the stellar surface (at least near L_1) would have to be $\sim 50\,\%$ covered by star-spots, to be able to reproduce the observed long-term behaviour.

In the case of HU Aqr short flares were detected in optical photometry with high time-resolution (Schwope et al., 2004). During these flares, which last only for a few seconds, the system's brightness can be doubled. Because of their phasing – only outside the eclipse – and their shape, they are thought to be tracing single accretion events of dense blobs.

This section was only intended to give an overview about polars and is far from being detailed or complete. A good introduction to CVs in general is the book by Hellier (2001). A little bit older but covering all the knowledge available at the time of publication is the book by Warner (1995). Beuermann (1997) wrote a review article especially dealing with magnetic CVs. A compilation of articles concerning the latest developments and most pressing questions concerning CVs are the proceedings of the CV conference in Göttingen, 2000 (Gänsicke et al., 2002).

1.2 Indirect imaging

Objects like polars are very small (distance of both stars $R < 1R_\odot$) and far away (distance from the solar system $d \gtrsim 100\,\mathrm{pc}$), leading to an apparent size of

$$\arcsin(\tfrac{R}{d}) \approx 1\,\mu\mathrm{arcsec}$$

Thus it is impossible to get information on the system's spatial structure by direct imaging with the available instruments (resolution of HST ~ 0.05", theoretical value of VLTI ~ 0.0007").

But polars (and the other CVs) are rotating and their projection along the line-of-sight is – if the inclination angle is large enough – changing with orbital phase. By analysing the changes in the measured light, it is possible to get information about the system's intrinsic structure, like the shape of the accretion stream or the brightness distribution on the secondary's surface (star-spots). This is done by indirect imaging techniques.

Indirect imaging techniques make use of the fact that a structure in N dimensions can be reproduced from $(N-1)$-dimensional images taken from different viewing angles.

The principle is the same as in the medical Computer Tomography. There a number of X-ray images of a part of a human body are taken from different

perspectives. The gray-scale values in these images represent the absorption coefficient along rays parallel to the line-of-sight. The information from all the images is then combined to calculate a 3D model of the distribution of absorbers. The mathematical principle behind is the Radon Transform (Radon, 1917), which describes the calculation of the values of a function in multiple dimensions from its projections.
For CVs the data is the time-resolved measured light of the object. In the following I shortly describe the methods to analyse optical photometry and spectroscopy.

Indirect imaging using optical light-curves – Eclipse mapping

Light-curves of CVs can be used to determine the brightness distribution on an assumed system geometry.

For systems showing eclipses by the secondary star (either total or partial), one can determine the spatial positions of the emission regions by studying the shape of the eclipse profile, either in continuum or line emission. If a Roche-lobe-filling secondary is assumed, the exact shape and position of the eclipsing object is known for a set of system parameters.
The eclipsed parts of the system are not entering the eclipse at the same time, but are eclipsed successively, which gives information on their position perpendicular to the line-of-sight at eclipse ingress. At the end of the eclipse, the system is seen under a different viewing angle. The eclipsed parts will thus leave the eclipse differently from how they entered it (Fig. 1.7).

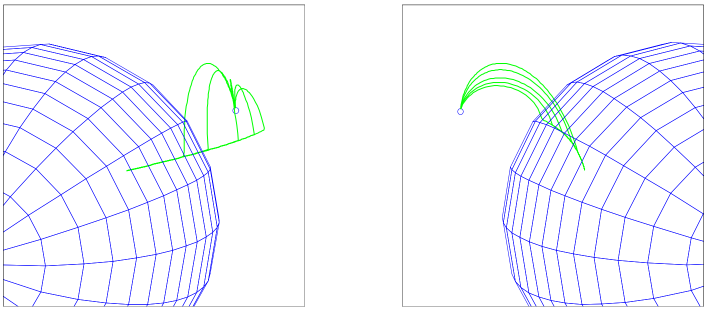

Figure 1.7: The situation for eclipse-mapping: A model-polar, shown at phases $\phi = -0.060$ (*left*) and $\phi = +0.068$.

With non-linear fitting algorithms one can try to find a model of the system, which is reproducing the observed light-curve. This approach is called 'eclipse mapping', and was first described by Horne (1985).
The drawback of this approach is that one has to assume an accretion geometry to map the intensity onto, because the number of free parameters of the model-system is much higher than can be determined by 1D-information like a light-curve.

A possible enhancement of this method is to use not only the eclipse data, but to model the shape of the light curve outside the eclipse as well.
In the case of disk-systems this is known as 'full-orbit eclipse mapping' (Kube, 2002).
For magnetic systems, different ways were chosen to restrict the mapped intensities to a stream-like structure ('Accretion Stream Mapping': Vrielmann and Schwope (2001), Harrop-Allin et al. (1999b,a, 2001), Hakala (1995), Hakala et al. (2002), Bobinger (2000), Salvi et al. (2002)).

Indirect imaging with time-resolved spectra

When time-resolved, high-resolution spectra are available, it is possible to measure velocities by the Doppler-shift of spectral lines and thus get a picture of all motions within the system.
In CVs all parts of the system are moving rapidly – both stars are orbiting each other with several hundred km/s. If there is an accretion disk, the disk is rotating with the Keplerian velocity, and the matter in the ballistic and the magnetically guided accretion stream (if existent) reaches even higher velocities of several thousand km/s. Due to the orbital motion of both stars, the observer sees the system from different directions, which causes the fractions of the velocity vectors parallel to the line-of-sight to vary with respect to orbital phase.
Using the quasi-2D information in phase-resolved spectra – one dimension is wavelength (velocity), the other time (viewing angle) – it is possible to map the intensity onto surfaces in velocity space, e.g. the orbital plane (Doppler-tomography, section 2.1), or onto surfaces in the 6-dimensional phase-space, e.g. the Roche-lobe (radial velocity fitting (Southwell et al., 1995), Roche-tomography, section 2.2)[1], or the accretion stream (Heerlein et al., 1999).

It is not possible to transform the velocity distribution into a spatial distribution without additional assumptions. Thus the shape of the surface (accretion disk, accretion stream, Roche-lobe) or a physical model, coupling velocities to spatial positions, have to be specified. Additionally, one has to assume the emission law for the matter.

In order to map the intensity onto the Roche-lobe, only the shape, determined by the gravitational potential of two orbiting mass-points, and the emission law (intrinsic line-profile, limb-darkening, ...) is necessary.
In the case of the accretion stream one has to assume a behaviour of the matter when interacting with the magnetic field. Either one assumes a fixed geometry calculated beforehand, or includes a number of model-parameters in the fitting process, like done by Heerlein et al. (1999).

The amount of additional assumptions for the model-construction could be

---

[1] Another method to get a line flux map of the Roche-lobe is flux-deficit fitting (Davey and Smith, 1996). This method uses the light-curve of an absorption line, but not the velocity information.

reduced, when high-resolution spectroscopy of a polar with a so far unavailable time-resolution were performed, so that eclipse light-curves for the substructures within spectral lines could be derived. This would lead to information about all 6 coordinates (x,y,z,v_x,v_y,v_z) in the phase space. With both, velocity and position, it should be possible to construct a physically consistent model of the accretion in polars.

Methods using other kinds of data

There exist more indirect imaging methods, making use of the information gathered in other wavelength bands or with different instruments, like polarimeters. I will not describe them here, but information about them can be found in the book Boffin et al. (2001).
A review article on indirect imaging techniques especially applicable in the case of polars, is the article by Schwope (2001) in the abovementioned book. There other methods, using data in the UV and X-ray range to determine the shape and properties of the accretion region on the white dwarf, are also described, as well as the possibility to create a map of the white dwarf's magnetic field structure by analysis of Zeeman-split absorption lines or by analysing the cyclotron emission from the accretion column (Stokes imaging).

The quality of the reproduction in those indirect imaging methods which are assuming a certain geometry, depends – apart from the quality of the data and the appropriate model for the geometry – strongly on the accuracy of the system parameter determination. The fundamental system parameters are orbital period P, inclination i and the masses of the stars, M_1 and M_2. Deviations from the real values may lead to artifacts in the determined structures.

For all indirect imaging methods, the systems have to fulfill one important condition:

A. There are no intrinsic variations within the system on time-scales less than one orbit, i.e. all variations seen in the spectra or in the light curves are caused by changing visibility or by projection effects.

Chapter 2

Doppler- and Roche-tomography in detail

2.1 Doppler-tomography

Doppler-tomography (Marsh and Horne, 1988) uses the information about the velocity of the line-emitting matter from the spectra: If one assumes that no additional effects cause broadening of spectral lines, all line emission/absorption deviating from the assumed intrinsic line profile is originating from matter having a velocity component parallel to the line-of-sight, which causes the lines to be Doppler-shifted.

If the line-of-sight is changing with time – e.g. in a rotating system – the projection of the velocities existing in the system onto the components parallel ($v_{\|}$) and perpendicular ($v_{\perp}$) to the line of sight varies, thus changing the line profile.

With time-resolved spectroscopy of one orbital cycle of a CV one gets projected velocity-distributions for a number of different viewing angles. Similar to tomography in medicine – which creates a three-dimensional image out of several X-ray images taken at different perspectives – Doppler-tomography creates an intensity-distribution in the two-dimensional velocity space.

In this section first the practical realisation of Doppler-tomography is described, later the results and ways of their interpretation are explained. The limitations of method and data used are discussed, as well as the maximum-entropy approach to reduce the effective number of free parameters.

2.1.1 Calculating the intensity map

Doppler-tomograms can be calculated with different methods:

The easiest way is the 'backprojection', which is simply the reversal of the projection of the Doppler-tomogram explained in Fig. 2.1: The intensity from all spectra, added to the distribution in the velocity plane under the appropriate angle, gives the intensity map. The results from this method are strongly depending on the signal-to-noise ratio of the data, because all noise is pro-

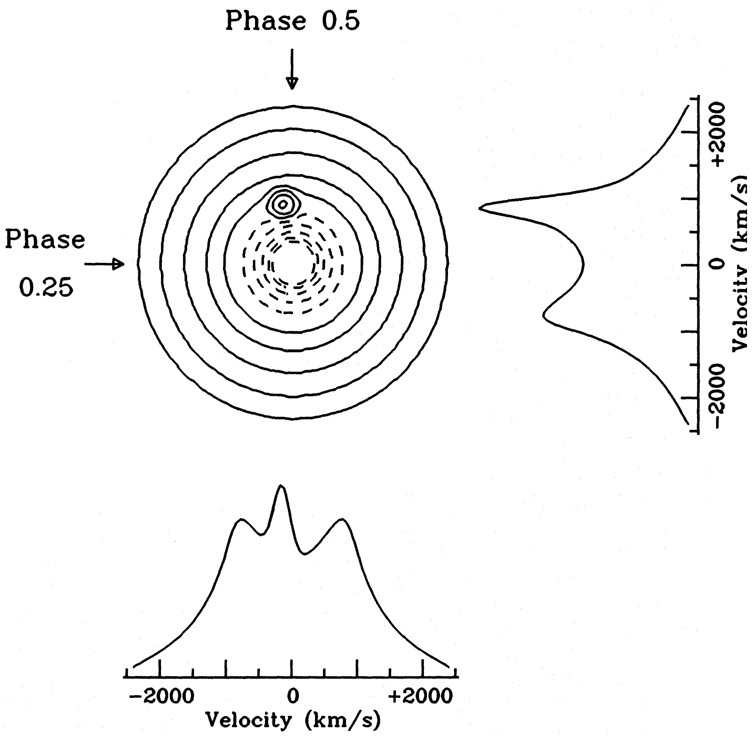

Figure 2.1: Projecting a Doppler-tomogram: If a Doppler-tomogram is projected under the angles corresponding to orbital phase, synthetic line-profiles are the result. (taken from Marsh and Horne, 1988)

jected into the map as well. Thus, in practice the data are additionally filtered (filtered back projection, Robinson et al. 1993).
Other methods, which are not as sensitive to the noise in the data, are using fitting algorithms to calculate the map. The map in velocity space is modified and projected until the projections are fitting the observed spectra at all angles best. In Maximum Entropy methods (see page 37) the entropy of the map is also optimised, which reduces the effective number of free parameters of the fit.
The quality of the reconstruction depends – apart from the signal-to-noise ratio and the spectral resolution of the data – on the phase sampling of the spectra. The effects of undersampling are illustrated in Marsh and Horne (1988), their Figure 7.

2.1.2 Interpretation of the maps

The velocity space, in which the intensity map is calculated, is the projection of the velocities with components in three dimensions onto the orbital plane with coordinates v_x and v_y. v_x is the velocity component in the direction from M_1 to M_2, v_y the one perpendicular to it in the direction of the orbital motion (see Fig. 2.2, lower panel).

For a rigid rotator around the z-axis (perpendicular to the orbital plane, intersecting at the barycenter), $v_{\|}$ depends on the spatial coordinates (x, y), the phase-angle ϕ, which measures the angle between the line-of-sight and the connecting line between both stars ($\phi = 0 \Leftrightarrow$ secondary in front of white dwarf), and the system's inclination i, which scales the velocity with the factor $\sin(i)$.

The Doppler-tomogram of a rigid rotator would show a point for every line emitting spot in the system, with a distance from the point of origin according to the rotational velocity and an angle with respect to the v_x-axis according to the phase angle of maximum $v_{\|}$.

The accreted matter in CVs doesn't follow a rigid rotation. It is falling in the direction of the white dwarf, forms an accretion disk (so matter is rotating with Keplerian velocities), or has a non-vanishing velocity-component v_z (parallel to the rotational axis).

The first two cases only add an offset in velocity and phase to the values for the rigid rotator, depending on the direction of the motion in co-rotating coordinates.

The latter case creates additional structure in the tomogram. This effect is discussed on page 28.

For objects other than a rigid rotator there is no way to transform the velocity maps (Doppler-tomograms) directly into an intensity distribution in position space, because without further assumptions matter with a specified velocity-vector can be located at any point within the system. From calculations with certain physical assumptions one can predict the positions of system components in the tomograms, as is shown in Fig. 2.2.

Shown are the outlines of the Roche-lobe (easy to recognise: solid line for the secondary star, dashed line for the one of M_1), the trajectory of a free-falling particle starting at L_1 (the ballistic stream, open circles on a dotted line), and an accretion disk rotating with Keplerian velocities around M_1 (solid circle marks the outer rim, dashed circles are trajectories closer to M_1). If there were particles at the spatial positions of the ballistic stream rotating with Keplerian velocities, they would have velocity-positions according to the second dotted line with circles on it, starting on the far side of the secondary in velocity coordinates.

By comparing these calculated positions in velocity-space to tomograms calculated from observed spectra, it is possible to get hints on the accretion geometry. But this has to be done carefully, as there are certain assumptions involved.

2.1.3 The axioms of Doppler-tomography

The preconditions for Doppler-tomography – additionally to the main one – are:

B. optically thin lines,

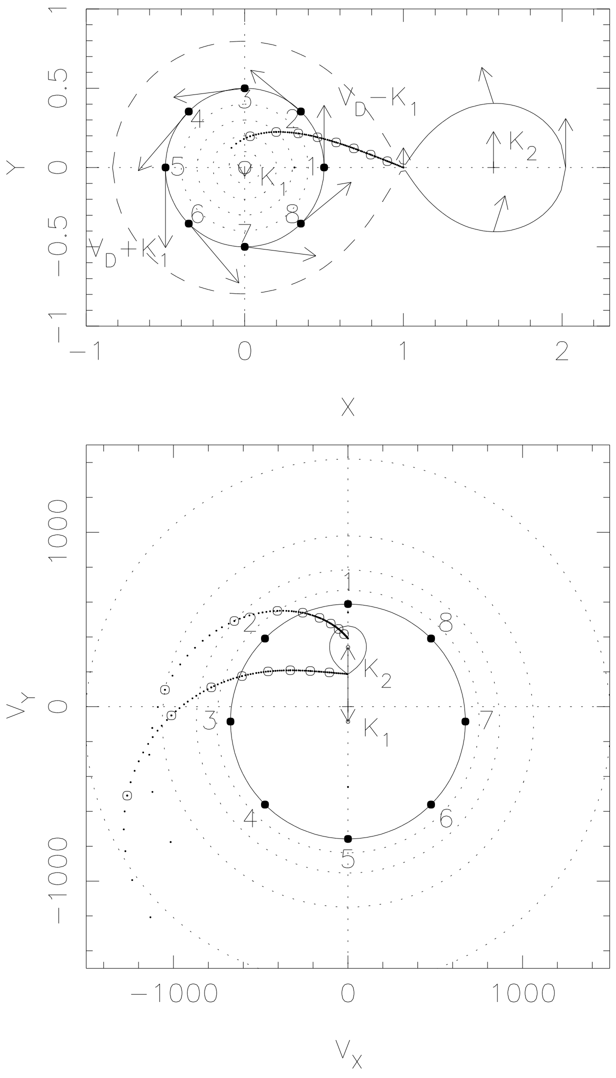

Figure 2.2: Doppler-tomography: Position and velocity coordinates (Figure by Keith Horne): The positions are given in units of the distance $M_1 - L_1$. For calculation of the velocities from the positions one has to assume the projected orbital velocities of both stars ($K_1 \times \sin(i)$ and $K_2 \times \sin(i)$).

C. the intrinsic line-width is negligible compared to the spectral resolution,

D. all motions are parallel to the orbital plane.

These conditions are potentially violated in CVs:

A. Accretion doesn't happen in a smooth, constant way. Small changes on the secondary star near L_1 – e.g star spots, oscillations – may change the density of the accreted matter. The magnetic fields of both stars interact with each other, as well as with the accreted matter, thus leading to changes in the field geometry. Oscillations can happen in the accretion

column on the white dwarf, as well as in an accretion disk or an the secondary star. And, finally, the rotation of the stars is normally not synchronised.
To get information on the stability of the system's emission, observational data should cover more than one orbit. Then one can discern between singular and repeating events.

B. The secondary star as well as the white dwarf are obviously optically thick. But also the accretion stream can be optically thick, either in single spectral lines or in the continuum, and all this may vary with position and time. Thus projection effects and obscuration have to be taken into account.
These effects don't change the measured velocities much, but have influence on the mapped intensity distribution.

C. The intrinsic line profile should not be broadened in most places in the system (accretion stream, secondary), because there temperature and pressure are not very high. Only on the surface of the white dwarf and in the accretion column, directly above the white dwarf's surface, temperature and pressure can reach values which are not negligible. Since the white dwarf only has a small surface area, and the accretion column is even much smaller, they don't contribute much to the over-all flux of optical emission lines.
The emission lines of the Balmer-series of the hydrogen atom are often saturated. Thus they appear broader in the spectra, and Doppler-tomograms of these lines don't show as much details as weaker lines. Stellar atmosphere model calculations with hydrogen in Non-LTE show a complicated line-profile (Barman et al., 2004), which could lead to a broader line profile for certain spectral resolutions.
Problems could arise during the interpretation, when extended emission regions are considered to be Doppler-broadened.
In most cases this assumption is fulfilled sufficiently.

D. The orbits of the two stars and the ballistic part of the accretion stream are – by definition – parallel to the orbital plane. The magnetic axis of the white dwarf will normally be inclined with respect to the orbital plane, thus causing a velocity component perpendicular to it when matter follows the field-lines. This results in additional structure in the tomograms (Fig. 2.3).

Emission from matter moving parallel to the orbital plane has the same amount of Doppler-shift when seen with a phase difference of $1/2$, just the sign has changed. The Doppler-shift simply follows a sinusoid over orbital phase. In the case of an additional velocity component perpendicular to it, v_z, the situation is more complicated.

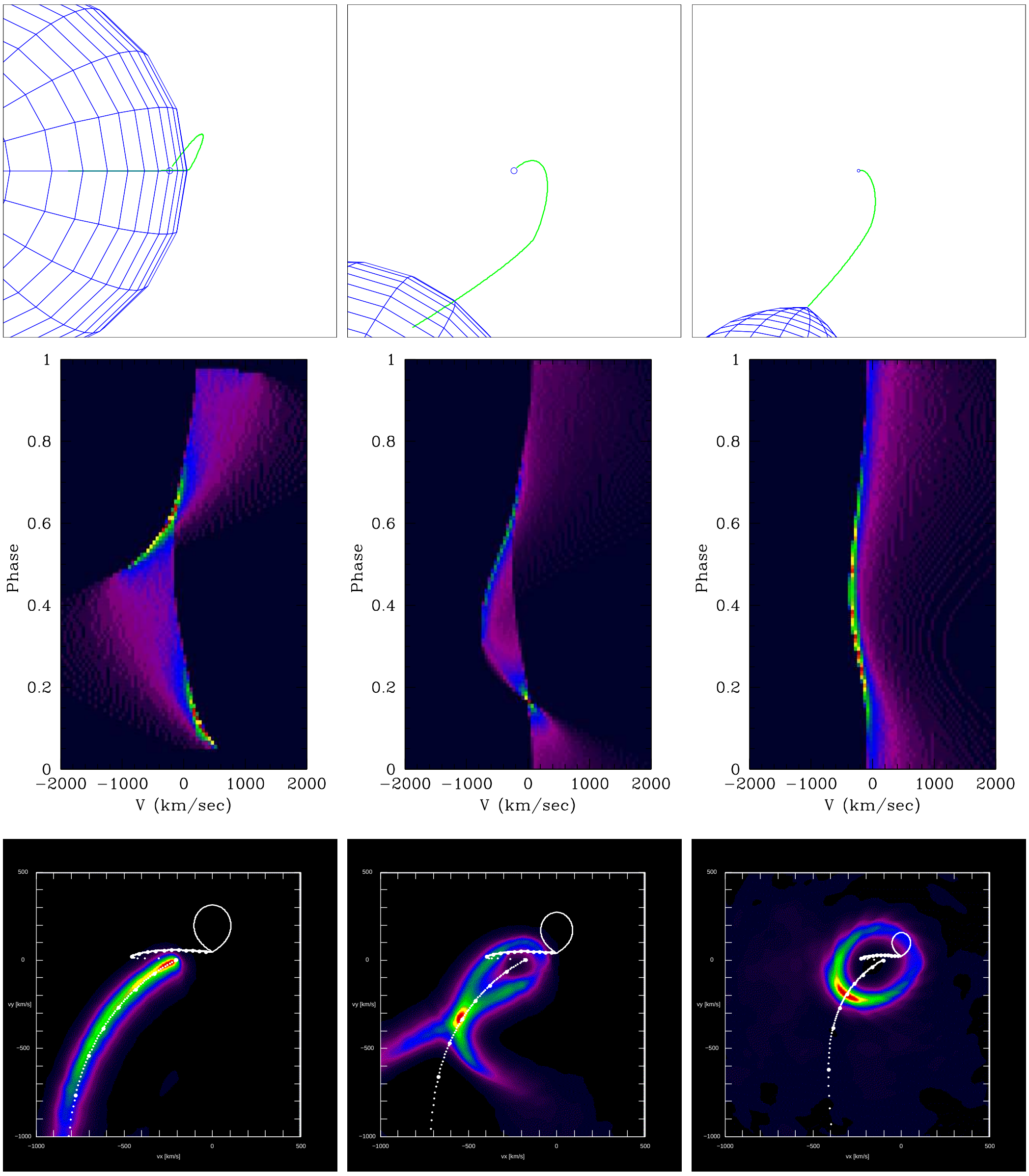

Figure 2.3: Effects of non-vanishing v_z on Doppler-tomograms: The same system shown under different inclination angles (left to right: 90, 60, and 30 degrees), the resulting trailed spectra, and the resulting Doppler tomograms from synthetic line profiles, created for the magnetically guided part of the stream. (colours: Fig. A.1)

In Fig. 2.3, one system is shown under different inclination angles (top panels). The accretion stream consists of a ballistic and a magnetically guided part. The Doppler-tomograms shown below are calculated from synthetic spectra. These were calculated for the magnetic part of the stream only, assuming optically thin emission. The same inclination angles like shown in the views above were used. For 90° inclination v_z has no influence on the tomogram at all. If there were no superposition

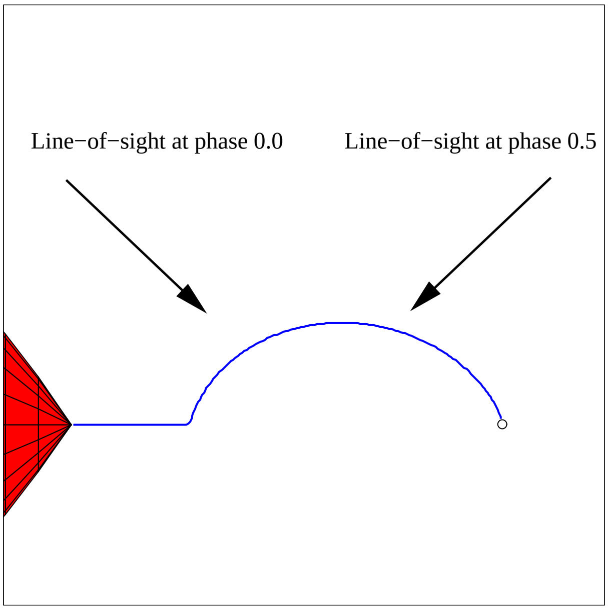

Figure 2.4: Doppler-tomography – Origin of v_z-effects. (View from the orbital plane.) For a given inclination, parts of the magnetically guided stream get a Doppler-shift whose amount is not varying sinusoidally. Thus the absolute value of Doppler shift half an orbit later is not the same.

> with v_x and v_y (as it is at 0° inclination), this would lead to a perfect ring, centered around the coordinate origin (see the right panel, where the result is shown for a low inclination). For an inclination less than 90° but higher than 0°, the velocity component v_z superposes v_x and v_y, but with varying effects at different phases. In Fig. 2.4, at phase 0.0 the fast-moving stream near the white dwarf gets the maximum Doppler-shift, while the matter near the coupling region moves perpendicular to the line-of-sight, thus getting none at all. Half an orbit later, at phase 0.5, the emission from the slower matter near the coupling-region is maximum Doppler-shifted, while the matter near the white dwarf has no projected velocity. Thus emission from matter at one point in spatial coordinates moving with a certain velocity $(v_x, v_y, v_z \neq 0)$ doesn't transform to a point in the Doppler-map, because the absolute value of its projected velocity will not be the same at opposite orbital phases.
> This effect is of low importance for high-inclination systems ($i > 75°$, e.g. the eclipsing ones). For systems with lower inclination the tomograms have to be interpreted cauteously.

Even if some of the conditions are not fulfilled completely, the Doppler-tomograms are valuable for the analysis of CVs. One only has to be careful when interpreting the results and has to check their consistency with the spectral data.

2.1.4 Doppler-tomography with MEM

Maximum Entropy Methods (MEM) assume that from two fits reaching the same χ^2, the one with the higher entropy – i.e. which is smoother – is to be preferred. This approach is motivated by the observation that the physical systems in nature 'prefer' the energetically advantageous states, i.e. the states with the highest entropy.

With MEM it is possible to get unique results in the case of under-determined problems. Therefor, the effective number of free parameters of the fit is reduced by coupling the values to a certain extent. How this is done and if this approach is reasonable at all for a certain problem, needs some consideration.

The Doppler-tomograms shown in this work were produced with the publicly available Maximum Entropy code by Spruit (1998). The results of this code are much less affected by noise in the data or a few missing spectra than those calculated with (filtered) backprojection.

As in all MEM codes, an additional parameter controlling the weight of the entropy in the quality of the fit is introduced. It cannot be determined by the fitting procedure, but has to be set manually for each data set. The user has to check that there is enough structure present in the tomogram to match the data, but not more than is resolved within the spectra.

2.2 Roche-tomography

This section describes the idea of Roche-tomography, its limitations and possible problems, and my implementation 'AStRoTom'. Test results obtained from synthetic spectra and results from tests of the ability to determine the system parameters are discussed.

2.2.1 The idea

The atmosphere of the secondary star, as seen in trailed spectrograms, doesn't show a homogeneous distribution of absorbtion and emission lines on its surface. Instead it shows the undisturbed properties (absorption features) of a late-type star on the hemisphere not facing the white dwarf, and emission lines in addition to less prominent absorption lines on the one facing it. The reason is the irradiation with high-energy photons from the white dwarf and the accretion region, and, maybe, the changed atmosphere structure due to the deviation from a spherical symmetry. Both, the absorption and emission lines, are in some systems not distributed evenly on the hemispheres: An asymmetry in both with respect to the connecting line of both stars may be seen with Doppler-tomography already, and may also be visible in the trailed spectral lines. This asymmetry is usually explained by shielding of the incident radiation by the accretion stream/curtain. Other deviations from a flat distribution of emission are expected from star-spots due to magnetic activity.

Time-resolved spectra contain more information about the origin of spectral lines than is revealed with Doppler-tomography, where only the velocity information is used. The information about the visibility and projected area at each phase angle can only be used marginally, because the matter is assumed to be optically thin.

In the optically thick regime it is possible to make use of those effects which are violating the assumptions of Doppler-tomography, the changing visibility and projected sizes (resulting in a changed flux) of the emitting parts of a rotating object, to calculate an intensity map of its surface.

Two surfaces in a CV can be specified in advance with a minimum number of assumptions: the white dwarf and the secondary star. Since the determination of the shape of the accretion stream in polars is one of the aims of the analysis of the data, the shape of the stream surface cannot be specified *a priori*.

Roche-tomography is a method to derive the intensity distribution of spectral lines on the surface of the secondary star in CVs by analysing the time-resolved profiles of spectral lines. With additional assumptions it is possible to get information on the fundamental parameters of the system, like inclination i, and the masses M_1 and M_2.
It was first described by Rutten and Dhillon 1994, later Watson and Dhillon 2001 (from now on referred to as WD2001), Watson et al. 2003 (from now on referred to as WAT2003), Potter et al. 2004.

To the code they use I have no access, so I wrote a program myself. In the following I describe its principle and my implementation.

2.2.2 The situation

In the case of 'normal' CVs with a high mass-transfer rate the secondary star is thought to be Roche-lobe filling, thus maintaining the mass transfer by Roche-lobe overflow at the L_1 point. This is implying that the secondary's rotation is locked to the orbital motion and that it is moving on a circular orbit. If this assumption is correct, the Roche-lobe can be used as the secondary's surface. The gravitational potential of two orbiting point-sources, M_1 and M_2, for a given orbital period P, as given by Eq. (1.1), can be written as

$$\Phi = -\frac{GM_1}{a}\left(\frac{1}{\sqrt{x^2+y^2+z^2}} + \frac{q}{\sqrt{(x-1)^2+y^2+z^2}} + \frac{q+1}{2}[(x-\mu)^2+y^2]\right) \tag{2.1}$$

with $\mu = q/(q+1)$ and $q = M_2/M_1$.

Thus the shape of the potential is dependent only on the mass ratio, whereas the other system parameters are just entering the scaling factor $(GM_1)/a$. The Roche-lobe is given by the equipotential surface containing the L_1, the minimum of the potential between the two stars.

For Roche-tomography, additional assumptions on the system, apart from the main one for indirect imaging, have to be made:

B. all line emission or absorption is arising on the Roche-lobe surface which is assumed to be optically thick,

C. the intrinsic line profile is the same all over the Roche-lobe.

Again, these assumptions can be violated in the systems:

A. M-stars in cataclysmic variables may have strong magnetic fields and can thus show fluctuations of the magnetic field strength on the stellar surface. This would result in star spots. The properties of them could be changing within an orbital cycle. Star spots could also lead to changes in the mass transfer rate, which would result in changes in the incident radiation. These would directly result in modified distributions of the absorption and emission lines on the secondary's surface.
With observational data from more than one orbit it is possible to discern between singular and repeating events, and thus avoid false interpretations.

B. Line emission will also arise in the matter being accreted. At certain orbital phases the projected velocities of the secondary star and the accretion stream will overlap, and the emission from the latter will contaminate the contribution of the secondary star. Emission from an accretion disk will always superpose the one from the secondary. Additional absorption may be caused by the accretion stream or disk, and also by circumbinary matter or matter expelled from the system.

In the observed spectra these complications would be clearly visible and could be taken into account.

C. The intrinsic line profile will vary over the stellar surface, because M-stars have deep convection zones which will influence the photosphere and thus change the local line profile due to additional velocity components. The secondary star is also highly asymmetric. This will result in differences in the effectiveness of energy transport, e.g. to the L_1 and the opposite point. The temperature structure will be different, and this will result in different line profiles.

Due to differences in the surface gravity (the Roche-lobe is an equipotential surface, but the gradient is different at different points), the limb darkening varies also over the surface.

Furthermore, the limb darkening for spectral lines is different from the one for the continuum (see next section). Thus the intrinsic line profile will be changing with the projection angle.

Irradiation changes the temperature structure of the stellar atmosphere, which leads to a differing line-profile also.

With the currently available spectral resolution of time-resolved spectra, most of the effects should not be detectable.

Results from Roche-tomography have, thus, to be interpreted with caution. But especially the deviations from the assumption of the same intrinsic line profile are rather negligible for the data available today. The low signal-to-noise ratio of the trailed spectra will prevent detection of artifacts created by them.

Despite of all these limitations, the information one can get from Roche-tomography is valuable. Together with information about the accretion stream and the white dwarf it will complete the knowledge about the accretion process in CVs. It also can be used to limit the possible system parameters and to get information on the atmosphere structure of the secondary stars.

2.2.3 My code: AStRoTom

Parametrisation of the Roche-Lobe

In my Roche-tomography program – AStRoTom – I divided the Roche-lobe in a number of surface elements of nearly the same size (Fig. 2.5).

The grid points are calculated by an iterative procedure. First the L_1 point and its gravitational potential is determined. The x-axis between the L_1 and the opposite surface point with respect to the mass centre of M_2 is then divided

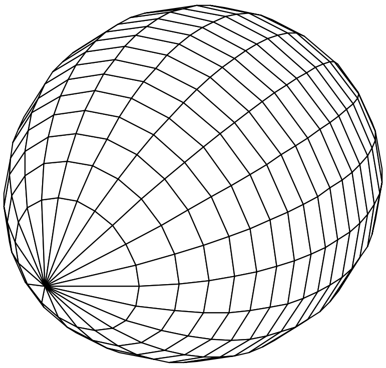

Figure 2.5: The Roche-lobe, divided in 20×20 nearly equally-sized surface-elements

in equally sized segments. For all points marking the end of such segments, the radial distances for a number of equal steps in rational angle around the x-axis are determined, which lead to the same potential as the L_1. Thus the corners of the tiles are defined. The actual size of the tiles is then calculated, in the case of the quadrangles by determining the sizes of the sub-triangles. The iterative procedure now modifies the x-values until the sizes of the tiles are nearly equal[1] (The computation of the sizes neglects the flattening of the Roche-lobe parallel to the rotational axis).
Afterwards, the 'centres of mass' of the triangles and quadrangles are calculated. These are the points to which all emission of the tiles is assigned, and whose projected rotational velocities are used for the Doppler-shift of the intrinsic line-profile. Although it is impossible to form a flat quadrangle out of four points on an arbitrarily bent surface, and the 'centre of mass' of all the elements is not exactly lying on the Roche-lobe but somewhat closer to the mass centre of M_2, the deviations in position and velocity are below one per cent for a sufficiently high number of tiles (e.g 20×20).

Creating the spectra

The spectrum at a certain phase-angle ϕ is in principle calculated according to Eqn. (2.2) and afterwards folded with a Gaussian representing the instrumental resolution.

$$\begin{aligned} I(\lambda, \phi) \quad = \quad & \sum_{i}^{N_{Roche}} I_i(\lambda, v_i) \\ & \times size_i \times \cos(\theta_i) \\ & \times m_i \end{aligned} \tag{2.2}$$

---

[1] This is advantageous for the quality determination of the fit (see later).

N_{Roche} is the number of visible surface elements of the Roche-lobe at a given phase ϕ, $I_i(\lambda, v_i)$ is the Doppler-shifted intrinsic line-profile, $size_i$ is the area of each surface element, θ_i is the angle between the surface-element's normal vector and the line-of-sight, and m_i is the intensity value for the map element. The intrinsic line-profile is the same for all elements, so all deviations from it in the observed spectrum are ascribed to Doppler-shift. In my code it is possible to use either an user-specified line-profile from a file or a Gaussian, for which the FWHM has to be specified. The intrinsic line profile is additionally folded with a Gaussian. This accounts for the not infinitely small surface elements, whose calculated brightness is assigned to their centre only, and for the line-broadening caused by the orbital motion within one phase-bin. The FWHM has to be specified by the user.

In detail the projection is much more complicated than it seems in Eqn. (2.2): The observed spectrum has a pre-defined binning, and into these bins the shifted intrinsic profile has to be distributed. Since the profile has also a limited resolution, one has to account for partly overlapping bins. To reduce the errors of using a step-function instead of a smooth one, the intrinsic profile has a three times higher resolution than the spectrum it is projected into. Thus the deviations for a single element are of the order of a few percent. On the global scale these small effects tend to average out.

Limb-darkening is not included in my code, contrary to the code used by WD2001. The reason is that there is little reliable data on limb-darkening for low gravity, and that the limb darkening of spectral lines has a different behaviour than that of the continuum. A paper by Orosz and Hauschildt (2000) showed that limb-darkening in the case of giants (and thus at low gravity) – calculated with a stellar atmosphere code in spherical symmetry – vastly deviates from all the established power-laws used so far (linear or two-parameter law). This is confirmed by the work of Hadrava and Kubát (2003). They additionally studied the limb-darkening of absorption lines and found that it is different from the continuum one. They state that a line which is in absorption at the disk centre, develops emission wings at the edge of the stellar disk and turns into an emission line just above the edge of the photosphere.

Both, the shape of the continuum limb darkening in the case of low gravity and the inversion of lines, cannot be put into a simple formula for limb darkening but can only be treated by radiative transport.

In the case of the secondary stars in CVs, the gravity at the surface is much lower than in single stars of the same mass – at least in the regions near L_1. Thus the limb darkening (for the continuum) depends on the location on the secondary's surface. For irradiated stars the situation is even more complicated: The incident radiation is changing the temperature profile of the stellar atmosphere. This modifies the effective temperature of the photosphere and also the profiles of absorption and emission lines (Barman et al., 2004).

I think that by including an unappropriate limb-darkening formula the trustworthiness of the reproduction is reduced, especially as long as the signal-to-noise ratio of the available data is not much enhanced, and does thus not allow

artifacts like shown in WD2001 to be resolved.
A possible solution to the problem of limb darkening could be the usage of a grid of line profiles, calculated with a radiative transfer code for the range of possible values of surface gravity and viewing angle. For the values in between one could interpolate the spectra.

Determining the quality of the fit

The main quantity measuring the quality of a fit is the correspondence of the calculated spectra with the observed ones. This quantity is measured by the χ^2, as usual.
Without additional restrictions, the degrees of freedom of the fit are the number of map elements. The spectral line profile in measured data is extended over a few dozen pixels only, while the maps I use have e.g. 400 tiles. Thus the problem is highly under-determined and many different maps could fit the data equally well. Additional restrictions are therefore necessary to reduce the number of free parameters.
For this purpose, assumptions on the resulting intensity maps are introduced. The standard approach is justified by the observation that in nature the physical systems tend to settle in those states which are energetically advantageous. These are the ones with the highest entropy, thus algorithms using the entropy of the map to reduce the number of free parameters are called **Maximum Entropy Methods**.
The quality of the fit is calculated according to Eqn. (2.3), i.e. it is the sum of the χ^2 and an entropy S. The entropy is multiplied with a parameter α, which controls the importance of the smoothness for the quality determination and has to be specified by the user.

$$Quality = \frac{1}{N_\lambda} \sum_{i=1}^{N_\lambda} \frac{(I_{i,comp} - I_{i,obs})^2}{\sigma_i^2} - \alpha \times S \tag{2.3}$$

(N_λ is the number of wavelength bins in the 2D-spectrum, σ_i is the error of the observed intensity, *comp* and *obs* are indezes marking the computed and observed values, respectively)
A quality defined like this (with $S < 0$) is a number always larger than zero and has to be minimised.

The appropriate definition of the entropy, resp. smoothness of the map, is highly important for the result and the convergence behaviour.
I tested several entropy definitions: Just summing up the absolute values of the differences of neighbouring map elements lead to a smooth map, but the convergence of the fit was very slow. The convergence speed was increased dramatically by using a logarithmic definition of the entropy.
As introduced by Horne (1985), I am using an entropy calculated with respect to a so-called default map. This default map defines the correlation-pattern considered as smooth: This means that for e.g. a homogeneous default map, as

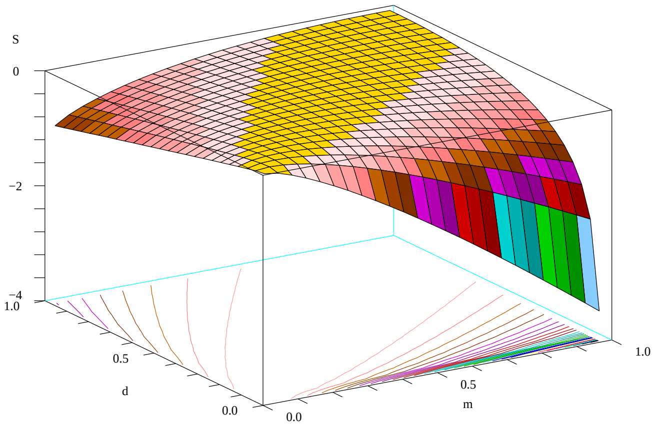

Figure 2.6: Plot of the entropy (S, Eq. 2.4) with respect to the values of map (m) and default (d).

stated by Horne (1985), the entropy measures the deviation from homogeneity. Such a map is useful to detect small-scale structure in a mainly homogenous distribution, because it leads to the 'most uniform' image and neglects the small-scale deviations. The entropy with respect to a smoothed version of the data map is especially sensitive to structure smaller than the smoothing range, while large-scale structure will affect the entropy value less. It thus leads to the smoothest map which is consistent with the data.
Depending on the problem to fit with MEM, the optimum default map can have other shapes, e.g. for accretion-disc eclipse-mapping (Horne, 1985) an axisymmetric map proved to be useful.
If using the definition by Horne (1985), $S = -\sum_{j=1}^{N_{Roche}} m_j \log_e \frac{m_j}{d_j}$ (m_j are the flux values of the actual data-map, d_j those of the default map), the entropy could reach positive values. The definition I finally used is the one specified by Eqn. (2.4).

$$S = \sum_{j=1}^{N_{Roche}} m_j - d_j - m_j \log_e \frac{m_j}{d_j} \tag{2.4}$$

It is the same definition as used by WAT2003. As seen in Fig. 2.6, the function approaches zero only if $m = d$, and is strictly negative. It also is obvious that the map has to be strictly positive to use this entropy definition (because of the logarithm).
Contrary to the homogeneous default map, with the average of the data-map assigned to each pixel, used by WAT2003, I decided to apply a smoothed version of the actual map as the default. This does not favour any user-defined shape of intensity distribution and is thus a quite loose restriction.

Especially in the case of the large differences in line flux from the irradiated and unirradiated hemisphere of secondary stars in polars, a homogeneous default seems inappropriate. I use the smallest possible smoothing radius, taking into account only the direct neighbours. In 2.2.4 I show, however, that the homogeneous default map is better suited to detect small-scale substructure like star spots.

When using the quality-function as defined in Eqn. (2.3) with the entropy from Eqn. (2.4), it is advantageous to have similarly sized surface elements. The reason is, that small elements would be of no importance for the χ^2 determination (and could thus be assigned arbitrary values), but would have a big impact on the entropy calculation. With nearly the same size, the weights of the elements are balanced better.

Fitting the intensity map with Evolution Strategy

For fitting the data, the projected spectra are calculated from the intensity map and compared to the observed ones at the corresponding orbital phase. The fitting procedure modifies the intensity map until the optimum quality value is reached.

The optimisation problem has as many free parameters as there are surface elements of the Roche-lobe. Of course, a larger number would lead to a better fit, because small features could be fitted more accurately. But the computational effort to reach convergence of the fit is increasing faster than linearly with the number of free parameters.

Sampling the Roche-surface with 400 surface elements, as I did, is a good compromise between a well-resolved map and an acceptable duration of the calculation. The velocity resolution of this parametrisation of the Roche-lobe is – for typical parameter values found in CVs – of the order of 10 km/s – higher than the resolution of data available to me.

However, the computer time necessary to achieve a fit depends strongly on the computational method used. The most time-consuming part within one iteration is the projection of the map to get the spectrum and the calculation of its quality. The aim is to get a high value for the progress per calculation time.

I chose Evolution Strategy (ES) as optimisation technique, which was first described by Rechenberg (1973). This method uses an adaptation scheme similar to the evolution of live, making use of modification and selection to find the attributes resulting in the best adaptation to the environment.

For this purpose a 'population' is created, consisting of a number of 'individuals'. In the case of Roche-tomography these individuals consist of a brightness map as main attributes, and values for certain evolution parameters, which influence the inheritance of the individuals' attributes. Like in real life, the individuals of a population are not equally well fitting into their

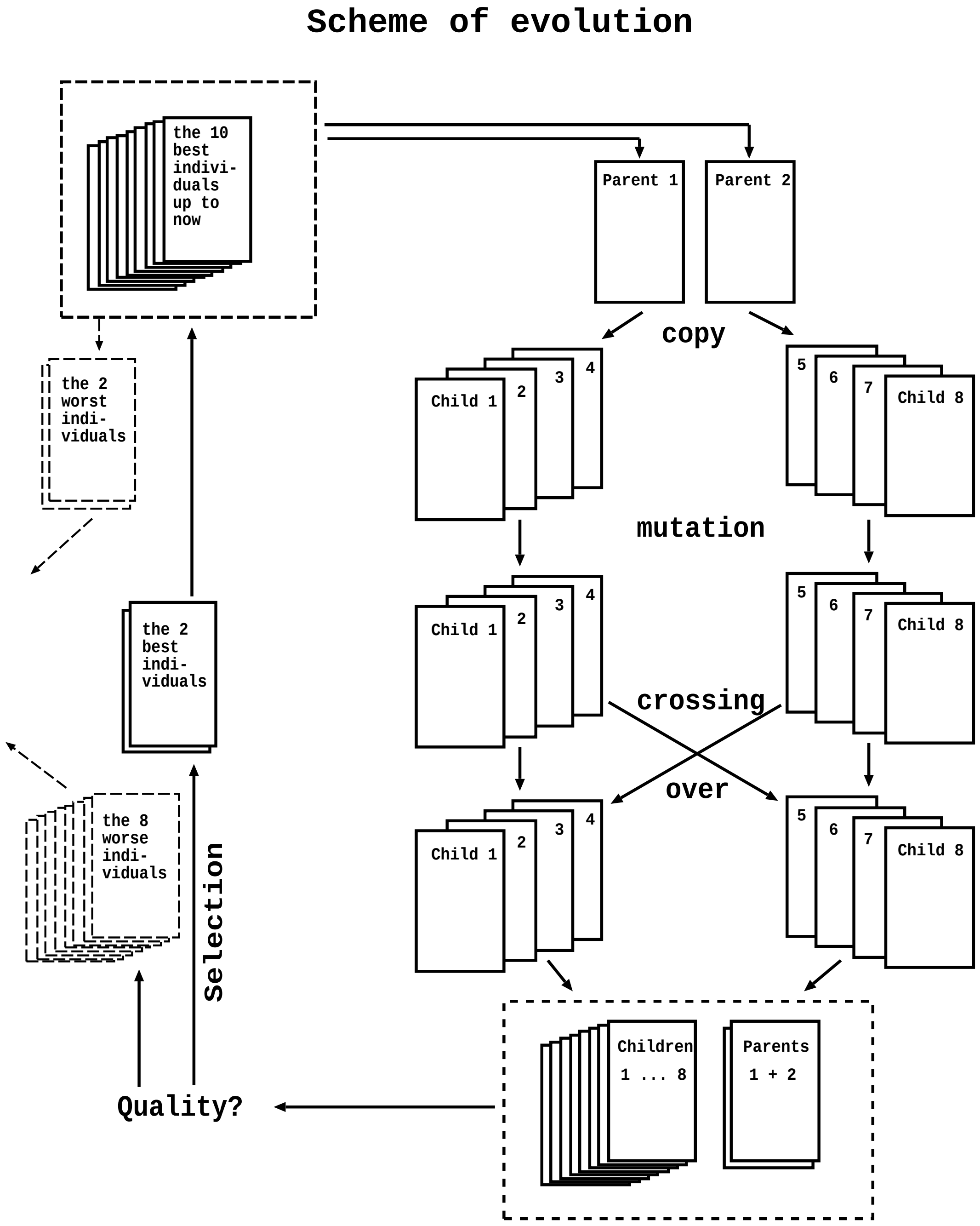

Figure 2.7: The scheme of Evolution Strategy as used in AStRoTom

environment. In the case of Roche-tomography, the degree of fitness is given by the quality function.
The best-fitting individuals have a higher probability to inherit their attributes to the next generation, the least suited ones will 'die out'. But at each inheriting-process errors are made. These are not just unavoidable but necessary, because in a number of cases the changes will lead to a better suitability. The former mechanism is a schematic description of the asexual reproduction.

In nature one sees another mechanism of reproduction: the sexual reproduction. Here the evolution 'uses' the advantage of being able to combine the results of two separated optimisation runs. Thus it also is possible to correct changes leading in the wrong direction.

The scheme of the sexual reproduction used in my code of Evolution Strategy is shown in Fig. 2.7. In this evolution scheme from the few best individuals so far (10 in the example) two are selected randomly to become the 'parents' of the next generation. Their properties are copied, modified, and evaluated. If one or two of the 'children' has a better quality than any of the individuals from the parents-pool, the latter one is replaced by the new individual.
In the nomenclature of Evolution Strategy this example is a (10/2+8)-ES, meaning that out of 10 possible 'parents' 2 are selected, from which 8 'children' are created, and that the parents already used for reproduction have the possibility to remain in the evolution process.[2]

The 'individuals' consist of an intensity map. Figure 2.8 illustrates the principles of modifications of the maps.

The existing map (3x3 tiles in this example) is first modified by mutation. This means that with a given probability (here: 1/3) a certain value (here: 5) is added/subtracted.
Crossing over (or recombination) exchanges values of the same tiles between two maps with a given probability (here: 1/3).

By applying random variations, the probability to get stuck within a local minimum is lower than in fully deterministic optimisation techniques, where the step-size of the variation is being adapted to the progress in the local minimum. From an initial value the ES is searching in multiple directions (and will thus find multiple local minima). The step-size for the variations is taken from a probability distribution according to a Gaussian around the most favoured value. This allows arbitrarily large steps to occur with a small probability. Thus the optimisation within the local minimum will happen in the case of most variations, but with a certain probability larger steps are done to explore the more distant surrounding.
However, in contrast to Monte-Carlo methods the modifications are not completely arbitrary and the results of earlier generations are the basis for further improvements.
For the highest efficiency of Evolution Strategy, the probabilities and stepsizes have to be adapted to the progress of the optimisation run. To prefer values which have already proven to be succesful, the current values should be preferred to values vastly deviating. But the latter ones should not be completely ruled out to avoid getting stuck in a local minimum. How this is done in

---

[2] An alternative approach to this (μ/ρ+λ)-ES would be a (μ/ρ,λ)-ES, selecting ρ 'parents' out of a pool of μ individuals, where the parents are replaced by the best λ children in any case, even if they have a higher quality value. This approach is used for highly complicated quality-landscapes, but during tests it showed to be less efficient in the case of Roche-tomography.

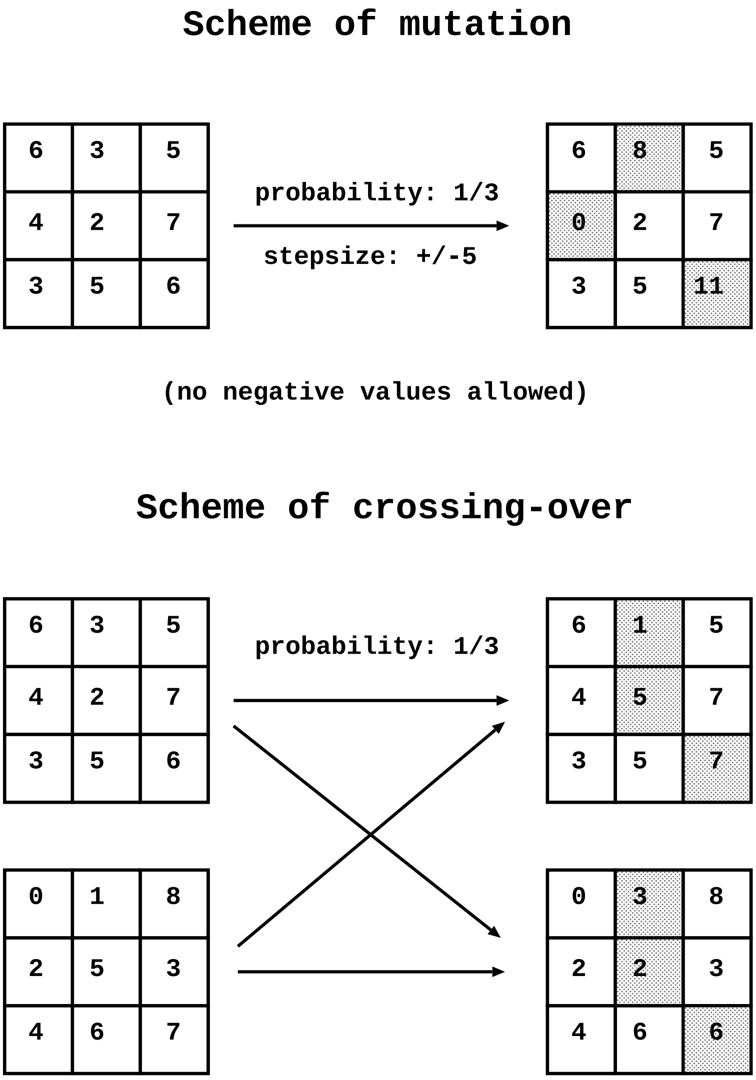

Figure 2.8: The scheme of the modifications in my ES

AStRoTom is described in the following.

The individuals in AStRoTom In AStRoTom the individuals consist of an intensity map and a number of evolution parameters. The intensity maps have floating point values larger or equal to zero. (The actual values are determined by the flux in the spectral line and the number of map tiles.) A virtual map element, which has a constant projected size, is emitting uniformly on all wavelengths and is allowed to have negative values, is added to account for a not perfectly determined continuum level.
Additionally, a number of evolution parameters are also included in the individuals. These are variable parameters and subject to inheritance and modification as well, enabling self-adaptation to the local shape of the quality landscape and to the progress already made.

The first evolution parameter is the stepsize for mutations, which is the same for all map elements. During the inheritance this value is modified to another slightly differing value. This value is determined by a probability distribution centered around the actual value, whose FWHM is 2/5 of the distance to zero. Further evolution parameters also contained in the individuals are the probabilities of mutation and crossing-over. These are modified the same way as the mutation stepsize.

The evolution in AStRoTom The actual fitting is done the following way: For an empty initial map the quality of the fit is determined. The evolution parameters are set to initial values: the mutation stepsize to a small value[3], the probabilities of mutation and crossing-over to 50%. The parental population is created, in the beginning consisting of 16 equal individuals.
The evolution in AStRoTom then takes 2 individuals out of the 'parent' pool and copies each to $\lambda/2$ 'children'. The mutations of the evolution parameters are performed first, afterwards the mutation of the map is performed. This means adding a random value, which is chosen according to a Gaussian distribution centred around zero with FWHM equal to the evolution parameter 'mutation stepsize'. The map of each offspring of one parent is then recombined with the one from an offspring of the other parent. The number of exchanged values is determined by the evolution parameter 'recombination probability'. The evolution parameters are set to a weighted average of the values of both children, according to the amount of exchanged information.
After the quality of each child is determined, the two best children have the possibility to enter the parent pool. If one is better than a member of the pool it is replacing the worst one. Thus one iteration is performed and the evolution continues with the choice of two parents for the next generation.

The iterative process is trying to minimise the quality (taking into account both, χ^2 and entropy), with the secondary aim to reach a predefined value for χ^2: χ^2_{aim}. To get the fitting process running for a homogeneous initial map, the factor α has to be small, so that the gain achieved by getting a better χ^2 is not counter-acted by the loss in entropy. With such a small value the best-fit map would not be smooth. Thus it is necessary to weigh the entropy higher when χ^2_{aim} is approached. The change of the weight cannot happen suddenly, because then the principle of causality would be violated[4], and the evolution parameters would be still adapted to the old weight and not suited for the new one. So the evolution would not be able to leave the local quality minimum. Also, the χ^2 shall not be able to reach lower values than χ^2_{aim}.
Thus I applied an additional weighing function to α, which lets it grow to

---

[3] $\frac{\sum I(\lambda,\phi)}{10 N_{spec} N_{map}}$, with $I(\lambda,\phi)$ the summed flux in the continuum-subtracted trailed spectrum, N_{spec} the number of pixels of the trailed spectrum, and N_{map} the number of map tiles. This proved to be a working value for all input spectra yet.

[4] Evolution strategy needs a form of causality, in which small changes in the data lead to small changes in the quality. Otherwise the adaptation of the evolution parameters to the entropy landscape and the progress is not possible.

infinity for χ^2 approaching χ^2_{aim}:

$$\alpha(\chi^2) = \alpha_0 \frac{\chi^2_{aim}}{\chi^2 - \chi^2_{aim}} + 1.0 \tag{2.5}$$

This approach actually prevents reaching the χ^2_{aim}, but is effectively leading to a good fit in χ^2 with a high entropy. In the case that α_0 is small enough, χ^2 will be close to χ^2_{aim} at the end if it is possible at all to get a fit of this quality for the assumed system parameters.
The actual value of χ^2_{aim} is determined with a fitting run with α set to zero, i.e. with a pure χ^2 fit. χ^2_{aim} is set to a value slightly higher than the minimum χ^2.

The iteration continues until convergence is reached (no significant changes within the last 20000 generations) or the maximum number of iterations is exceeded.
In AStRoTom I use a (16/2+16)-ES, meaning that from a pool of $\mu = 16$ individuals $\rho = 2$ are selected to become the parents of the next generation. The best 2 of the $\lambda = 16$ children created have the possibility to replace individuals in the pool with a worse quality value.
These basic parameters were optimised during numerous test runs to achieve the lowest computation time.
It showed that the progress per iteration was increasing with the number of children (λ) involved. But for λ-values larger than 16 the progress was proportional to λ. The progress per iteration was thus growing as fast as the computer time needed for modification and selection. λ was chosen as the smallest value in this linear regime to use the minimum amount of memory.
The quality reached at the end of the evolution is improving with the number of individuals in the parent-pool (μ). But the convergence speed is rapidly decreasing, because advantageous achievements of single individuals are inherited on a low rate only and thus spreading slowly. The value of 16 individuals in the pool proved to be a good choice for both, convergence speed and stability.
The values for the FWHM of the probability distribution for the evolution parameters were tested as well. Too large values lead to unstable convergence behaviour, because after an incidental improvement with a very large change in stepsize the evolution could not re-adjust to the best value. For values too small the adaptation to the quality landscape and the progress was too slow. A FWHM of 2/5 of the distance of the actual value to zero is a good choice.
It proved to be optimal to perform mutation and crossing-over on all children successively, not just one of the modifications on each 'child'.

Comparison of ES with other optimisation techniques

Optimisation of a function with a large number of free parameters is always problematic. First one has to be confident of beeing able to find the global minimum, although you can never be sure of really finding it. Secondly, the convergence speed is rapidly decreasing with a growing number of free parameters.

The most time-consuming part of the code in the case of Roche-tomography is the projection of the map and the calculation of the quality. So one has to find an optimum ratio of progress to projection and quality determination.

Evolution Strategy creates a pre-specified number (λ) of 'children' per iteration, which have to be compared to the existing 'individuals'. This means that the quality has to be calculated λ times per iterative step. The success rate per quality calculation of mutation in evolution strategy is of the order of 1/2, depending on the shape of the 'minimum valley' and of the actual stepsize. Imagine a valley in two dimensions: At every point of the slope, one half of all directions lead downhill, the other half uphill – if the step size is appropriate. Although the success rate per quality calculation is high, the progress in quality is rather small, since for multiple dimensions the most probable distribution of changes is the equity of improvements and aggravations. To estimate the effects of crossing-over on the probabilities is more difficult. However, experiments with ES show that it speeds up convergence dramatically, because successful features from different individuals can be combined in one.

Compared to gradient strategy, ES is much more effective for large numbers of free parameters (Tab. 2.1).

	gradient strategy	evolution strategy
progress per iteration	large	small
probability of progress	1	1/2
number of quality determinations per iteration	number of free parameters	number of children

Table 2.1: Comparison of ES with the gradient method

The larger progress per iterative step in the case of gradient strategy is not compensating for the much bigger effort calculating the quality for changes in every dimension. Gradient strategy also needs the correct step-size of the variations, which is not easily determined.

The values of progress in the ES also depends on the appropriate mutation stepsize. This assumes an effective self-adaptation to the quality-landscape. The value of 1/2 for the progress probability is an estimate for the best stepsize possible. For deviations from this ideal value the probability is reduced. Neglected in this comparison are the effects of recombination, which is used in more advanced approaches to evolutionary algorithms and also in AStRoTom. By combination of successful features of individuals, additional progress can be achieved, even in the case of inappropriate mutation stepsizes.

A Newton method in multidimensions would incorporate numerous quality determinations for calculating the derivative of the quality function in every dimension.

Powell's method (as implemented in Numerical Recipes), which doesn't need the derivatives, is faster than ES in terms of CPU time. But it doesn't allow to specify additional restrictions, like the intensity map to be positive at all points.

WD2001 and WAT2003 use the MEMSYS package (Skilling and Bryan 1984, Gull and Skilling 1991) in their Roche-tomography code. This is in principle a gradient method in the $\chi^2 \otimes S$-space. The general behaviour of this fitting-algorithm is described in Horne (1994).

All the deterministic methods (including the three methods mentioned above) tend to get stuck within a local minimum, if the quality-landscape is not shaped nicely. This risk exists for ES as well (due to the adaptation of the step-sizes). However, by applying gaussian distributions for the modifications of the step-size and the data, there is a non-vanishing probability to leave a local minimum and find the global one. For quality-landscapes with lots of local minima one could use an ES with multi-modal optimisation. In this approach multiple populations are created out of one, and are optimised seperately for a specified number of generations. Afterwards the results are compared and maybe combined, to form the starting point for new separate populations. This is not implemented in AStRoTom yet.

When using random variations for the optimisation, like in ES, each optimisation run is different and leads to different results after the same number of iterations. For a large enough number of iterations – what this means depends strongly on the shape of the quality landscape and the dimension of the problem – the probability is high to end up in the vicinity of the result of a different run. But there is the chance that the procedure gets stuck in a different (local) minimum. A quantitative approach to estimate the reliabilty of the fits is called 'bootstrapping' and is described in 2.2.4.

For more information on Evolution Strategy I recommend reading the ENCORE compilation of material concerning evolutionary computation (e.g. at *http://surf.de.uu.net/encore/*). A book in german on evolutionary algorithms in general exists also (Weicker, 2002).

Fine-tuning with Powell's Method From the considerations mentioned above, the idea arose to apply a deterministic method for fine-tuning of the results after the ES. To be able to implement Powell's Method it was necessary to extend the domain of the intensity map values from just positive ones to real numbers. For all projections of the map and the quality determination (i.e. entropy calculation), the absolute values of the intensity map are used.

It proved that Powell's Method is able to enhance the quality of the fit beyond the one achieved with ES, when the ES already converged. When applying it without running the evolution first it is converging (i.e. finding a local minimum), but it turned out that in most cases, from the same starting point in parameter space (most probably not inside the global minimum) it was not

able to fit the data as good as the ES alone.
Thus the presumption seems to be proven that the deterministic methods (at least this one) have more problems in finding the global minimum than ES, but are better suited for optimisations inside a local minimum.

2.2.4 Performance tests

Artificial maps were used to test the program's ability to reproduce structures and to test the convergence behaviour of the ES.

Simple maps created with this program

As a first test, a simple map created with AStRoTom itself was used to proof the ability to reproduce a map from a trailed spectrum. The map was calculated for an inclination $i = 50°$, using a Gaussian as intrinsic line-profile and folding the resulting spectrum with a Gauss curve representing an instrumental response. The map and the – successful – reproduction are shown in Fig. 2.9.

The fit clearly reproduces the global structure of the test map, with the emission arising on the 'unirradiated' hemisphere only. The sharp boundary between the emitting and non-emitting region in the test map is softened – a result of the entropy involved in the quality definition. The entropy is necessary to prevent the program from over-fitting the data. As can be seen in the reproduction of the emitting region, additional sub-structure is introduced, especially on those parts less visible for an inclination of 50 degrees. There the highest intensities (a factor 1.5 heigher than in the input map) are found – a result of the weaker restricion of intensities for map tiles visible for a small phase range only. A reasonable value of the weighting parameter for the entropy, α, which leads to a good fit to the data and a relatively smooth map, has to be chosen by the user.

Simple maps created with other programs

With another program trailed spectra of emitting parts of the Roche-surface were calculated: first the 'irradiated' surface (test map A), where the emission-line intensity is weighted by the irradiation angle, and the 'non-irradiated' surface with all its pixels set to a constant value (test map B). The program used for the creation of the spectra calculates them differently from AStRoTom: It uses a higher resolution of the surface but no intrinsic line profile. Also it does not fold the resulting spectrum with an instrumental response. The trailed spectra have a velocity binning of 12.5 km/s and a phase resolution of 0.01.
For the fit, the Roche-lobe was sampled with 20×20 surface elements. The intrinsic line-profile was assumed as a Gaussian with 10 km/s for map A and with 20 km/s for map B.
The structure of the synthetic maps was reproduced well, as can be seen

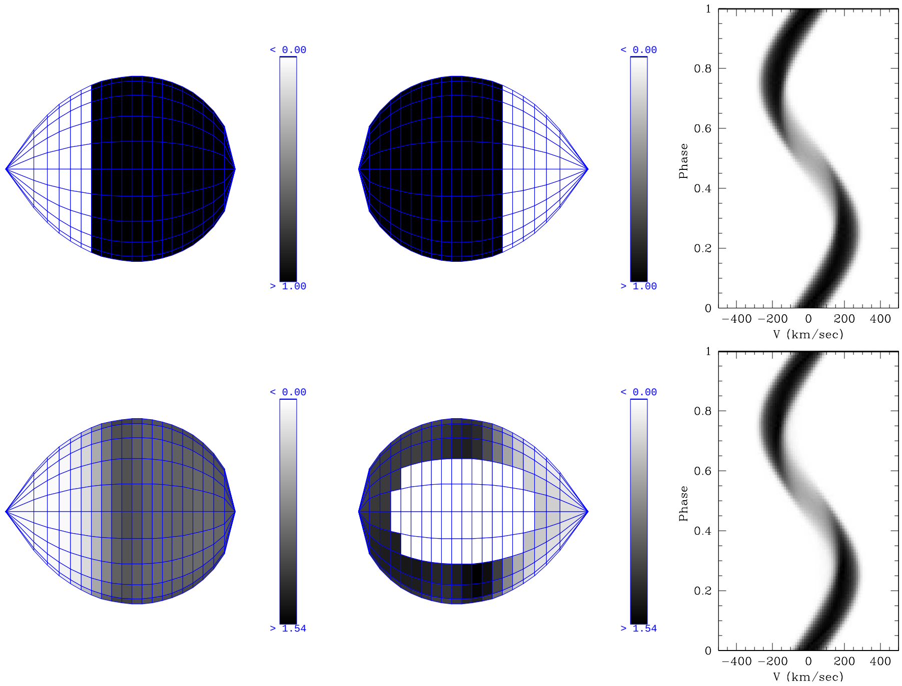

Figure 2.9: Roche-tomography: Reproduction of a simple test map. The parameters i, Q, M_1, and the intrinsic line width were the same for original (top) and reproduction (bottom). The parameter for weighing the smoothness (α) and the aim for χ^2 were set in a way, that there is not too much substructure in the reproduction. (*left*: view from top, *middle*: view from bottom) The cut values are set to minimum and maximum of the respective map. In the original map, the maximum (in black) is at 1.0, whereas it is at 1.54 in the reproduction. The white tiles at the bottom are the surface elements which are never visible at the inclination $i = 50°$. The trailed spectra on the right are the projected input map (top) and the fit (bottom).

in Fig. 2.10. The residuals show that the line profile is broader in the fit. Also sharp edges are smeared out. There are two reasons for this: First, the intrinsic line-profile is assumed to be the same for all elements, independently of whether they are looked at under a viewing angle of 90 degrees or 1 degree. Thus the intensity is wider spread in v for elements at the limb when using the intrinsic profile than in case of the program used for the creation of the spectra. (There the range in v, over which the emission from an element near the limb is spread, is infinitely small.) Additional smoothing is introduced by the entropy as an additional criterion, which penalises sharp edges in the intensity distribution. This is unevitable, because without it the map would consist of isolated pixels with a high brightness among pixels with no intensity at all.

One also sees that the code tends to put more intensity into pixels which are at one phase perpendicular to the line-of-sight. This behaviour was not reported by WD2001 and WAT2003.

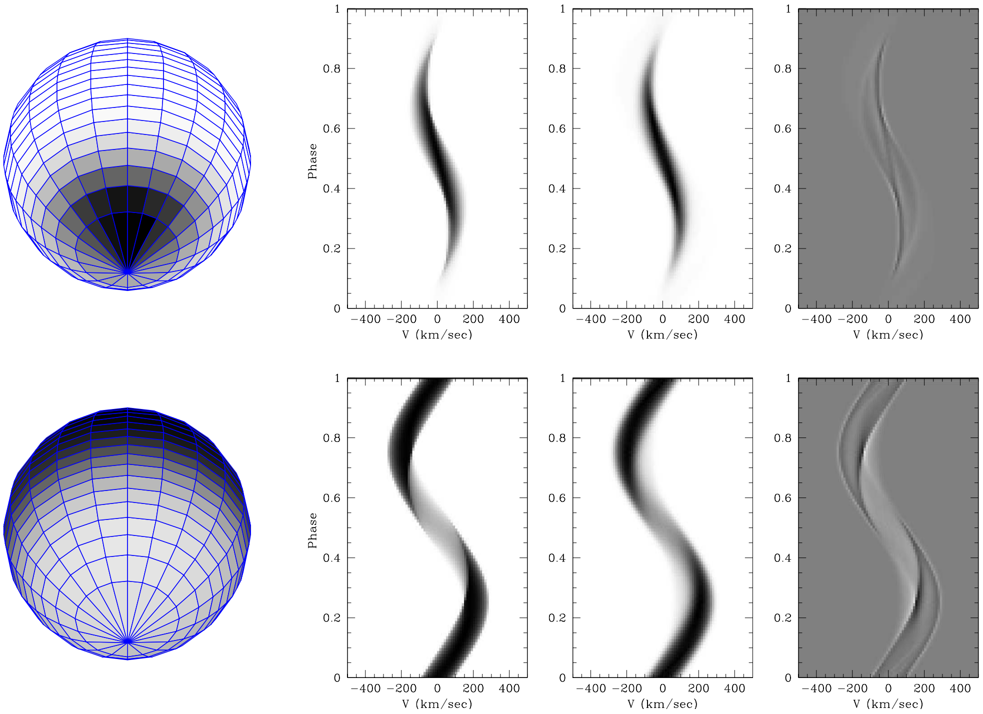

Figure 2.10: Fits to synthetic data (1): The reconstructed synthetic intensity maps for an irradiated Roche-lobe under 50° inclination (as for the creation of the spectra) at phase 0.5, *top*: test map A, *bottom*: test map B, the original spectra, the fits and the residuals. (left to right; black means strongest emission, white no emission; dynamic range in residuals the same as in the spectra, but zero is gray)

The choice of the MEM default-map

If Maximum Entropy methods are used, it is necessary to define a default map. The entropy is calculated with respect to this map (Eq. 2.4). In this section I describe how the use of two different entropy definitions influences the reconstruction of two test maps.

To my knowledge two kinds of maps are commonly used: the homogeneous map, whose intensity is adjusted to the average of the actual map (e.g. WAT2003) or a smoothed version of the actual map (e.g. Steeghs, 2003). For special geometries one can use less general default maps, e.g. a radially symmetric one in the case of accretion disk mapping.

The definition of the map doesn't affect the calculation of χ^2. Nevertheless, it has influence on the solution found: The homogeneous map biases the result to a uniform intensity map, as can be seen in Fig. 2.11, where I show results of fitting-runs with both approaches, smoothed and homogeneous, which have the same value of χ^2.

Although the homogeneous default map favours a levelled-out map, it can

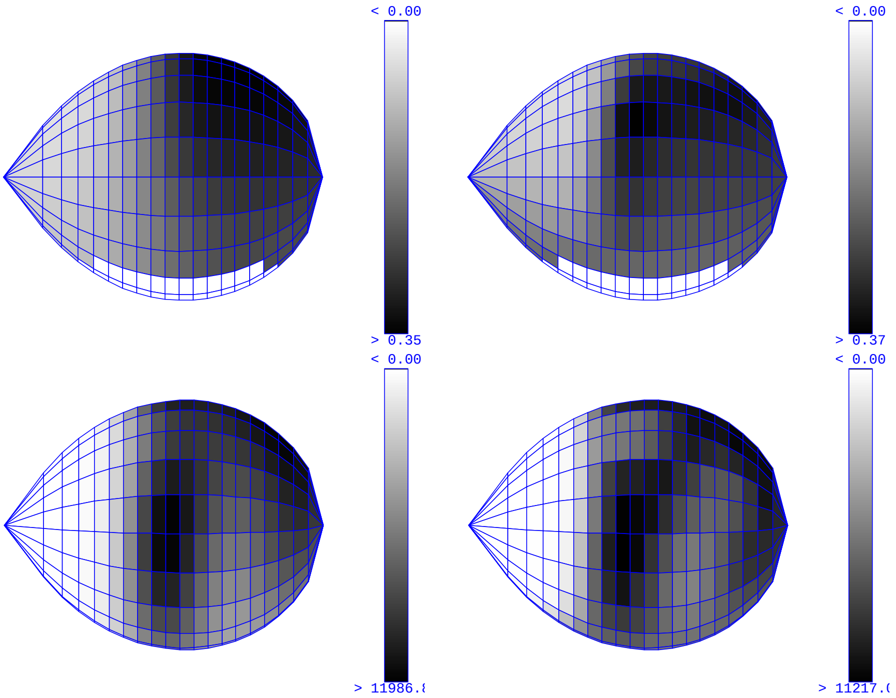

Figure 2.11: Different resulting maps for different default map definitions:
top: The input spectrum was the lower one from Fig. 2.10. *left*: with the default map being a smoothed version of the actual data map, *right*: with a homogeneous default map, whose intensity is the average value of the data map. The maps are shown at phase 0.75 for 90° inclination, although calculated for 50°. The white regions on bottom are the pixels which are never seen at 50° inclination. Both maps result in the same χ^2.
bottom: Fits to the same input spectrum (from test map #2, see Fig. 2.13, shown at $i = 50°$): *left*: with the default map being a smoothed version of the actual data map, *right*: with a homogeneous default map at average level. Although both reach the same χ^2, the structure resolved in the map is less for the smoothed-map approach. But additional structure is created in the right map to counter-act the effects of trying to make the map homogeneous.
The greyscale values are spanning the whole intensity range from minimum to maximum in the maps. The actual values are depending on the line-flux in the input spectra, which is the reason for the vastly differing ranges for the two maps.

be seen that there is more substructure on the emitting hemisphere than in the case of the smoothed map. The reason is, that for obtaining a good χ^2 this is necessary to counter-act the excess intensity in those pixels which at all phases contribute weakly to the spectrum (i.e. the ones near L_1 on the 'southern' hemisphere), but are preferentially set to the default level (top right panel.

I prefer the smoothed map approach, because it assumes nothing concerning the global shape of the intensity distribution. Especially in the case of highly inhomogeneous flux maps an unbiased approach is preferable, to avoid artificial

substructure introduced by the fitting procedure. If better data were available for more homogeneously emitted lines, the homogeneous default map could be appropriate to detect star spots.
The chosen smoothing radius of one pixel is the smallest possible restriction to the fit of the data, allowing sub-structures of all kinds to form in the map. With growing smoothing radii the default map converges to the uniform map.

Structured maps

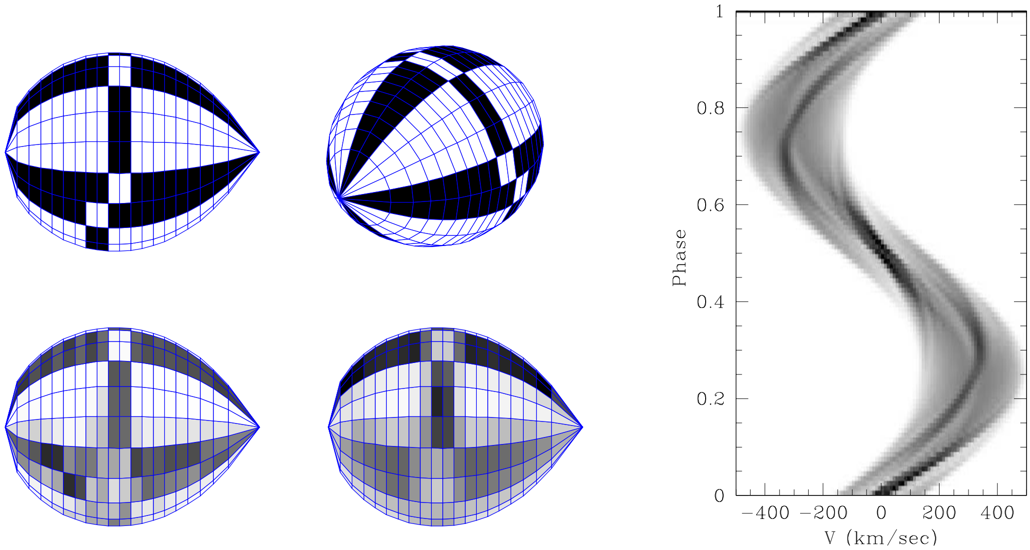

Figure 2.12: The structured test map #1, shown at phases 0.75 and 0.38 with $i = 60°$ (top), the projected spectrum (right), and two reconstructions (bottom) with a very low weight of the entropy (left), and with the entropy (Eq. 2.4) taken into account more strongly (right)

For testing the ability of the code to reproduce substructures on the Roche-surface, two test maps were created and projected with AStRoTom. Map #1 consists of bright stripes on a dark surface with dark spots at the intersections (Fig. 2.12). It was projected with $i = 60°$, $Q = 2.0$, $M_1 = 1.0\,\mathrm{M}_\odot$, and $P_{orb} = 7200\,\mathrm{s}$ into a trailed spectrum with 100 phase bins and a pixel size of 10 km/s (also Fig. 2.12). An intrinsic line-width of 30 km/s FWHM was used. For the reproduction with AStRoTom, the binary parameters and the line width were set to the original values.
The sharp features with high contrast present in the test data are difficult to reproduce, as is expected when using a MEM-approach. The contrast in real data is likely to be much lower, and the features shouldn't have such sharp edges, making the MEM-approach more suitable. But, of course, the signal-to-noise ratio has to be quite high to be able to resolve the less prominent sub-structure.

Deviating system parameters

I investigated the effects of system parameters for the fit which are slightly changed from the ones used for the calculation of the input spectrum. The effects of are shown in Fig. 2.13 for a test map representing a model for the distribution of sodium absorption on the secondary's surface (test map #2). The line originates only on the 'non-irradiated' hemisphere and there are spots where the line is less strong. The Roche-lobe was divided into 20×20 elements, and a Gaussian with a FWHM of 30 km/s was used as the intrinsic line-profile of each. The resulting spectrum was folded with a Gaussian of FWHM = 30 km/s, representing the instrumental resolution. A pixel size of 12.5 km/s and 100 phase bins were used for the resulting spectrum.

All changes in the parameters lead to a redistribution of the emission. For the same value of χ^2_{aim}, the entropy finally reached was much smaller than for fitting with the original parameters. To achieve the relatively smooth maps in Fig. 2.13, χ^2_{aim} was increased.
The changes resulting in a different velocity range covered by the Roche-lobe (changes in i, M_1, and Q), are creating a bright and a dark band nearly parallel to the equator. If the maximum velocity becomes smaller, the emission moves to the equatorial plane and a dark band forms on the bottom because of the conservation of the over-all flux. For a larger maximum velocity, the opposite effect occurs, creating a dark band in the equatorial plane and shifting the necessary emission to the bottom.
As expected, a deviating system velocity γ results in a redistribution of emission from the leading to the trailing hemisphere, or the other way round.
The effects for emission on the irradiated hemisphere are the same – it all depends on the velocities which can be reached at a certain phase and whether there is emission in the spectrum at this position or not.

These effects are discussed in detail also by WD2001. They also illustrate the expected degradation of the fitted map by a lower sampling in wavelength and phase. As expected, also incomplete phase-coverage leads to a reduced quality of the map.
For an inclination near 90°, it is impossible to distinguish between features arising on the northern or southern hemisphere. In such a case the calculated map will be symmetric with respect to the orbital plane.

Maps with noise

So far idealised data with an infinite S/N were used. For testing the dependence of the fit and its stability from noise in the data, I created noisy spectra from the test map #2, shown in Fig. 2.13. The noise added to the artificial spectrum has a Gaussian distribution.

As can be seen in Fig. 2.14, noise doesn't affect the over-all appearance of the fits much. Of course, the fit cannot reproduce structures which are represented by information in the trailed spectrum below the noise level, and the final value of χ^2 is growing with lower S/N, although the same value χ^2_{aim}

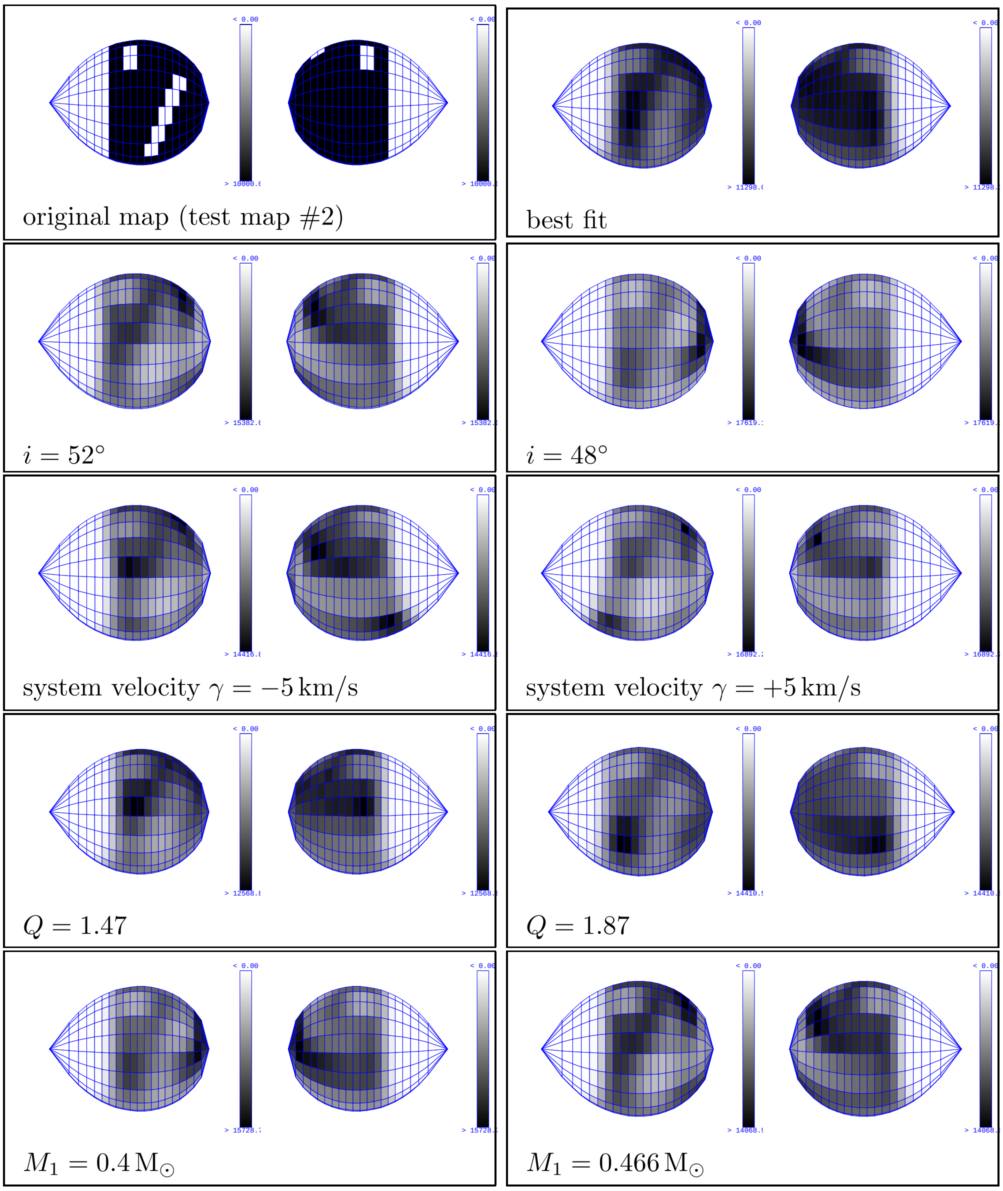
original map (test map #2)

best fit

$i = 52°$

$i = 48°$

system velocity $\gamma = -5\,\mathrm{km/s}$

system velocity $\gamma = +5\,\mathrm{km/s}$

$Q = 1.47$

$Q = 1.87$

$M_1 = 0.4\,\mathrm{M}_\odot$

$M_1 = 0.466\,\mathrm{M}_\odot$

Figure 2.13: Roche maps for the original and deviating system parameters, shown at phase 0.25 and 0.75 under the correct inclination. The parameters for generating the input spectra were $i = 50°$, $M_1 = 0.433\mathrm{M}_\odot$, and $Q = M_1/M_2 = 1.67$. Because of the deviating parameters there was not one value of χ^2 that could be reached by all runs and that would reproduce the input structure of the bright hemisphere with dark spots. Thus a χ^2_{aim} was used in each run, which reproduced the substructure and produced a relatively smooth map. The greyscales in the plots represent all values between minimum and maximum in each map.

was used. The entropy is increasing with larger values of χ^2 reached. The reason for S being lower for S/N=3 than for S/N=10 is a reduction of the weight factor of the entropy, α, by a factor of 10 compared to the latter case, which was necessary to get χ^2 below 1, and thus achieve a decent fit to the data.

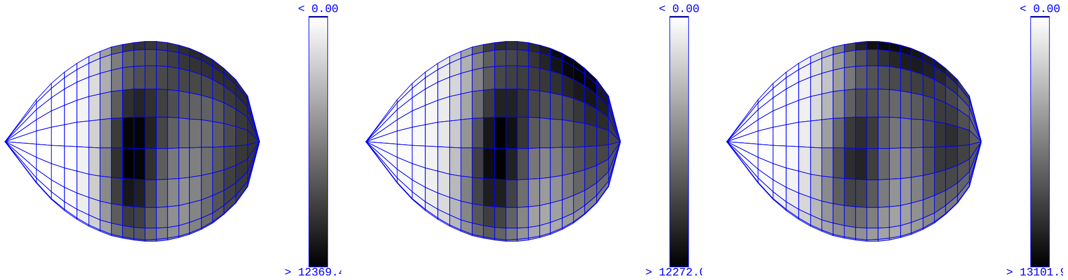

Figure 2.14: Reproductions of test map #2:
left: without noise, reaching $\chi^2 = 0.54$ and an entropy $S = -4270$,
middle: with a noise level of S/N=10, reaching $\chi^2 = 0.71$ and an entropy $S = -3052$,
right: with a noise level of S/N=3, reaching $\chi^2 = 0.88$ and an entropy $S = -3967$

On the reliability of the fits: bootstrapping

For quantifying the quality of the fit and the relevance of structure resolved in the maps, it is desirable to calculate the errors of the intensity for every map element.

Formally one could use the error propagation formula to determine them, but not all requirements are fulfilled in the case of Roche-tomography. First, the errors are not independent but correlated. This is caused by the assignment of velocities in the spectra to map elements along arcs, which vary with orbital phase, as well as by the use of the MEM approach, which correlates the map elements via the default map (WD2001).

The effective number of free parameters strongly depends on the choice of the default map and the chosen value of α and cannot be quantified generally (Horne, 1985). Thus the calculated value of the normalised χ^2 doesn't have much statistical meaning when normalised to the number of data points N, and can reach values below 1, even if the errors are known exactly. From a statistical point of view it would be more appropriate to divide the χ^2 by $(N - M)$, to account for the reduced number of free parameters due to the fit with M independent map parameters, but the reduction of these by the smoothing would still not be incorporated.

For getting an estimate of how much of the structure seen in the maps is real substructure present in the observed data and not just one representation of multiple possibilities to fit the data, I use a version of the bootstrap method (see Efron and Tibshirani, 1993), which is described by WD2001: From the observed trailed spectrum (with N data points) N points are randomly selected, allowing multiple selections. The errors of the selected points are reduced by the square root of their hit-frequency, thus making points selected more than once more significant and the unselected ones completely insignificant. This is done e.g. 200 times, and the fitting procedure is applied to each spectrum with the same input parameters. This method doesn't change the over-all noise-level for the modified spectra compared to the original one, and is thus preferable to an approach modifying the spectral values and not the errors only.

From the resulting maps of all runs, the most probable value for each map element and the size of the interval centered around this value and containing 95% of all the values is determined. Half the width of the interval is considered the error of the fit, following more the idea described by WD2001 than the one which they used later (WAT2003).
The distribution of values around the most probable one is not Gaussian, so the statistical quantities σ and FWHM are not applicable. The quantity I use can be considered as the maximum error.

The reliability of the structure is then determined by dividing the map of the errors by the fitted map, after subtracting a constant value from the latter one, which defines the comparison level. All structures which show a ratio of considerably less than 1 can be considered as trustworthy with respect to the comparison level.

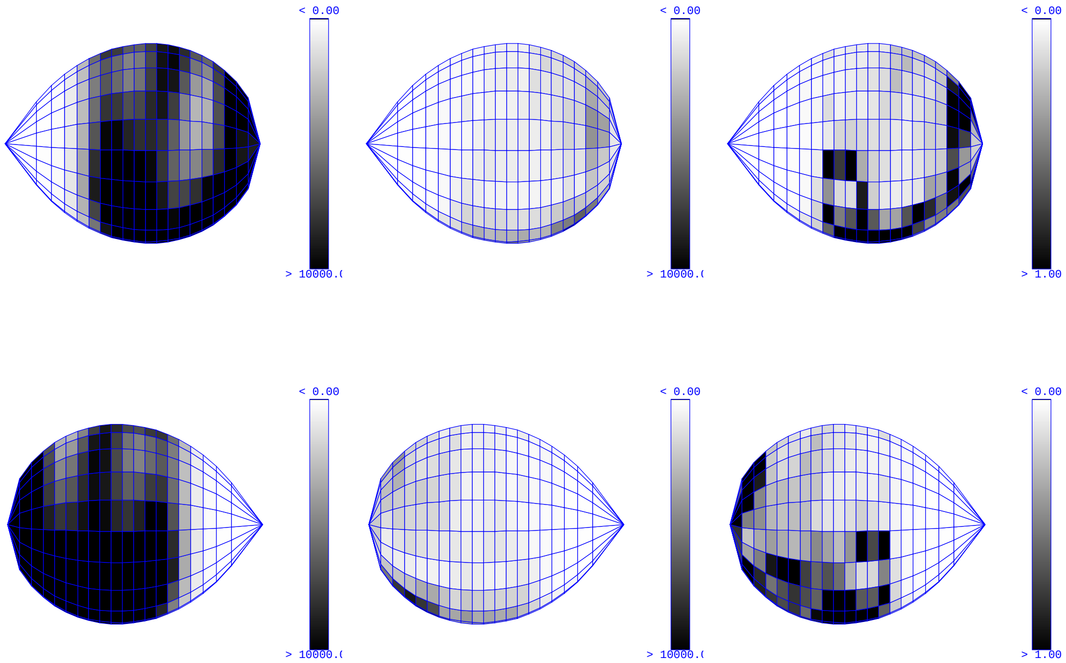

Figure 2.15: Test results of the bootstrap for the spectrum corresponding to map #2 (Fig. 2.13): **top**: view at phase 0.25, **bottom**: view at phase 0.75, *left*: one arbitrarily chosen intensity map out of the 200, *center*: the resulting errors of the intensity map, *right*: the relevance map for a comparison level equal to the mean value of 10 slides in the 'unirradiated' hemisphere

For the spectrum from test map #2 (Fig. 2.13), I calculated 200 maps and created out of them the maps of error and relevance (Fig. 2.15). As can be seen from the relevance map, the 'star spots' are clearly detected (relevance much smaller than 1), whereas the substructure in the intensity map is specific to this particular fit and cannot be trusted.

Using the bootstrap method, it is possible to estimate the statistical uncertainties of fitting with Evolution Strategy, which are arising from both, the noise in the data and the random variations during the fitting procedure. But apart from this, substructure can be intruduced by not perfectly known system parameters and by a not appropriately chosen value of α.

Estimates of requirements to detect substructure

To get an estimate of the requirements on the data, which have to be fulfilled to be able to resolve sub-structure on the Roche-lobe, the projected spectrum of map #2 (Fig. 2.13) was used.

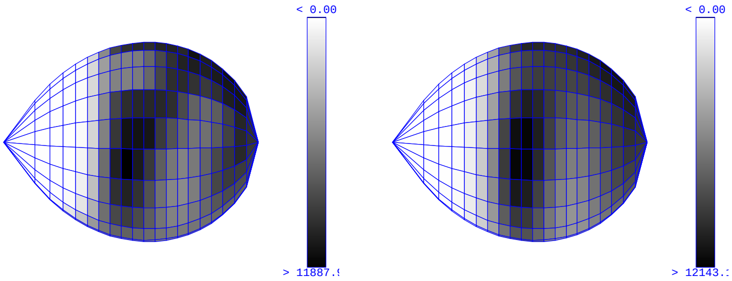

Figure 2.16: Tests of resolving substructure with AStRoTom (1): map #2 reproduced
left: with the homogeneous entropy default map, *right*: with the smoothed default map. (Both fits have nearly the same χ^2.)

First it was checked which default map is suited better to reproduce substructure in the maps. Fig. 2.16 shows that at the same χ^2 of the fit the homogeneous default map reproduces the sub-structure more clearly. The global structure is nevertheless better reproduced by the smoothed map, because the homogeneous map assigns the average intensity to the pixels less visible.

The influence of noise on the detection of sub-structure has also been studied. Therefore a gaussian distributed noise was added to the artificial spectrum created out of map #2. Two signal-to-noise (S/N) levels [5] have been tested: S/N=10 and S/N=3.
Fig. 2.17 shows fits with the homogeneous default map and the respective relevance maps with respect to the average level of the 'unirradiated' hemisphere.

It is clearly seen that the relevance-level of the reproduced substructure is much lower in the case of the noisier data: While in the case of S/N=10 the

---

[5] The signal-to-noise level here gives the ratio of the brightest pixel in the trailed spectrum to the σ of the gaussian distribution.

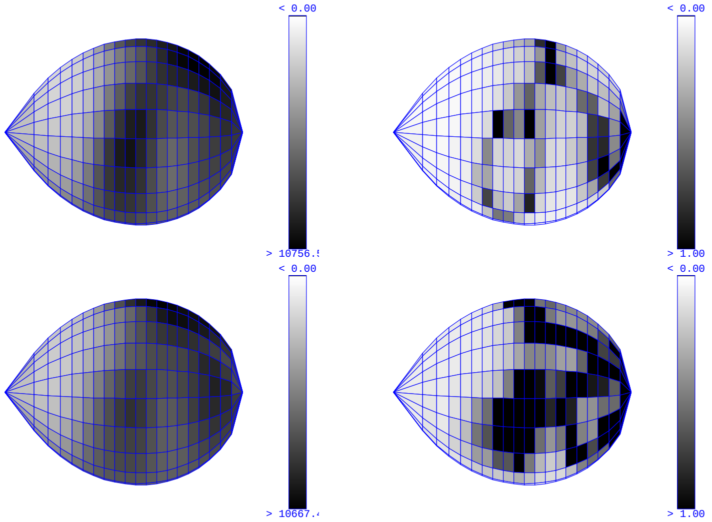

Figure 2.17: Tests of resolving substructure with AStRoTom (2): map #2 reproduced from noisy spectra with S/N=10 (**top**) and with S/N=3 (**bottom**): *left*: the reproduced map, *right*: the relevance map

'star spots' are detected above the intrinsic noise level of the reproduction process (relevance values below 1), for S/N=3 the relevance map has much more points with values larger than 1, marking them as not trustworthy, although the 'star spots' are still visible in the intensity map.

The noise found in observed data is certainly not Gaussian (for instance because of the Poissonian photon-noise component), and during the reduction process some artifacts will be created in the data as well. Thus any estimate calculated with artificial spectra and Gauss-noise cannot be quantitatively applied to real data.

The calculations, however, show that the noise level has a large influence on the resolvable substructure, and that the bootstrap method is capable to indicate the cases, where results of the mapping process have to be interpreted with caution.

2.2.5 Determination of system parameters

A map with larger entropy at same χ^2 is assumed to be more likely (maximum-entropy assumption). Thus one can try to determine the fundamental system parameters inclination i, mass ratio $Q = M_1/M_2$, and M_1 by determining the maximum entropy values reachable for a pre-defined χ^2 for different parameter combinations. This assumes that the real system parameters will provide the smoothest map, because deviating values would result in additional substructure in the maps, which are necessary to reproduce the spectra. The test with deviating system parameters (see there) seems to prove this assumption.

The parameter χ^2_{aim} defines the χ^2 level, on which the smoothest map is sought. I determine its value with a fitting run for a probable parameter combination (in case of artificial data the original one) without the entropy being taken into account. Its value is set such, that for a wider range of system parameter combinations around this probable one, the χ^2 reaches the 10% interval around χ^2_{aim}, and the entropy-distribution is steep enough to find a clear maximum. Nevertheless, χ^2_{aim} and α are free parameters whose exact values are chosen manually.

It is not possible to use the bootstrapping method to distinguish between 'good' and 'bad' system parameters, because it only determines the relevance of map features with respect to noise in the data and uncertainty created by the random variations during the fitting process. This relevance is calculated with respect to a mean of maps calculated for identical system parameters. With bootstrapping it is thus not possible to determine any 'absolute relevance' of map features.

Parameter determination from artificial spectra

Spectra created by AStRoTom For testing the ability to determine the correct system parameters, first artificial spectra were created with AStRoTom from three intensity maps: a uniform one (A) and two with emission either from the 'non-irradiated' (B) or 'irradiated' hemisphere (C), as shown in Fig. 2.18. In the latter two cases the emitting tiles all have the same intensity. All maps consist of 20×20 tiles.

The artificial spectra were created with an inclination of $50°$, a mass ratio of $Q = 1.67$, and a primary mass of $M_1 = 0.433\,\mathrm{M}_\odot$. The intrinsic line profiles were set to 20 km/s, 30 km/s, and 10 km/s, repectively, accounting for the different sizes of the elements on the two hemispheres in velocity coordinates. For the instrumental resolution a Gaussian with a FWHM of 30 km/s was used.

For the fitting runs, all parameters were kept at the values used for the creation of the spectra, except the mass ratio, the inclination, and the primary mass. A fitting run was started for every combination of the values $Q = \{1.5, 1.55, 1.6, 1.65, 1.7, 1.75\}$, $i = \{45, 47, 49, 51, 53, 55\}°$, $M_1 = \{0.36, 0.39, 0.42, 0.45, 0.48, 0.51\}$.

χ^2_{aim} was set to 0.5 in case A, and to 1.0 in the two other cases. These values and the values of α were chosen such, that for the exact parameter combination χ^2_{aim} was reached and the map was smooth enough to resemble the input map.

The results are shown in Fig. 2.18 as slices of the cube of entropy values in the planes of constant Q, i, and M_1, respectively, which contain the highest entropy value.

It has to be noted, that only in the regions coloured gray χ^2 reached a value with less than 10% deviation from χ^2_{aim}. The entropy values for more deviating values of χ^2 have been coloured white, the maximum black.

The highest entropy in case A (uniform map) was achieved for the parameter combination $Q = 1.65$, $i = 49°$, $M_1 = 0.45\,\mathrm{M}_\odot$.

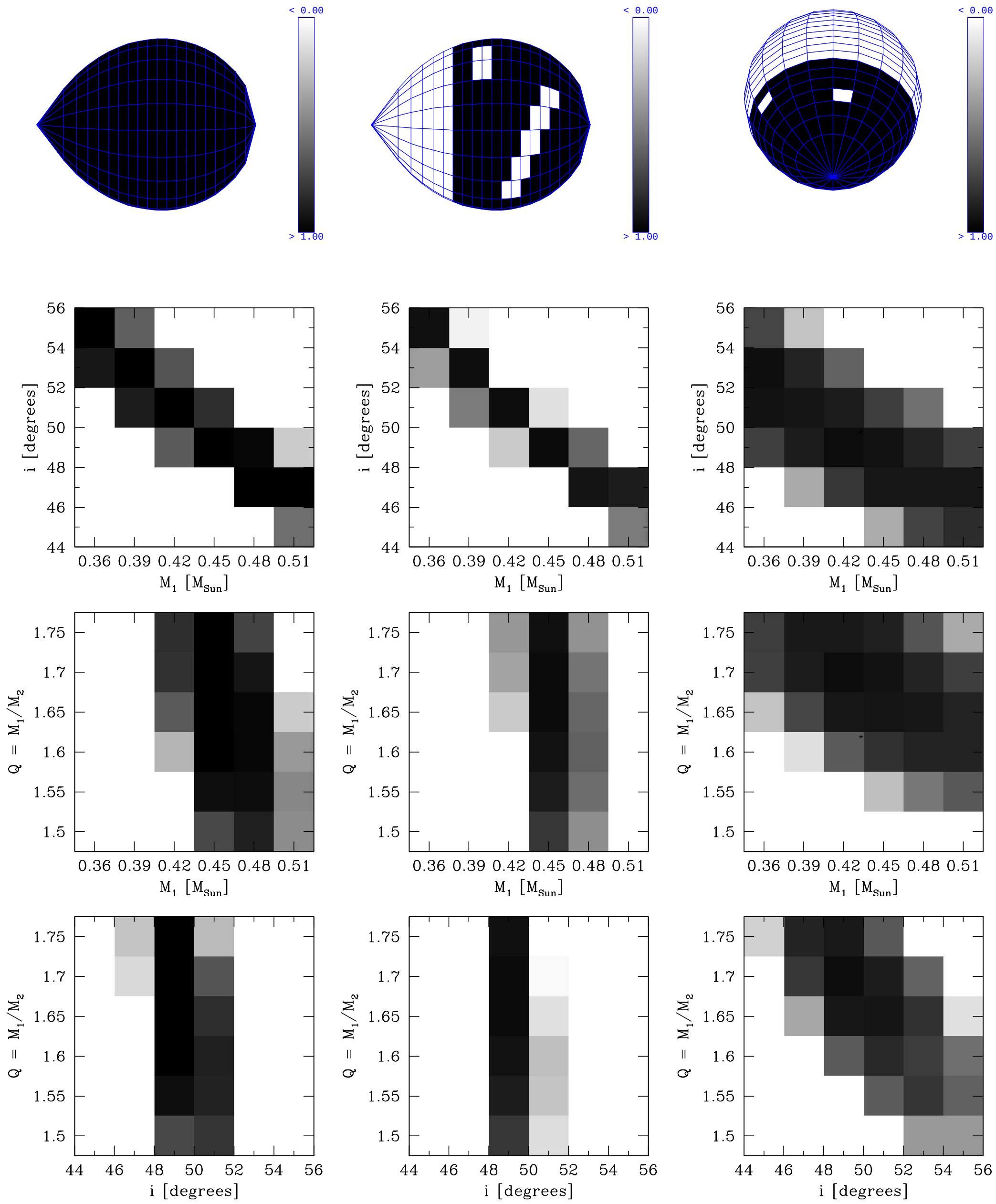

Figure 2.18: **top**: The three test maps for the parameter determination with AStRoTom, shown at $i = 50°$: *left*: (A), shown at $\phi = 0.25$, *middle*: (B, same as in Fig. 2.13), shown at $\phi = 0.25$, *right*: (C), shown at $\phi = 0.5$
Below, the resulting entropy distributions with respect to the system parameters Q, i, and M_1 are shown as slices of the data cube, which are containing the best-fit value for each map: $Q = const.$-plane (*upper middle*), the $i = const.$-plane (*lower middle*), and the $M_1 = const.$-plane (*bottom*). Black denotes higher entropy.

As default map the smoothed actual map was used. The uniform default map lead to similar results. The system parameters were even better restricted in this case, but this is not surprising, because for the exact system parameters the best fit is identical to the default map, whereas the deviations from uniformity grow rapidly for slightly changed parameters.

In case of map C, the approach with the uniform default proved to be inefficient, because it didn't find the exact parameter combination and reached the highest entropy on the edge of the parameter range. For map B, the smoothed map as well as the uniform default proofed to be appropriate.
The highest entropy in case B ('unirradiated' hemisphere, test map #2) was achieved for the parameter combination $Q = 1.65$, $i = 49°$, $M_1 = 0.45\,\mathrm{M}_\odot$, calculated with the smoothed default.
The highest entropy in case C ('irradiated' hemisphere) was achieved for the parameter combination $Q = 1.7$, $i = 49°$, $M_1 = 0.42\,\mathrm{M}_\odot$, calculated with the smoothed default.

These test runs give evidence of the program's ability to determine system parameters from trailed spectra under the assumption that at the same χ^2-level a smoother map is more likely to represent the real parameters.
The deviations in the determined parameters were in all three cases below the resolution of the parameter grid.

Spectra created by AStRoTom with noise To test the ability of Roche-tomography to determine the system parameters in the case of noisy data, artificial noise according to a Gaussian distribution was added to the projection of map B. Two signal-to-noise levels were considered: S/N=10 and S/N=3.

The slices through the entropy landscape containing the minimum are shown in Fig. 2.19. In case of S/N=10.0 this minimum was found at $Q = 1.7$, $i = 47°$, $M_1 = 0.48\,\mathrm{M}_\odot$, for the noisier data at $Q = 1.65$, $i = 49°$, $M_1 = 0.45\,\mathrm{M}_\odot$.
For the low noise-ratio, the entropy distribution still allows the approximate determination of the system parameters, although the largest entropy value is not reached closest to the initial parameters.
For the run with S/N=3, χ^2_{aim} had to be set to a higher value, and – to be able to start the iteration – the weight of the entropy had to be decreased. Although all values of χ^2 lie within the range of 0.05 per cent of χ^2_{aim}, the entropy distribution is not very smooth and doesn't restrict the possible parameter values efficiently.

Spectra created with another program To test the reliability of the reproduction, the best-fit parameters are determined for the spectra shown in Fig. 2.10. These spectra were created with a different program using a deviating projection scheme (without an intrinsic line-profile but simply summing up the emission from a number of emitting spots – much more than map tiles used in AStRoTom).

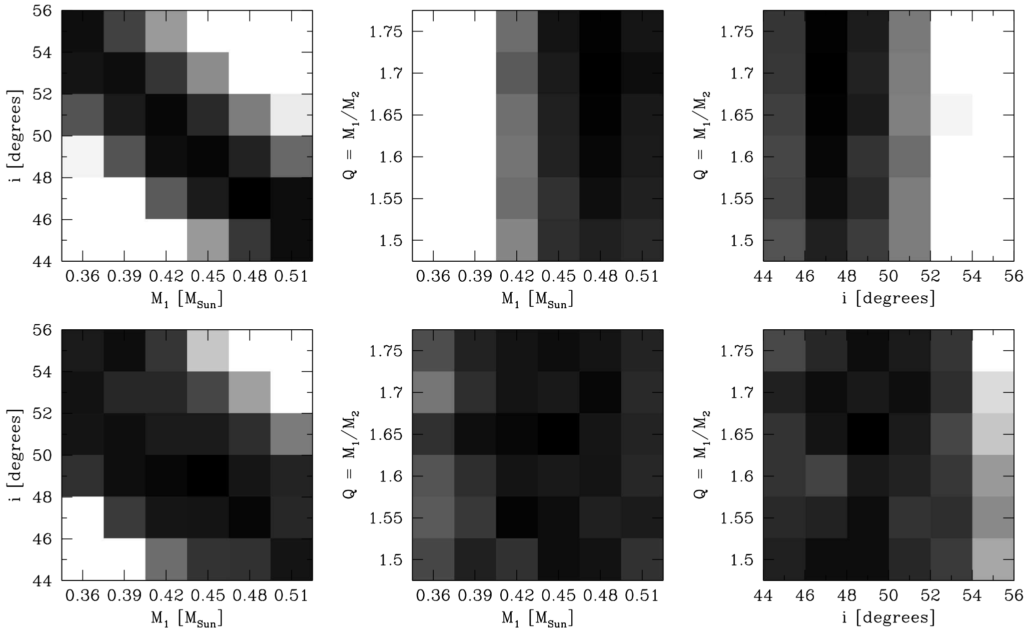

Figure 2.19: The entropy maps for noisy versions of the spectrum of map (B) (2.18) (top: S/N=10.0, bottom: S/N=3.0), with respect to the system parameters Q, i, and M_1 are shown as slices of the data cube, which are containing the best-fit value for each map: $Q = const.$-plane (*left*), the $i = const.$-plane (*middle*), and the $M_1 = const.$-plane (*right*). Black denotes higher entropy.

This test gives thus information whether the success of the parameter determination is relying on the reproduction of a map created with in intrinsic line-profile attached to the central point of a map element, or if the application of this projection in the reproduction is also appropriate for spectra created differently.

The system parameters for the creation of the spectra were $Q = 1.667$, $i = 50°$, and $M_1 = 0.433\,\mathrm{M}_\odot$. The trailed spectra had a velocity binning of 12.5 km/s and a phase resolution of 0.01.
For the fitting runs, intrinsic line widths of 20 km/s ('unirradiated') and 10 km/s ('irradiated') were assumed, to take into account the size of the surface elements in velocity space. The best fit in the case of the 'unirradiated' hemisphere was found at $Q = 1.7$, $i = 51°$, $M_1 = 0.42\,\mathrm{M}_\odot$– close to the original value.
For the 'irradiated' hemisphere the maximum entropy value is located at the border of the parameter range ($Q = 1.6$, $i = 45°$, $M_1 = 0.36\,\mathrm{M}_\odot$). Thus it was not possible to restrict the system parameters. The reason could be problems of the used entropy definition (smoothed map) with the shape of the entropy distribution created by this program (bright at L1, less intensity with smaller projected area seen from the WD).

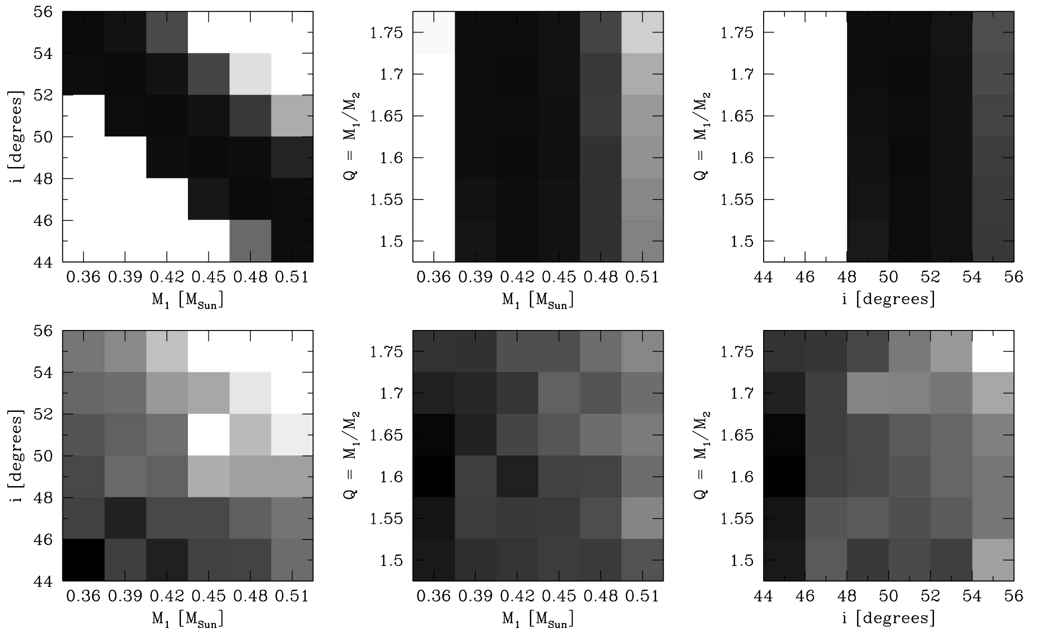

Figure 2.20: The entropy maps for the fits of the spectra from Fig. 2.10, **top**: 'unirradiated' side, and **bottom**: 'irradiated' side, with respect to the system parameters Q, i, and M_1 are shown as slices of the data cube, which are containing the best-fit value for each map: $Q = const.$-plane (*left*), the $i = const.$-plane (*middle*), and the $M_1 = const.$-plane (*right*). Black denotes higher entropy.

2.2.6 Comparison with other Roche-lobe mapping-techniques

Intensity maps of the sodium line on the secondary star surface in polars were created with other methods than Roche tomography as well, and were used to estimate the system parameters:

Southwell et al. (1995) presented a map of AM Her. The mapping procedure used there (see Davey and Smith, 1992) tries to reproduce the observed radial-velocity curve of the lines by summing up the Doppler-shifted and intensity-weighted line profiles of all surface elements. The observed radial-velocity curve was determined by cross-correlation with single M-star template spectra.

Additionally to this approach, Davey and Smith (1996) used the changes in the flux deficit of the sodium lines with respect to orbital phase to determine the intensity distribution on the secondary's surface. (Thus this method uses the line light-curve only, not the velocity information.) Both methods lead to similar maps and were used to estimate the system parameters of AM Her ($i = 50°$, $M_2 = 0.26\mathrm{M}_\odot$, $q = M_2/M_1 = 0.6$). For comparison, a map calculated with the Roche-tomography code of Rutten and Dhillon (1994) was presented, which was in good agreement with the maps from the other methods.

Catalán et al. (1999) combined the two methods of radial velocity fitting

and flux deficit fitting into one. It was used to calculate a surface map and determine the system parameters of QQ Vul ($i = 65°$, $M_2 = 0.3 M_\odot$, $q = M_2/M_1 = 0.54$).
The advantage of Roche-tomography over the above described methods is, that it uses all the information in the spectral line: the velocity shift, the changes in line flux, and – additionally to the methods mentioned above – the line profile changes. The measured line profile is thought to be the sum of the intrinsic line profile of every visible surface element at any phase.

2.2.7 Summary

My implemetation of Roche-tomography – AStRoTom – proved to be able to reproduce synthetic intensity distributions from projected spectra, created with both, AstRoTom itself and another program.
The influence of noise in the data on the reproduction was studied, as well as the impact of different system parameters used in the creation and reproduction of the maps.
A bootstrap algorithm was applied to measure the reliability of reproduced structure. It provides the ability to distinguish between map-structure really inherent in the data and artifacts of individual fit-runs.
For synthetic data created with AStRoTom, the determination of the system parameters with entropy-maps lead to values close to the ones used for creation of the spectra, also for data with added noise. In the case of synthetic spectra created with the other program, the correct system parameters could only be found for the 'unirradiated' hemisphere, for which uniform emission was assumed. In case of the spectra for the 'irradiated' hemisphere, the highest entropy value was achieved at the rim of the parameter range, so the system-parameter values could not be restricted. The reason for this behaviour could be the emission law used in this program for the irradiated hemisphere.

2.2.8 Discussion

The values of α and χ^2_{aim}, which determine the weight of the entropy in the quality, have to be chosen manually. Thus the amount of structure apparent in a Roche-map can be prejudiced. The sub-structure, which is just an artifact of one specific optimisation run, can be determined with the bootstrap method. The amount of sub-structure really present in the observational datacannot be easily quantified, since the choice of α has a strong influence on the reproduction, and the true value of χ^2 cannot be determined accurately because of the degeneracy of the quality function.

Contrary to the work by WD2001 and WAT2003, I decided to use a smoothed version of the data map as default for the entropy calculation. For the determination of star spots on an otherwise homogeneously emitting (absorbing) star surface, their approach is probably the better choice. But the distribution of the absorption and emission lines on the surface of the secondary star in polars is far from being uniform, as is clearly seen already in the trailed spectra.

In the case of the test map they presented (WD2001), the choice of a homogeneous default map is though appropriate, since they used a uniform map with smaller perturbations, mimicking the effects of star-spots and of shielding by the accretion stream/curtain. Also, their attempt to determine the correct system parameters from the achieved entropy values works well, because the emission is covering the whole stellar surface. Thus the system parameter combinations leading to both, a good fit to the data and a smooth map, are tightly restricted by the minimum and maximum radial velocities observed.

If the emission/absorption arises on the (un-)irradiated hemisphere only, the restriction works this strong only in one direction: In the case of absorption lines from the unirradiated hemisphere, the maximum velocity at which there is absorption in the trailed spectrum has to be in reach of the Roche lobe at this particular orbital phase. Thus only parameter combinations leading to smaller reachable velocities are effectively ruled out, but combinations resulting in higher velocities still work.

For emission lines arising solely on the irradiated hemisphere, the situation follows the same principle. Here the velocity of the L_1 point determines the minimum velocity which has to be accessible for the Roche lobe. Thus it restricts the system parameters to values which don't move the L_1 point to velocities larger than the measured minimum velocity. But there is no limit set to the minimum velocity with such a spectral line.

To determine the system parameters in the case of data where there are big differences between the irradiated and the unirradiated hemisphere, it is better to use data from both hemispheres, i.e. one emission line and one absorption line. The combined results from fitting runs on both data sets may give the correct values.

The problem with the emission lines from the secondary star is that they are superposed by emission from the accretion stream. There is no way of *a priori* disentangeling them. A possible solution could be a combination of Roche-tomography with a fitting algorithm, mapping the line emission from the accretion stream/curtain onto an assumed surface. Such code was developed by J. Vogel at the AIP during his Diploma thesis.

Future enhancements to the Roche-tomography code:

Due to the rotation of the system within a phase bin, the contribution of one surface element to a certain spectral bin is changing with time. The amount of change is dependent on the position on the Roche-lobe and on the actual phase angle. Also, the surface elements have a finite size. Thus they are emitting in a velocity range, not at just one velocity like assumed in my model. The velocity range is also dependent on the position on the Roche-lobe and on the phase angle.

In AStRoTom I try to compensate both effects by applying a Gaussian broadening to the line profile emitted with the properties of the element center. In the current version, the FWHM of this Gaussian is the same for all elements

and orbital phases. This is, of course, not exact and one has to select carefully a value which fits the actual system parameters. This is especially difficult in the case of entropy grids for the parameter determination.
For better results, the width of the broadening function should be calculated for each element at each phase. This will be implemented in a future version of AStRoTom.

For data with high signal-to-noise ratio it may be necessary in the future to include limb darkening into the code. Due to the difficulties arising from the Roche-lobe geometry and the complicated behaviour of limb darkening of absorption lines this cannot be regarded by a formula weighting the intensity, but has to be applied to the intrinsic line profile. A possible solution would be to use a grid of pre-computed synthetic line profiles from a radiative transfer code for the possible range of surface gravity and viewing angles. For the values between these calculated parameter combinations, the spectra could be interpolated.
There would still be problems due to the irradiation, which changes the temperature structure in the stellar atmosphere and thus the limb-darkening behaviour. In this case the use of a stellar atmosphere code would be of no use, because the amount of incident radiation is unknown (and looked for with Roche-tomography).

2.3 Requirements on the data for indirect imaging

For all kinds of tomography, data is needed which has a good signal-to-noise ratio and a good resolution in both, wavelength and time. The velocity-resolution of the input data limits the size, down to which structures can be resolved. The time-resolution controls how many spectra can be obtained within one orbital cycle. This defines the number of angles, under which the system is observed and how strong the spectra are smeared out due to the change in the projection during the exposures.
Getting appropriate data is difficult in the case of polars, since they are quite faint ($<14\,$mag), are orbiting in a relatively short time ($\sim 2...8\,$h), in which $\gtrsim 50$ spectra have to be observed, and one needs a spectral resolution of $\lesssim 100\,$km/s to resolve the secondary star in the absorption lines and the accretion stream in the emission lines. Thus only telescopes with a diameter of $\sim$4 meters or more can be used efficiently for obtaining high-resolution spectra useable for indirect imaging of polars.

Chapter 3

AM Herculis

3.1 The system

AM Her was detected as a variable star in photographic plate surveys (Wolf, 1925). The system was $13\overset{\mathrm{m}}{.}5$ in 1905 and measured unusually bright in 1919 ($10\overset{\mathrm{m}}{.}3$).
For a long time it remained unclear, to which type of variable stars it belongs. The long-term light-curves showed different brightness states with differences of up to 3 mag, which changed aparrently erratically (e.g. Götz, 1993). The system's brightness was measured as $U \sim 11\overset{\mathrm{m}}{.}5 \ldots 15\overset{\mathrm{m}}{.}0$, $B \sim 12\overset{\mathrm{m}}{.}3 \ldots 16\overset{\mathrm{m}}{.}0$, and $V \sim 12\overset{\mathrm{m}}{.}9 \ldots 16\overset{\mathrm{m}}{.}0$.
Hudec and Meinunger (1976) proposed the object to be identical with the *Uhuru* X-ray source 3U 1809+50. Berg and Duthie (1977) identified the object as a cataclysmic variable, but said to be "unable to distinguish between a U Gem or a Z Cam subtype".
A model by Chanmugam and Wagner (1977) proposed accretion onto the white dwarf (near a magnetic pole) without an accretion disk. The presence of a magnetic white dwarf was confirmed by Tapia (1977), who measured linear and circular polarisation, which he attributed to be originating from accreted matter in the magnetic field of a white dwarf. This model was refined by Stockman et al. (1977), who used the results of Lamb et al. (1973) to establish the accretion stream model with a ballistic and magnetically guided part. Thus the sub-class of AM Her-stars was invented.

A lot of effort was put into observing AM Her. Observations were performed in all possible wavelengths, including X-rays, UV, optical, IR, and radio. Optical polarimetry was performed as well. Here is a compilation of some results from publications based on different kind of observations:
X-ray data was obtained in different accretion states. Observations during an high state showed the maximum of the soft X-ray emission when the hard X-ray emission was zero. This was interpreted as two-pole accretion (Heise et al., 1985). Observations in intermediate states can be interpreted as accretion to just one active pole, while further observations during high states showed changing properties of the emission from the two accreting poles

(Matt et al., 2000). During an optical low-state the model fit to the observed X-ray spectrum was compliant with coronal emission from the seconday star only, and was thus interpreted as a complete turn-off of the accretion process (de Martino et al., 2002).

Polarimetric observations were used to get information on the accretion regions on the white dwarf's surface. Wickramasinghe et al. (1991) presented a two-pole accretion model, which was able to account for the observations presented in Heise et al. (1985) and previously published polarimetry, inferring a system inclination of $i \simeq 50°$.

Photometry obtained in the UV range resulted in further parameter determinations: Heise and Verbunt (1988): $HJD(\phi = 0) = 2443014.76614(4) + 0.128927041(5)E$, Sirk and Howell (1998) derived $i = 37°$, accretion spot latitude $\beta = 68°$, azimuth of the spot $\psi = 31°$, $B = 12\,\mathrm{MG}$. Gänsicke et al. (1998), analysing high state light-curves, obtained $\beta_{spot} = 54.4°$, spot azimuth $\psi = 0.0°$, $i + \beta = 105°$, $M_1 = 0.35 - 0.53\,\mathrm{M}_\odot$, $q = 0.38 - 0.74$, temperatures of the undisturbed white dwarf ($T_{wd} = 20000\,\mathrm{K}$) and the accretion spot center ($T_{max,spot,hs} = 47000\,\mathrm{K}$).

Gänsicke et al. (2001) combined the latter results with optical photometry to create a model for the observed B and V light-curves. As main source of variability in the V-band they derived cyclotron emission from a region near the accretion spot, whose adopted parameters are azimuth[1] $\psi = -12°$ and colatitude[2] between $\beta = 55°$ and $70°$. In the B-band there is almost no variation. The brightness of the secondary star was measured as $B = 18.43$, $V = 16.83$.

In spectroscopic data from the IR range, Bailey et al. (1991) detected cyclotron features and determined the magnetic field strength as $B = 14.5\,\mathrm{MG}$. Furthermore they gave values for the secondary's brightness: H=12.0, K=11.6.

UV spectroscopy during a low state gave further information on the white dwarf: temperature of the undisturbed white dwarf surface $T_{wd} = 20000\,\mathrm{K}$, temperature in the center of the accretion spot $T_{max,spot,ls} = 24000\,\mathrm{K}$, area of the accretion spot in terms of the surface area of the white dwarf $A_{spot} = 0.1\,A_{wd}$, distance to the solar system $d = 90\,\mathrm{pc}$ (Gänsicke et al., 1995).

During a high state, time-resolved spectra in the UV were obtained with HST, which could be used to create Doppler-tomograms (Gänsicke et al., 1998). The spectral line of Si IV showed a NEL at the expected position of the irradiated hemisphere of the secondary and an accretion stream, while the N V line contained a quasi-stationary component – matter near the centre of gravitation of the system. A similar measurement was reported by Hutchings et al. (2002), who reported a low-velocity NEL in the case of O VI.

Spectropolarimetry in the near-IR, presented by Schmidt et al. (1981), gave M4.5-M5 as spectral type of the secondary, a distance of $d = 80 - 100\,\mathrm{pc}$, and an estimate of the magnetic field strength on the white dwarf surface of $B \sim 20\,\mathrm{MG}$ near the poles and $B \simeq 10\,\mathrm{MG}$ at the equator.

---

[1] the position angle with respect to the connecting line of both stars in the orbital plane, in a right-handed coordinate system

[2] the position angle measured from the z-axis

Date	Telescope	Filter	HJD start	HJD end	Exp. time (red/blue resp. I/B)
Aug 4,	CA 3.5m	spectr.	2451761.3710	2451761.4750	180/120 s
2000	AIP 70cm	I/B	2451761.3428	2451761.4856	21 s
Aug 5,	CA 3.5m	spectr.	2451762.5152	2451762.6141	180/120 s
2000	AIP 70cm	I/B	2451762.3645	2451762.6091	21 s
Aug 6,	CA 3.5m	spectr.	2451763.3597	2451763.5225	180/120 s
2000	AIP 70cm	I/B	2451763.3415	2451763.4967	30,40,60 s

Table 3.1: Log of the observations of AM Her used here

Emission line spectra were analysed by Young et al. (1981), who determined the primary mass $M_1 = 0.39\,\mathrm{M}_\odot$ and the magnetic field strength $B = 13\,\mathrm{MG}$. Optical spectroscopy with both, a high resolution in wavelength and time, have only be presented in the range around Na I $\lambda\lambda$8183/8194. Analysis of these lines resulted in values for fundamental system parameters. Southwell et al. (1995) determined a mass ratio of $q = 0.48 \pm 0.08$ and a mass of the secondary $M_2 = 0.20 - 0.26\,\mathrm{M}_\odot$ with their radial velocity fitting method. Using this method and the method of flux-deficit mapping, Davey and Smith (1996) calculated an intensity map of the Roche-lobe and gave a value for the inclination of $i \simeq 50°$.
WAT2003 determined the system parameters of AM Her with Roche-tomography: $\gamma = -17\,\mathrm{km/s}$, $i = 60$, $M_1 = 0.24 - 0.36\,\mathrm{M}_\odot$, $M_2 = 0.12 - 0.24\,\mathrm{M}_\odot$. Their intensity map shows a significant depletion of sodium absorption on the irradiated side of the secondary star.

This compilation is far from being complete. In most cases these are the latest publications concerning specific system parameters derived from different data sets, or are regarded significant for the interpretation of other data.
If the system parameters determined in the publications mentioned above are compared, it becomes clear that there is still a large scatter in their values. Especially the inclination i is practically not known, and the given values are in the range from 37° to 60°.
Although AM Her is the prototype-polar, no optical spectroscopy with a high resolution in wavelength and time and with full phase-coverage was published in the literature yet. With such kind of data, information about the main system parameters, the accretion geometry and the mechanisms of spectral line excitation may be obtained. The data presented here were observed to fill this gap.

3.2 The data

The spectra of AM Her analysed in this work were taken on August 4, 5 and 6, 2000 at the 3.5m-telescope at Calar Alto, Spain, with the two-channel spectrograph TWIN. This instrument provides high-resolution spectroscopy in two separate wavelength regions simultaneously.

During this observation run we used grating T01 (second order) in the blue arm, and grating T06 in the red one. The chosen wavelength ranges were 4200 Å to 5000 Å (blue) and 7660 Å to 8650 Å (red). With a 1.5” spectrograph slit we achieved a spectral resolution (measured at the night-sky lines) of 1.1 Å (~ 80 km/s) and 1.4 Å (~ 50 km/s), respectively.

The data reduction was straight forward, including flat-fielding with dome-flats, wavelength calibration with arc-lamp spectra, and flux calibration with standard star exposures. The time information stored in the data was transformed to the solar system’s barycentre.

The wavelength regions were chosen to cover the emission lines of Hβ, Hγ, and He II λ4686 in the blue arm, and to be centered on the sodium doublet at 8183/8194 Å. Other lines within these ranges proved to be interesting as well (O I λ7775, Ca II λ8498 and Ca II λ8542, K I λ7667 and K I λ7699).

Simultaneously to the spectroscopic observations, AM Her was observed with the 70cm-telescope at the AIP in Potsdam. The light curves obtained in I and B (Fig. 3.2) were used for the flux calibration of the spectra, accounting for slit-losses and changing transparency of the atmosphere. The correction factors were calculated as a ratio of continuum flux in the spectra and the flux in the overlapping broad band range. The smallest factor was set to 1, assuming that at this point the slit and atmospheric absorption losses were negligible. All the other factors were normalised to this value. Although variations not intrinsic to the system can thus be removed, an absolute flux calibration is not possible because of the not completely overlapping response curves of the broad-band filters and the spectrograph, the exclusion of spectral lines for the determination of the flux from the spectra, and slit-losses, even at the best weather conditions and with a relatively wide spectrograph slit of 1.5”. I thus mark the fluxes as ’arbitrary units’ instead of ’10^{-16} erg cm^{-2} s^{-1} Å^{-1}’.

The data of August 6 were already presented by Schwarz et al. (2002), most of those of the remaining nights already by Staude et al. (2004). Orbital phase is calculated according to the ephemeris by Schwarz et al. (2002, BJD(orb)= $2446603.40308(35) + E \times 0.128927103(6)$ d). This ephemeris was derived using the data for August 6, 2000 by measuring the time of blue-red zero crossing of the Na I absorption lines from the secondary star ($HJD = 2451763.452523$). With respect to the T_0 from Southwell et al. (1995) we derive a cycle-count of 40023.

The absorption lines show the behaviour typical for polars: A sinusoidal motion around the rest-wavelength and a weaker absorption around orbital phase 0.5 than around 0.0. The explanation is that the absorption lines arise

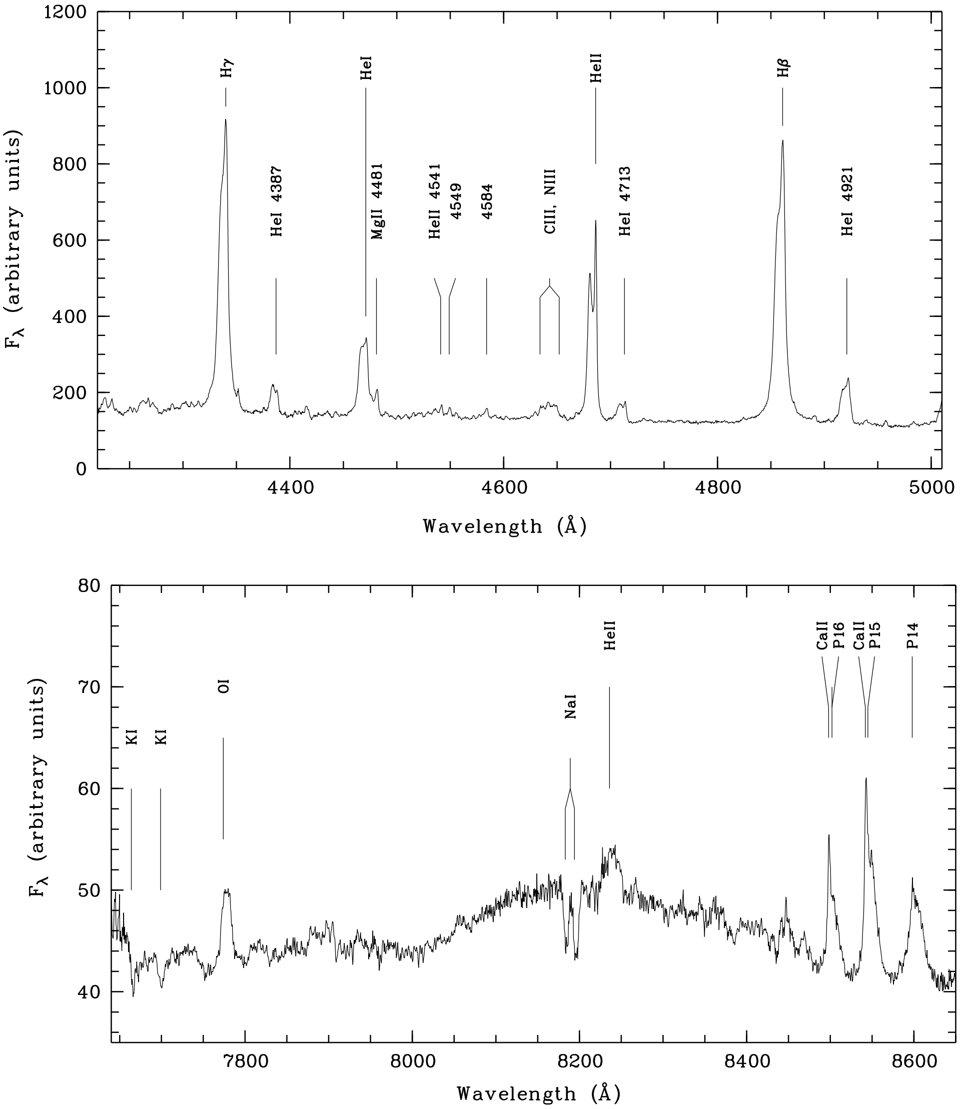

Figure 3.1: AM Her: averaged spectra from Aug. 6, 2000: *top*: blue arm, orbital phases (0.4,0.6), *bottom*: red arm, orbital phases (0.9,1.1) The phase ranges were selected to show the differences between best visibility of the undisturbed hemisphere of the secondary and best visibility of the irradiated side.

on the secondary star. On the part of the surface which is irradiated by high-energy X-ray and UV photons, the temperature stratification in the atmosphere is changed, so that the absorption features typical for a M-star become weaker.

Instead there are emission lines originating on the irradiated hemisphere. The most prominent lines are the Balmer lines of hydrogen and the lines of neutral and ionised helium. But other species are seen as well: Ca II (blended with the hydrogen Paschen lines), Mg II and the Bowen blend of C III/N III (Fig. 3.1). All the emission lines show a narrow component (NEL), which can be identified as originating on the irradiated hemisphere of the secondary by its low velocity amplitude and its phasing with respect to the absorption lines. While some lines show only the NEL (e.g. the Ca II lines), other lines (hydrogen, helium, Mg II) consist of multiple components. (The absence of these additional components in the case of Ca II is not caused by a low signal-to-noise ratio. If there were other components with similar intensity-ratios compared to the NEL like in the case of the other lines, they would be detected easily.)

3.2.1 Light-curves

Optical light-curves of polars are formed out of multiple components. These are originating from the constituents of such systems, as there are the white dwarf with its atmosphere, the accretion column emitting cyclotron radiation, the accretion stream or curtain, showing continuum and line emission, and the secondary star. The latter is showing an undisturbed late-type stellar atmosphere on the un-irradiated side and strong emission lines and reduced absorption features on the irradiated hemisphere. All these components have different shares on the flux in different pass-bands and vary with changing aspect angles. Polars are also intrinsically variable, which creates additional fluctuations to the orbital modulation.

To use all available information, the light-curves obtained in optical broad-band filters and from spectral lines are analysed additionally to the spectra.

The brightness values covered during the observations of AM Her in August 2000 ($14\overset{\mathrm{m}}{.}2$ to $13\overset{\mathrm{m}}{.}7$ in B and $13\overset{\mathrm{m}}{.}5$ to $12\overset{\mathrm{m}}{.}5$ in I) show that the system was in a high accretion state (low state $\Leftrightarrow B \sim 15.5$, de Martino et al. 2002, Götz 1993, high state $\Leftrightarrow B \sim 13.7$, Gänsicke et al. 2001).

The I-band light-curves look like the ones published earlier by Olson (1977). They have roughly a similar double-humped shape in all three nights. Especially the maximum at $\phi \sim 0.3$ has the same height (~ 1 mag). The second maximum varies in height between 0.5 and 1 mag.

The B-band light curves vary strongly from night to night and are different from the ones published by Olson (1977), Szkody and Brownlee (1977) and Gänsicke et al. (2001).

The secondary maximum (at phase 0.7) in our data shows strong brightness variations during the three nights of observation. It was faintest in the first one, during the second one its luminosity increased (the two brightness levels are best seen in the phase-folded data in I), and the two maxima showed nearly the same flux level in the third night.

This behaviour was apparent in both broad-band filters. It could be understood when taking into account a model presented by Wickramasinghe et al. (1991), in which nearly all contimuum-emission is produced by two cyclotron-emitting regions. Their continuum light-curves showed a pronounced double-hump shape.

The high variability in our data could thus be interpreted as the result of a change in the accretion geometry, which changed the amount of cyclotron

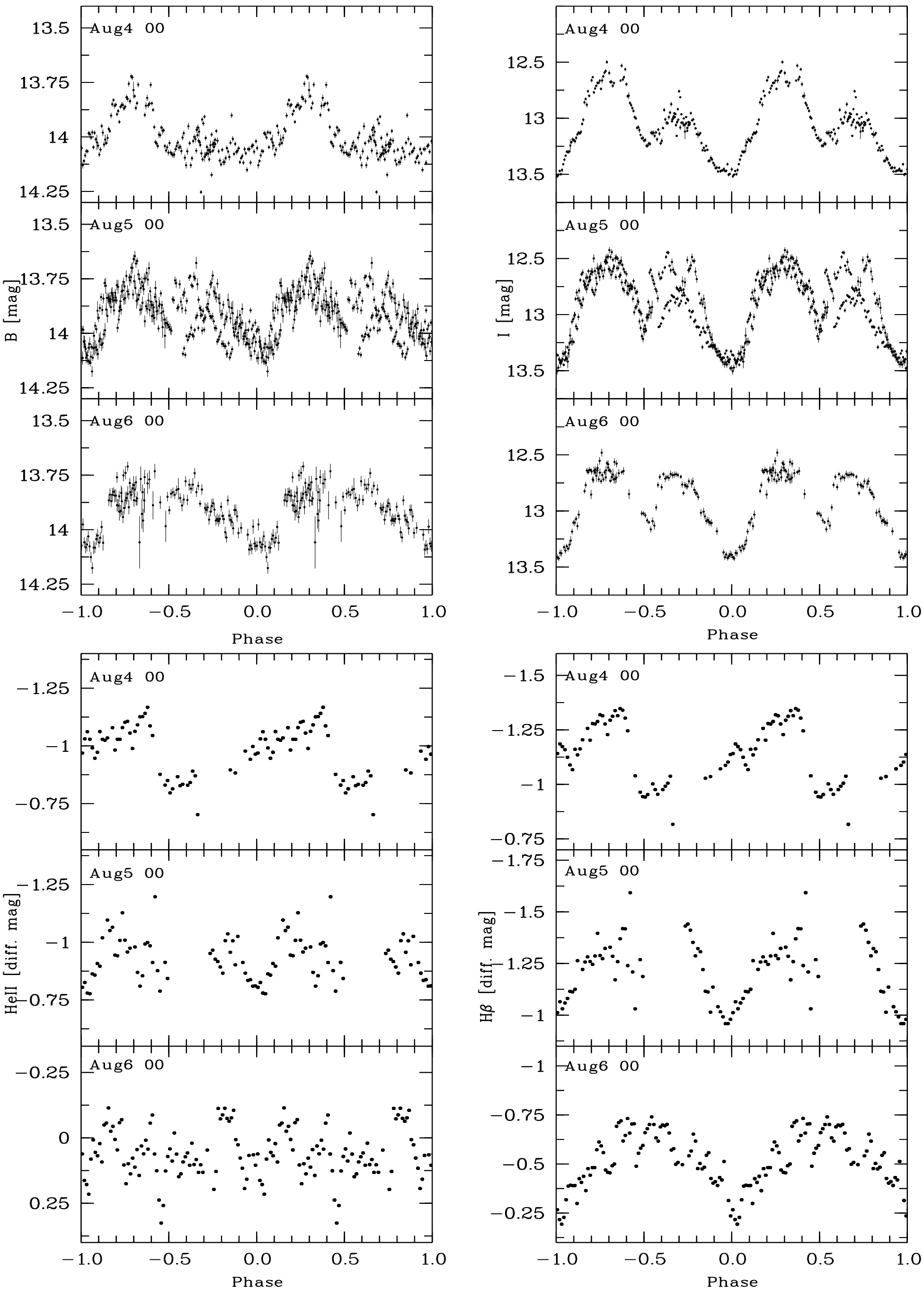

Figure 3.2: AM Her: Light curves, *top*: broad-band light curves in B and I, *bottom*: line light-curves He II $\lambda4686$ and Hβ

radiation arising in the region responsible for the secondary maximum.

To study the spectral line emission in comparison to the continuum radiation, line light-curves were produced by simply averaging the flux of the continuum-subtracted trailed spectra (as seen in Figs. 3.6 and 3.7). To get

comparable scales, the flux was transformed to an arbitrarily scaled magnitude according to $mag = -2.5 * \log_{10}(flux) + 5.2$.
The line light-curves of He II and Hβ show a complicated behaviour: On August 4, both curves have roughly the same shape, clearly different from both broad-band light-curves. The line-flux is constantly rising from phase 0.5 to phase 0.4, with a sharp drop between 0.4 and 0.5.
Both light-curves of the lines from August 5 look similar, and resemble – with respect to the low accuracy – the continuum light-curves in B.
On August 6, only the flux of the Hβ line follows the behaviour of the continuum, the He II line light-curve shows a more irregular shape with a deep eclipse-like feature near $\phi = 0.45$, which is also visible (but weaker) in the case of Hβ and the B-band.
The line light-curves from August 4 are obviously dominated by the additional stream feature, which is apparent in the spectrum and the Doppler-tomogram (Fig. 3.6). In the following nights, the line light-curves are more symmetric with respect to phase 0.5. An explanation could be that there is no visible asymmetry between the irradiated and unirradiated side of the accretion stream.

3.2.2 Absorption lines

The two sodium lines are by far the strongest absorption lines in the spectra, and thus they are used for further analysis of the system. The weaker lines of K I show the same variations with respect to orbital phase but have a much lower signal-to-noise ratio.
The properties of the absorption lines showed no significant night-to-night variations, so the data of all nights were merged after subtracting the continuum to enhance the signal-to-noise ratio.
Both sodium lines belong to the same excitation state and should, therefore, have the same line properties (profile, depth, ...). In the literature, spectra from polars can be found which show the sodium doublet with two identical lines, as well as cases with the lines having different depths, e.g. AM Her (Southwell et al., 1995), QQ Vul (Catalán et al., 1999), V1309 Ori (Staude et al., 2001). Also in the case of single M-stars both states can be found, and always (to my knowledge) the line at 8194 Å is deeper. As far as I know, nobody has investigated this. Probably there is a superposition with another spectral line under certain circumstances. In the case of the data used here the line-flux ratio is $\simeq 0.75$ at all phases.

Deconvolution of the Na I-doublet lines

For the use of Doppler-tomography it is necessary to disentangle the two sodium lines, because they are so close to each other that they would produce significant artifacts in the tomograms. The Roche-tomography code can deal

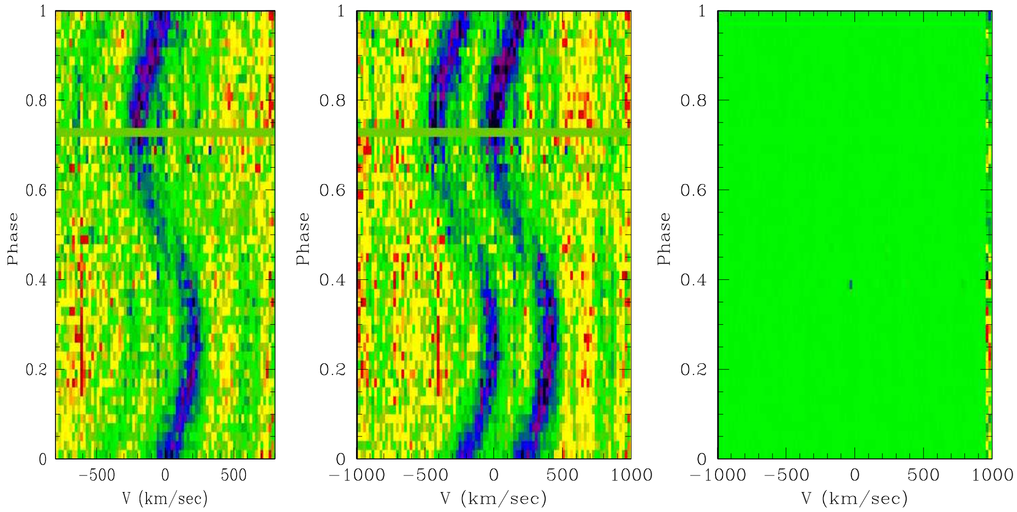

Figure 3.3: AM Her: Summation of the sodium lines from Fig. 3.4: *left*: the deconvolved line profile, *middle*: the fit, *right*: the residuals of the fit. For the fit and the residuals the same cut-levels were chosen. (colours: Fig. A.1)

with any intrinsic line profile, in particular it could deal with two close-by, similarly behaving, absorption lines. But since the whole profile has to be projected frequently during the fitting procedure, a profile as narrow as possible is favoured. Thus, considering the necessary computer time, a single line is advantageous.

If one assumes that line profile and distance are the same for both lines anytime, one can fit a line profile to both simultaneously. For this purpose I wrote a program using Evolution Strategy for the fitting of the data. The output (Fig. 3.3) is one line spectrum which gives the least χ^2 when projected with the given separation and depth ratio, taking into account some sort of smoothness when necessary, e.g. in the case of noisy data.

As becomes clear from the residuals (they are very close to the zero level), the data could be fitted very well. But in the deconvolved line there seem to be some artifacts at ±500 km/s from the line center. Probably this is a result of the not perfect removal of night-sky lines, as can be seen when comparing the original data with the deconvolved. Further it may arise from a violation of the assumption of equal line profiles – maybe due to superposition with other spectral lines.

Anyway, even if one uses the original data for Roche-tomography, and fits an intrinsic line profile consisting of two gaussians with the same FWHM and a line-flux ratio of 0.75, the problems would remain and would arise during the calculation of the Roche-map.

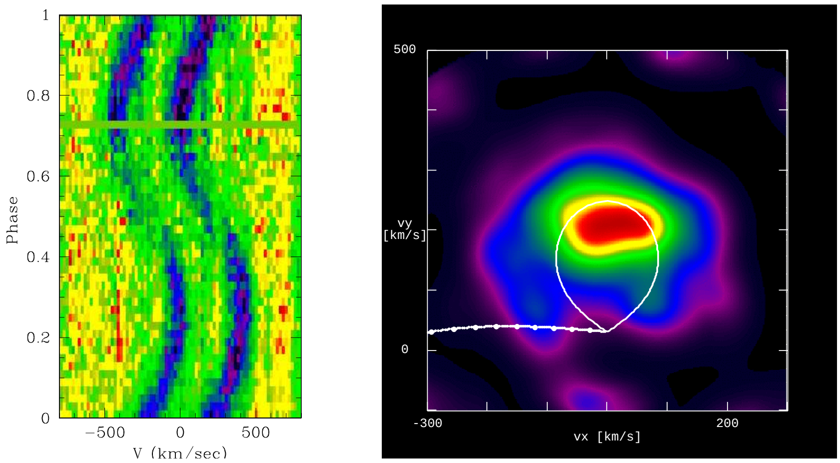

Figure 3.4: AM Her: The sodium lines at 8183 Å and 8195 Å, combined data of all three nights, and the resulting Doppler-map (with overplotted contour of the Roche-lobe for $Q = 1.4$, $M_1 = 0.3\,\mathrm{M}_\odot$, $i = 50°$, colours: Fig. A.1)

Analysis with Doppler-tomography

In Fig. 3.4, the phase-resolved line-profile of the two sodium lines and the resulting Doppler-tomogram are shown. The tomogram was calculated with the code by Spruit (1998). The overplotted outline of the secondary star was calculated for the values of the system parameters as determined with Roche-tomography from the Ca II λ8498 line (page 84). The observed sodium absorption is located mainly within the calculated Roche-lobe, but is shifted to too high v_y to be compatible with the idea of arising on the whole unirradiated hemisphere for this parameter combination. This is discussed further in section 3.2.5.

3.2.3 Emission lines

The lines with the best signal-to-noise ratio are those of the hydrogen Balmer series and the one from He II at 4686 Å. Other prominent emission lines are those of He I at 4921 and 4471 Å. In the case of the line at 4471 Å, the analysis is complicated because of the blending with the Mg II line at 4481 Å. The line of He I λ4921 (Fig. 3.9) has a much lower signal-to-noise ratio than the one of He II. The shape of line profiles and tomograms is similar, which is the reason I concentrate on the analysis of He II. From the Balmer-lines I only use Hβ, because Hγ looks very similar. Further interesting lines are those of neutral calcium, which show nearly no stream component but just a prominent NEL. Due to the stronger signal I will use the one at 8498 Å rather than the one at 8542 Å which looks similar.

The narrow emission line component

In all detected emission lines, a nearly sinusoidal component with a low velocity amplitude is seen, which can be identified with the narrow emission line component (NEL) arising on the irradiated surface of the secondary star.

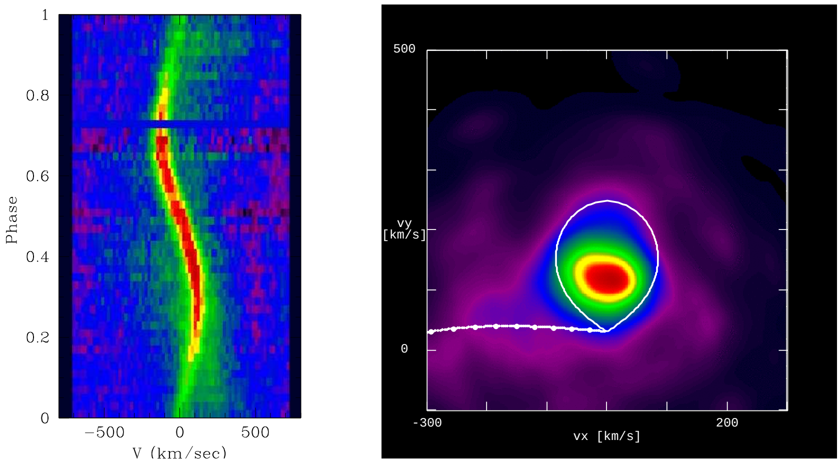

Figure 3.5: AM Her: The calcium line at 8498 Å: combined data of all three nights, and the resulting Doppler tomogram (with overplotted contour of the Roche-lobe for $Q = 1.4$, $M_1 = 0.3\,\mathrm{M}_\odot$, $i = 50°$, colours: Fig. A.1)

The calcium emission line at 8498 Å (Fig. 3.5) shows a strong NEL, but nearly no stream component. With this line the determination of the system parameters was attempted with Roche-tomography (see page 84). The overplotted contour of the secondary star in Fig. 3.5 was calculated from the best-fit values.

In Fig. 3.7, the Hβ emission line shows a bright NEL and a diffuse stream contribution without much substructure. In the resulting Doppler-tomogram the NEL is located at the expected position of the irradiated hemisphere of the secondary star.

The trailed spectra and the tomograms of He II (Fig. 3.6) look different. The NEL is not centered on the secondary's surface, which could denote that there is shielding of the incident radiation by the accretion stream.

The position of the NEL in the tomograms of He I cannot be identified as clear as in the cases of Hβ and He II. On Aug. 4 the NEL seems to be shifted away from $v_x = 0$ to higher v_x, a similar position as in the case of He II. On Aug. 5 the NEL cannot be isolated from the stream emission, and on Aug. 6 the NEL is positioned at $v_x \sim 0$.

The stream component

All emission lines show a stream component additionally to the NEL. The low signal-to-noise ratio prevents a detailed analysis in case of the majority of lines,

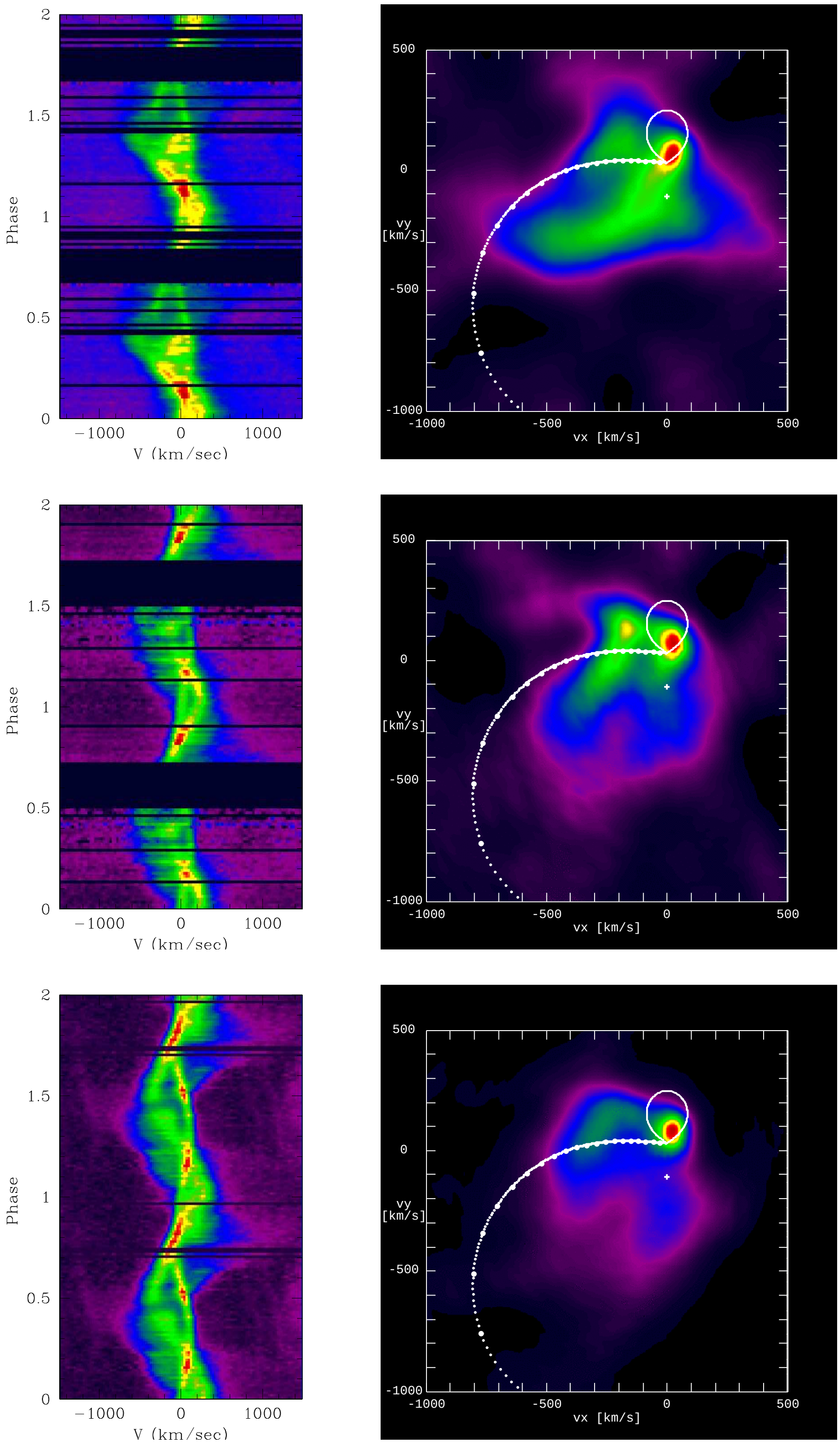

Figure 3.6: AM Her: He II, spectra and Doppler-tomograms for the 4., 5., and 6. August 2000 (from top to bottom) (with overplotted contour of the Roche-lobe and ballistic stream for $Q = 1.4$, $M_1 = 0.3\,\mathrm{M}_\odot$, $i = 50°$, colours: Fig. A.1)

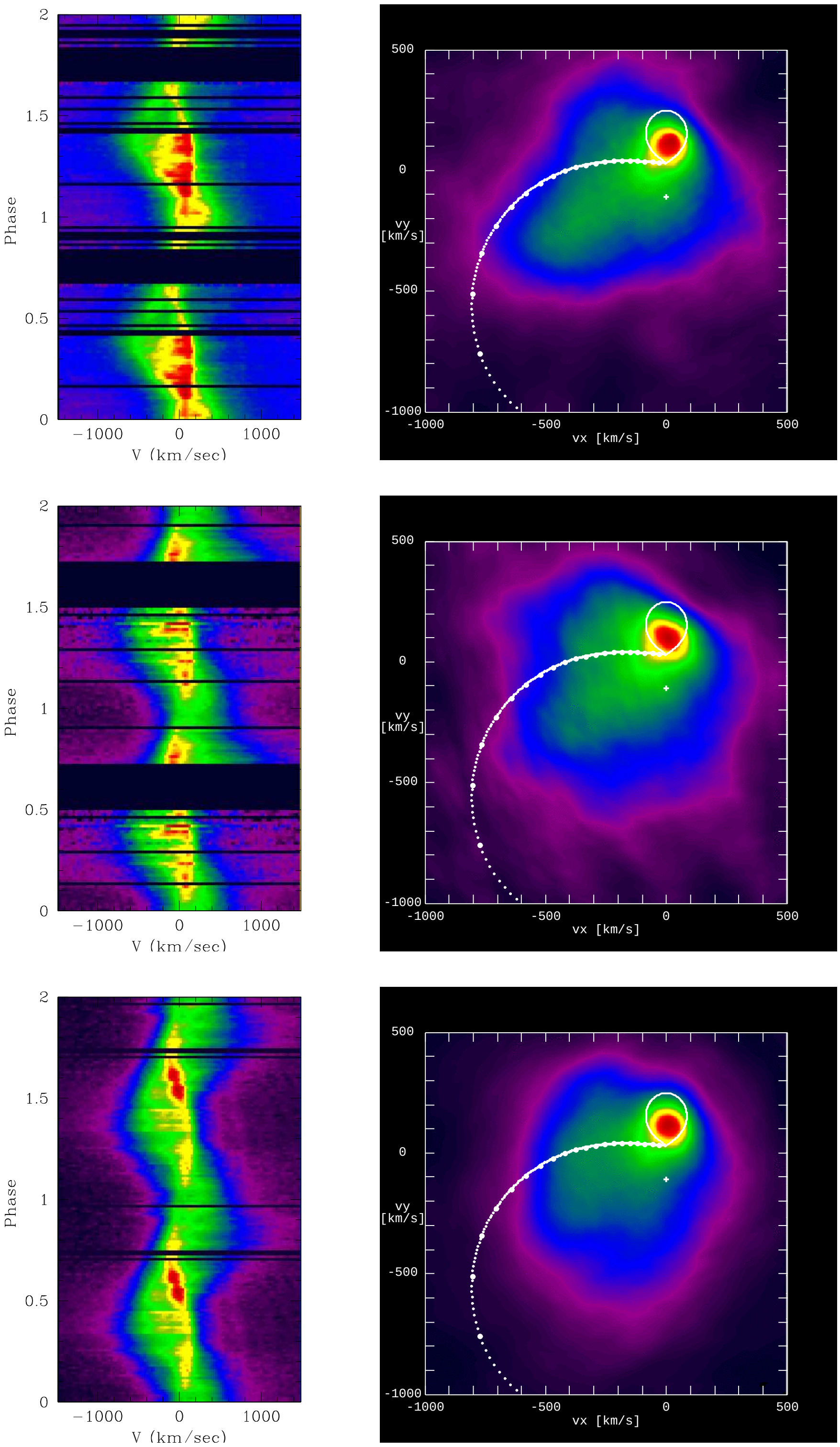

Figure 3.7: AM Her: Hβ, spectra and Doppler-tomograms for the 4., 5., and 6. August 2000 (from top to bottom) (with overplotted contour of the Roche-lobe and ballistic stream for $Q = 1.4$, $M_1 = 0.3\,\mathrm{M}_\odot$, $i = 50°$, colours: Fig. A.1

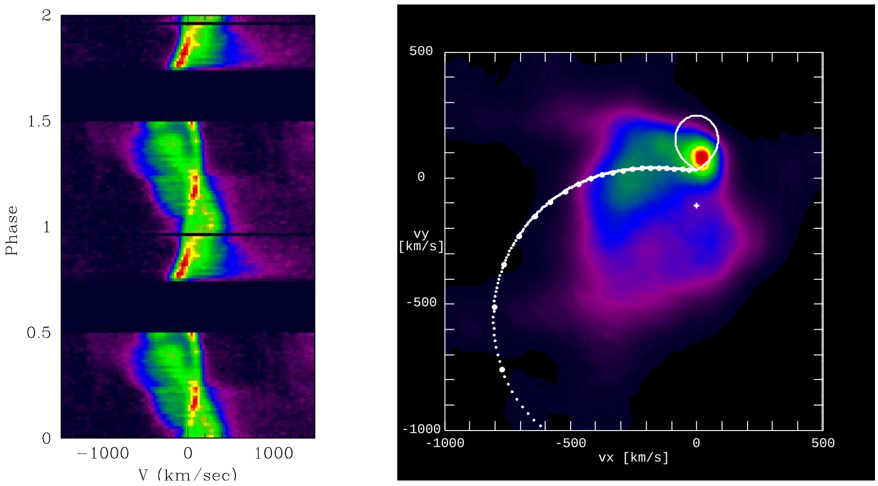

Figure 3.8: Trailed spectrum and Doppler tomogram of AM Her He II λ4686, August 6, 2000, with the same big gap in phase as on August 5 (with overplotted contour of the Roche-lobe and ballistic stream for $Q = 1.4$, $M_1 = 0.3\,\mathrm{M}_\odot$, $i = 50°$, colours: Fig. A.1)

so I concentrate on the most prominent ones.

In the case of **He II** (Fig. 3.6), the line profile is different during each observation. The observed structure apart from the NEL in the tomogram resembles a stream, but cannot be identified with a ballistic stream starting at L_1. In the first night, emission stretching from the position of the NEL in the tomogram directly to the lower left quadrant is the dominating part besides the NEL. This feature has completely vanished one night later and is also missing in the third night.

The remaining emission (besides NEL and the additional structure on Aug. 4) in all three nights transforms to a stream-like structure starting (?) with a clearly higher v_y than the predicted ballistic stream. At low v_x this structure bends towards the lower left quadrant but is cut-off quite soon. Compared with the brightness of the NEL, this feature is similarly bright during the first and third night, while it is clearly brighter in the second.

The differences between the data from the second and third night are not this obvious in the spectra. But the tomograms from Aug. 5 and 6 show a clearly changed stream-like feature. To be sure that this change is not caused by the big data gap in the Aug. 5 spectra, the same big gap was introduced into the data from the third night. The resulting tomogram (3.8) didn't change much compared to the complete data set.

The emission above the location of the ballistic stream in the tomograms (at higher v_y) cannot be explained with the standard model of mass transfer in CVs, because these velocities cannot be reproduced by matter flowing off via the L_1 with velocities of the order of the sound speed.

One explanation could be that the emission apart from the NEL and the extra emission on Aug. 4 was originating in a coronal loop. The problem

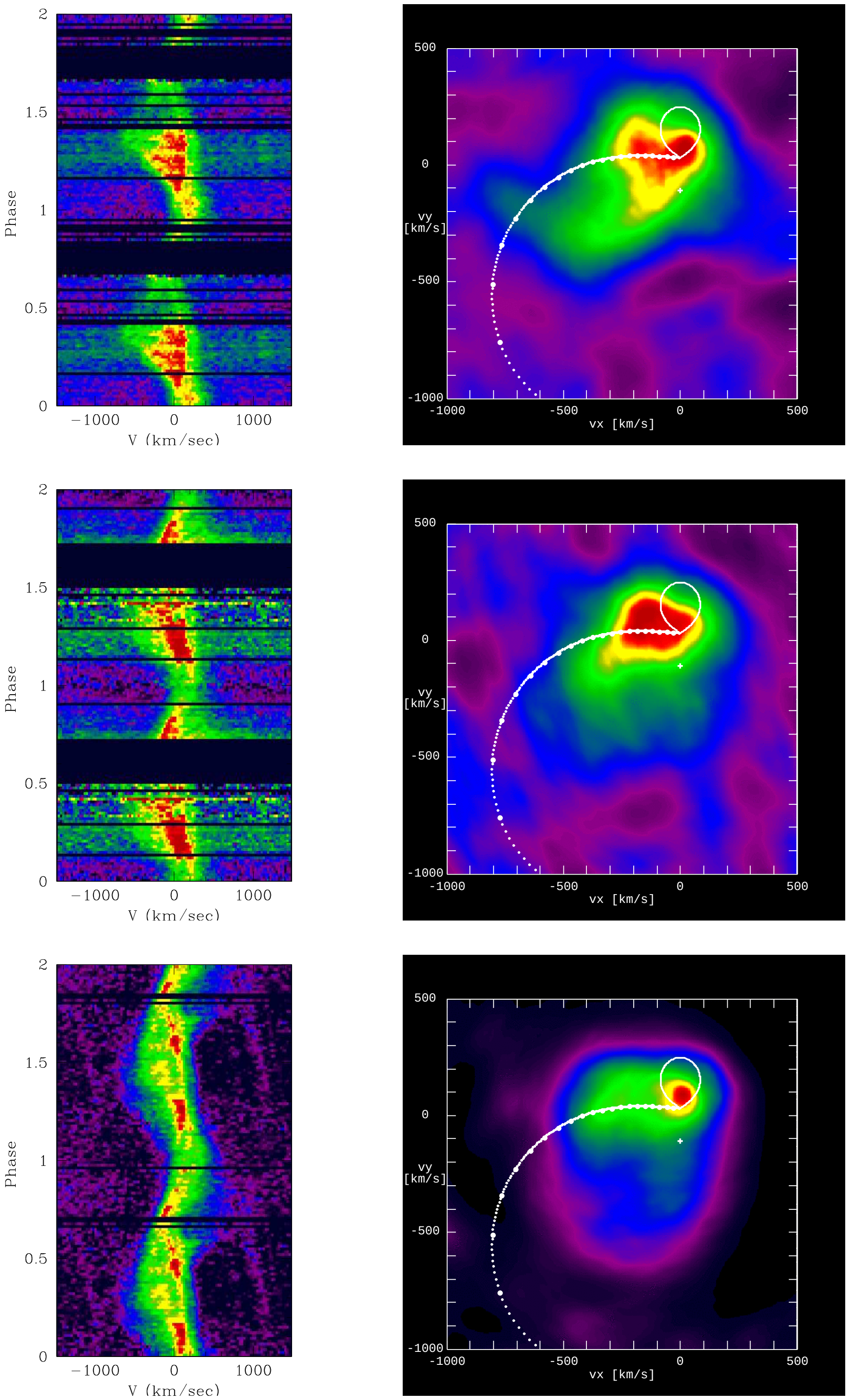

Figure 3.9: AM Her: He I λ4921, spectra and Doppler-tomograms obtained on August 4, 5, and 6, 2000 (from top to bottom) (with overplotted contour of the Roche-lobe and ballistic stream for $Q = 1.4$, $M_1 = 0.3\,\mathrm{M}_\odot$, $i = 50°$, colours: Fig. A.1)

would then be, how the ionisation is achieved, when there is no accretion onto the white dwarf and thus no ionising radiation from the hot spot. It may be possible that the magnetic field trapping the matter, or the hot matter of the corona are providing the necessary energy.

Only on Aug. 4 there is an additional stream-like feature which could transport the matter. But the over-all system brightness and the apparent brightness of the NEL component is nearly the same in all three nights, so accretion should have happened also in the last two nights, otherwise the amount of irradiation should have been diminished. If one assumes this feature in the tomogram to be the signature of a structure transporting matter, to reach the observed velocities the matter either has to start with a velocity which can clearly not be explained by Roche-lobe overflow, or the observed matter is somewhere near the white dwarf, where the magnetic field has changed the direction and velocity of its motion. The latter scenario is unlikely, because due to the rapid increase of the velocity near the white dwarf the emission is expected to be spread over a wide range of velocities.

This expectation is supported by the observations of the only two polars, where the standard model was able to reproduce the observed tomograms – HU Aqr and UZ For (Schwope et al., 1999). In their tomograms the accretion stream is not visible any more shortly after coupling to the magnetic field lines. Since both systems are eclipsing, i.e. are having a high inclination, v_z-effects are negligible and cannot contribute much to a smearing in the v_x-v_y-plane.

Generally, the effect of 'invisible' magnetically guided streams could also arise due to the low signal-to-noise ratio in the strongly Doppler-shifted parts of the spectral lines and due to the lower sampling of the tomogram in the outer regions than near the center of mass.

I favour a scenario, in which the matter starts somewhere else than at the L_1 on the secondary's surface. This could happen when matter flows along strong local magnetic field lines. To achieve accretion onto the white dwarf (which is necessary to get ionising radiation; also, judging the system's brightness, it was in a high accretion state during all nights) the matter has to be guided somehow into the primary's Roche-lobe. The superposition of the fields from both, the white dwarf and the secondary, could create field lines capable of doing this.

As a simple test I assumed the accretion flow to start somewhere else than at the L_1 at the irradiated hemisphere with $\sim 600\,\mathrm{km/s}$, and than directly coupling to a dipole fieldline of the white dwarf. I tried to reproduce the observed data by changing the orientation of the dipole and the starting point at the surface of the secondary star.

I found a dipole orientation, which was able to reproduce the structures seen on Aug. 5 and 6 by just changing the starting point on the donor star. The two configurations and the resulting tomograms are shown in Fig. 3.10. The emission was assumed to be optically thick. In the model for Aug. 5, the

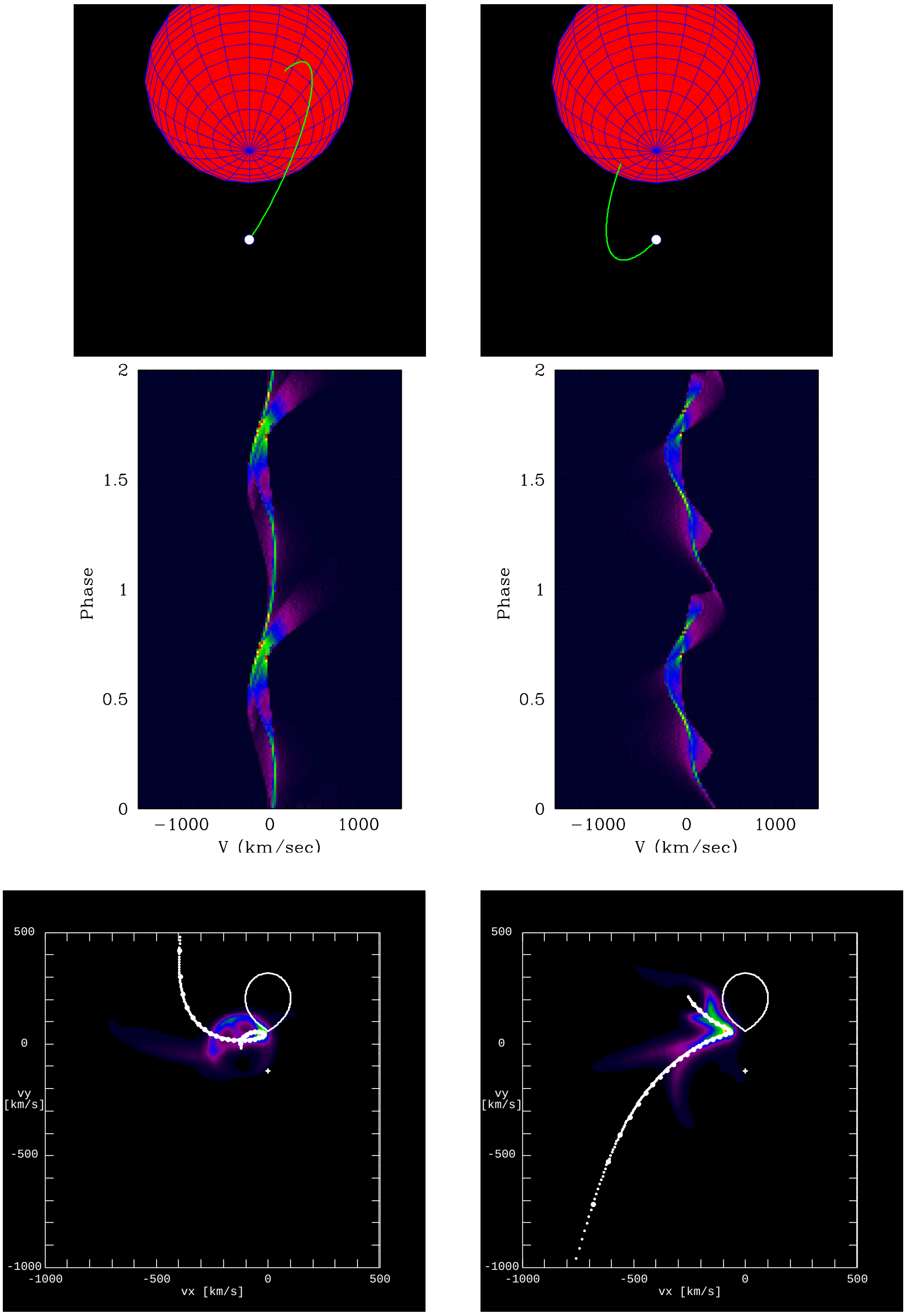

Figure 3.10: AM Her: Simple model, which creates similar features in the Doppler-map like the observed He II line on Aug. 6. (left) and Aug. 5 (right). Assumed was a centered dipole with colatidude $\beta = 32.5°$, azimuth $\psi = -104°$, $Q = 1.667$, $M_1 = 0.433\,\mathrm{M}_\odot$, $i = 60°$, optically thick emission, ratio irradiated/unirradiated side of the stream = 3 (left) and = 1 (right).

stream is thought to be irradiated by the hot spot, resulting in a flux ratio irradiated/unirradiated of 3, while the model for the Aug. 6 has a ratio of 1. The synthetic spectra were calculated for an inclination of 60°, thus being strongly influenced by v_z-effects.

The assumed starting velocities in this toy model are high. This is probably caused by our simple treatment of the interaction between the matter and the magnetic field. A model solving the magneto-hydrodynamical equations for the superposed magnetic fields would certainly lead to much different initial values for the velocity.

In the case of **Hβ**, the remaining emission apart from the NEL looks like a smeared-out version of the one seen at He II.

The line **He I λ4921** shows the same structures as the one of ionised helium, but in the first two nights the stream emission is clearly dominating the one from the NEL (contrary to what is seen at He II and Hβ).
These changed ratios may give hints on the ionisation and excitation conditions in the stream and on the irradiated hemisphere of the seconderay star. With a radiative transfer code it could be possible to determine the physical properties of the emitting matter and the incident radiation.

3.2.4 Roche-tomography

Na I

For trying to determine the system parameters of AM Her, an entropy-grid was calculated first for the sodium absorption lines. For the fit, the intrinsic line-profile was set to a Gaussian with FWHM= 60 km/s. This value is compatible with the line widths of the sodium-doublet in the slowly rotating single M-star LHS2065 (Tinney and Reid, 1998).
χ^2_{aim} was set such, that for a significant number of grid-points the final χ^2 is in the 10% interval of χ^2_{aim}, and the resulting entropy map is smooth.
The slices of the entropy grid containing the highest value are shown in Fig. 3.11. The best-fit value is at $Q = 1.0$, $i = 40°$, and $M_1 = 0.9\,M_\odot$, at the edge of the parameter range. Thus it is not possible to find a unique set of best-fit parameters from the sodium lines, because values of $Q = M_1/M_2$ lower than unity are not in concordance with the current understanding of CVs.

What could be reasons for the failure of the parameter determination?
When looking at the observed line, the best fit and its residuals (Fig. 3.12), one can see that there is line intensity in the fit at low velocities around phases 0.25 and 0.75. This intensity is required to fit the remains of the night-sky lines, which could not be subtracted better from the observed data.
These low velocities require the map to reach down to nearly zero velocity at those phases. A mass ratio near unity provides both, these low velocities and the high velocities seen in the sodium lines. In the best-fit map (Fig. 3.13) there is some intensity near L_1, while the dominating part is on the unirradiated

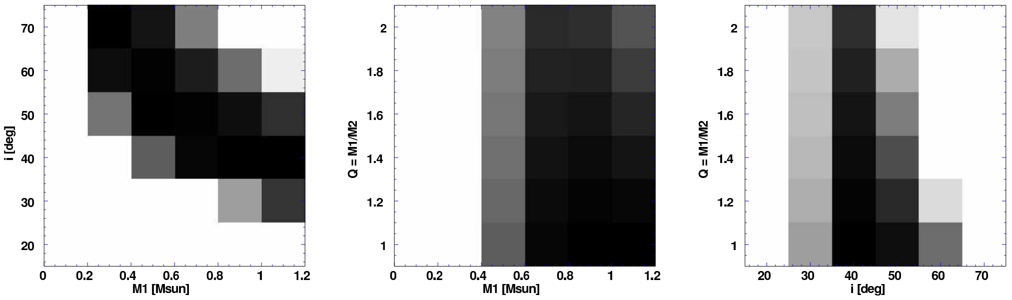

Figure 3.11: The entropy maps for the fits onto the Na I line (Fig. 3.4), with respect to the system parameters Q, i, and M_1 are shown as slices of the data cube, which are containing the best-fit value for each map: $Q = const.$-plane (*left*), the $i = const.$-plane (*middle*), and the $M_1 = const.$-plane (*right*). Black denotes higher entropy.

hemisphere.

Another reason could simply be the too low signal-to-noise ratio of the data. It is difficult to estimate the errors of the data, because the 'noise' is not just photon noise, but the data are contaminated by remains of the night-sky lines, artifacts introduced by the line-separation, and other weak lines apparent in the data. Thus it is not possible to test the results with artificial spectra with a comparable S/N-ratio.

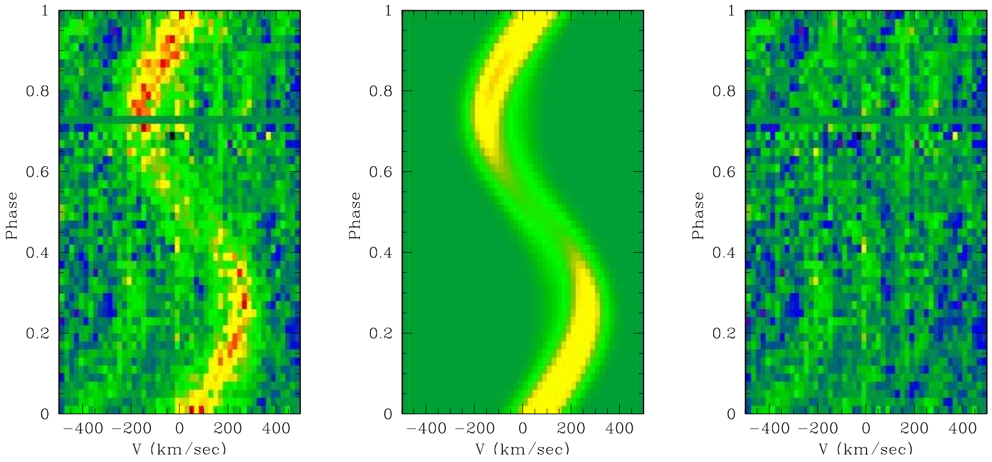

Figure 3.12: The spectrum for the best fit to the Na I line (Fig. 3.4): *left*: observed spectrum, *middle*: fitted spectrum, *right*: residuals (all with the same cut levels).

Ca II

The line of Ca II was fitted with a Gaussian of 20 km/s FWHM as intrinsic line-profile.

The resulting entropy-grid shows a clear maximum at $Q = 1.4$, $i = 50°$, and

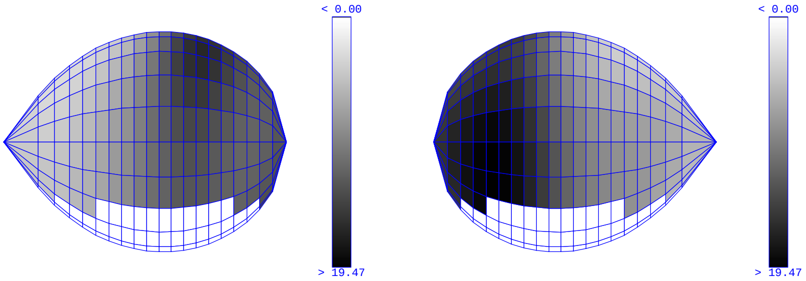

Figure 3.13: The intensity map leading to the fit shown in Fig. 3.12 displayed for $i = 90°$ at phases 0.25 and 0.75.

$M_1 = 0.3\,M_\odot$ (Fig. 3.14). The reliability of the determination I estimate as one grid element size in each coordinate – 0.2 in Q, 10° in i, and $0.1\,M_\odot$ in M_1. In the residuals of the best fit with the observed spectra (Fig. 3.15), it is seen that AStRoTom is tempted to fit the weak stream-component additionally to the NEL. The result is thus a compromise between left-over emission where the stream crosses the NEL, and too much flux removed at the other phases. The chosen values of α and χ^2_{aim} lead to a relatively smooth map which is not fitting best in χ^2. But these values were necessary to get a comparatively smooth entropy grid.

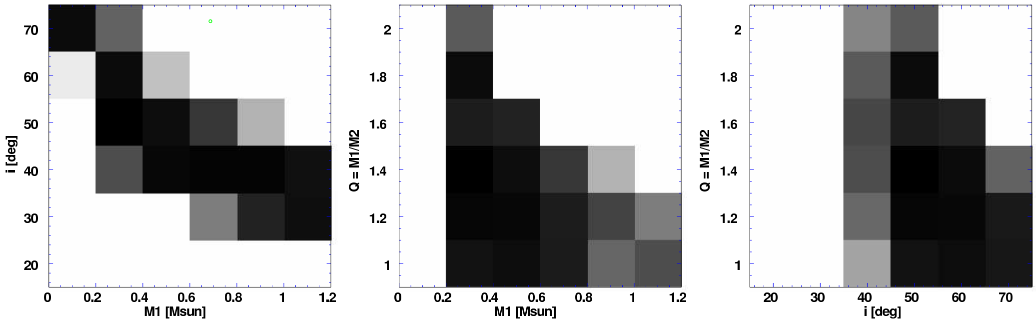

Figure 3.14: The entropy maps for the fits onto the Ca II line (Fig. 3.5), with respect to the system parameters Q, i, and M_1 are shown as slices of the data cube, which are containing the best-fit value for each map: $Q = const.$-plane (*left*), the $i = const.$-plane (*middle*), and the $M_1 = const.$-plane (*right*). Black denotes higher entropy.

For comparing these values for the system parameters with the observed data, the calculated Roche-lobe outline of the secondary star is overplotted onto the Doppler-tomograms in Figs. 3.5 and 3.4.
The emission peak in the case of Ca II is located near the center of the secondary star, while the peak in the Na I tomogram is found at the far end of the Roche-lobe.

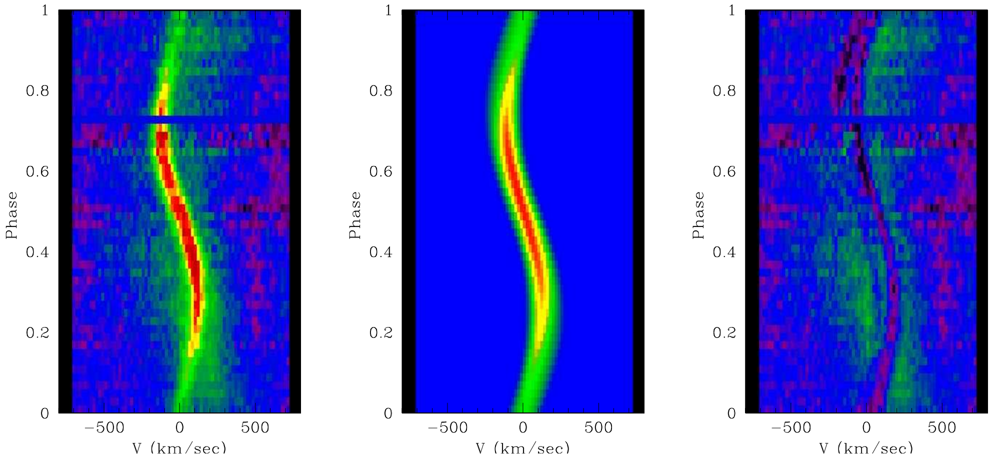

Figure 3.15: The spectrum for the best fit to the Ca II line (Fig. 3.5): *left*: observed spectrum, *middle*: fitted spectrum, *right*: residuals (all with the same cut levels).

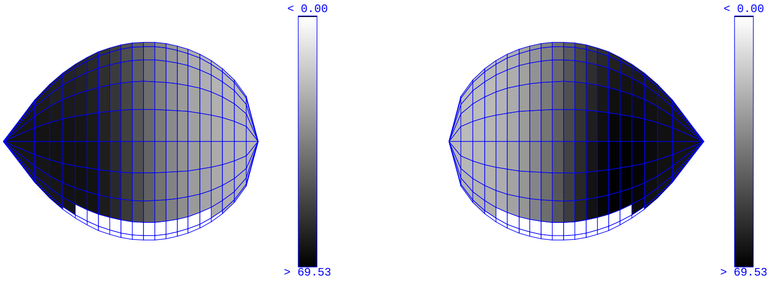

Figure 3.16: The intensity map leading to the fit shown in Fig. 3.15 shown for $i = 90°$ at phases 0.25 and 0.75.

The determined system parameters I consider as not convincing, because the sodium line is expected to originate on the Roche-lobe, thus the intensity clearly outside the calculated contour is difficult to explain with these system parameters. I would also expect the calcium emission to be more localised near the L_1, because there the irradiation is strongest and hitting under the lowest angle with respect to the normal of the surface.

3.2.5 Discussion

System parameters The determination of the system parameters with Roche-tomography did not lead to a consistent result.
Compared to previously published values for Q, i, and M_1 (e.g. WAT2003), the numbers determined with Roche-tomography from Ca II are still within a reasonable range.

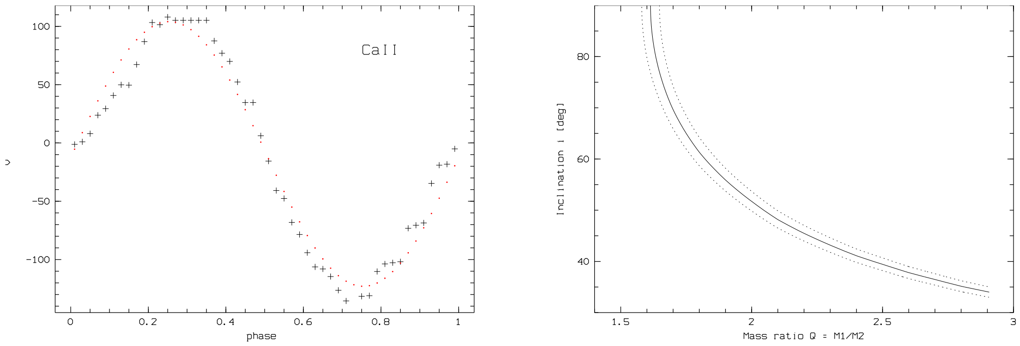

Figure 3.17: AM Her: *left*: Radial velocity measurements (black crosses, in km/s) of the calcium line and the fitted sine curve (red squares). *right*: The possible combinations of Q and i values for the measured radial velocity amplitude $K'_{2,CaII} = 114\,\mathrm{km/s}$ (straight line; the dashed lines mark the uncertainties in the velocity determination of 3 km/s).

From fits to the radial-velocity curves of the NEL, it is also possible to determine the system parameters of polars. For this purpose, Gaussians are fitted to the line profile at each phase in the trailed spectra, and the centers of those are fitted with a sine-curve, assuming a circular orbit: $v(t) = \gamma + K' \sin(\omega(t - t_0))$. This was performed for the calcium line (Fig. 3.17) and lead to values for the velocity of the center of light $K'_{2,CaII} = 114(3)\,\mathrm{km/s}$, and systemic velocity $\gamma = -9(2)\,\mathrm{km/s}$.

Fitting the observed velocity values with an elliptical variation containing two more free parameters, a better value of χ^2 was achieved, but the values for K' and γ remained unchanged.

The observed radial velocity amplitude is now used to determine the possible combinations of Q and i, as described in Schwarz et al. (1998): From synthetic spectra for the NEL calculated with the emission according to the model described by Beuermann and Thomas (1990), the conversion factors from the observed radial velocity K'_2, representing the motion of the center of light of the secondary star for this spectral line, to the radial velocity of the center of mass, K_2, are calculated for a number of combinations of Q and i. Assuming a ZAMS mass-radius relation according to Patterson (1984), the combinations of Q and i resulting in the observed radial velocity of CaII, were calculated (Fig. 3.17).

The system parameters determined with AStRoTom from the calcium line are not consistent with the model used for the calculation of Fig. 3.17, contrary to the values given by WAT2003.

In the case of the sodium lines, no entropy maximum was found within the parameter range for the mass ratio Q between $Q = 1 \ldots 2$. Since values of Q smaller than 1 are not possible with the Roche-lobe-overflow assumption, it is not justified to extend the range in this direction.

With the Ca II line, a clear maximum was detected at $Q = M_1/M_2 = 1.4 \pm 0.2$, $i = 50 \pm 10°$, and $M_1 = 0.3 \pm 0.1\,M_\odot$. These values do not fit well with the

Doppler-tomogram of the sodium lines, because the Roche-lobe is shifted to low orbital velocities to be able to distribute the calcium emission onto an area as big as possible.
If I would have been able to determine parameters with Roche-tomography of the sodium lines, the values obtained there could be used to restrict the parameter ranges to values resulting in higher orbital velocities. Only in a small range the possible parameter combinations obtained from the two lines would overlap. This could have lead to a consistent parameter determination.
With a similar approach as described above for the NEL, one could obtain information on the system parameters from the measured radial velocity of the sodium lines (Fig. 3.18) when assuming a certain intensity distribution on the surface.

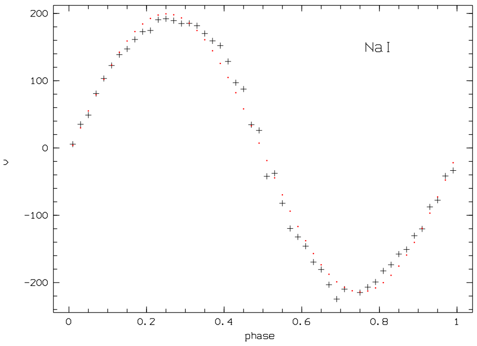

Figure 3.18: AM Her: Radial velocity measurements (black crosses, in km/s) of the sodium doublet and the fit (red squares). The line profile in the trailed spectra was fitted with two Gaussians with fixed distance and intensity ratio. Onto the position of the maxima, a sine-curve was fitted. The fit parameters are $K''_{2,NaI} = 207(3)\,\mathrm{km/s}$ and $\gamma = -7(2)\,\mathrm{km/s}$.

Stream component Our emission line spectra and the resulting Doppler-tomograms suggest modifications to the Roche-lobe overflow model, because emission is seen in the Doppler-maps at positions, which can clearly not be reproduced by the standard accretion model, consisting of a ballistic and a magnetically guided stream.
Whether all or part of the structures seen in the tomograms are caused by v_z-effects cannot be decided yet. To exclude this possibility it would be necessary to test all possible magnetic field configurations and different irradiation and emission laws for the accretion stream for the creation of artificial trailed spectra, which are to be compared to the observed ones.
However, to calculate trajectories following field lines in the superposition of the magnetic fields of the white dwarf and the secondary star, it would be necessary to solve the magneto-hydrodynamic equations in three dimensions.

The large differences between the emission lines observed on Aug. 4 and Aug. 5/6 may either be caused by a changed configuration of the stars' magnetic field, or by a changed accretion rate, which could force the matter to follow another trajectory. The different brightness levels of the secondary maximum (near phase 0.7) in the broad-band filters during the three nights are indicating a change in the mass flow to one of the accreting spots, if one assumes the majority of the continuum flux to be of cyclotron origin.

As explanation I favour a changed magnetic field structure on the secondary star, which could enable mass transfer from different locations on the secondary's surface. In the Doppler-tomograms a ballistic stream-component is not detected. This could mean that either it is not there at all, or it is only weakly emitting. For the latter, two explanations are possible: 1. the matter density is low, or 2. the atoms/ions are only weakly excited due to a lack of irradiation. Against the latter scenario speak the strong NEL components in both the atomic and ionic lines.

Chapter 4

QQ Vulpeculae

4.1 The system

QQ Vul was discovered as an X-ray source with the HEAO-1 low-energy detectors in the energy band 0.15 – 0.5 keV and was catalogued by Nugent et al. (1983). After the detection, spectroscopic, photometric and polarimetric observations were performed by Nousek et al. (1984), who classified the object as a polar with an orbital period of 222.5 min. The observed B-band luminosities are in the range from $B \sim 14\overset{\mathrm{m}}{.}4$ to $15\overset{\mathrm{m}}{.}5$.
The object was studied intensively over the years, including pointed X-ray observations, polarimetry, optical spectroscopy and photometry.
The spectroscopic observations lead to the detection of the secondary star and its absorption lines. This made first estimates of the system geometry via the rotational velocities possible (McCarthy et al., 1986, Mukai and Charles, 1987). The time of inferior conjunction of the secondary star could also be determined.
X-ray and polarimetric observations were used to get hints on the accretion geometry. Osborne et al. (1987) and Beardmore et al. (1995), using X-ray data, proposed a scenario, in which the accretion switches between a one-pole and a two-pole accretion mode. Cropper (1998) analysed polarimetric data and proposed that the cyclotron radiation is originating from an extended accretion arc on the white dwarf surface. He also proposed, that the spin of the white dwarf is not perfectly synchronised with the orbital rotation. The magnetic field strength is supposed to be around 30 MG.

A combined analysis of spectroscopic data with both, a high resolution in wavelength and time, and polarimetric data was presented by Catalán et al. (1999) (referred to as CAT1999) and Schwope et al. (2000) (in the following SCHW2000).
From the sodium lines alone the system parameters were determined as $i = 65 \pm 7°$, $q = M_2/M_1 = 0.54 \pm 0.08$ ($\Leftrightarrow Q = M_1/M_2 = 1.85$), $M_1 = 0.54^{+0.21}_{-0.16}\,\mathrm{M}_\odot$, and $M_2 = 0.30 \pm 0.10\,\mathrm{M}_\odot$, while the measured values of the system velocity γ were compatible with 0. The application of a combined flux-deficit and a radial-velociy fit to the sodium line and the Ca II/Paschen blend at 8542 Å gave

intensity maps of the lines at the Roche-lobe surface. The ones for sodium showed a depletion of line strength on the irradiated hemisphere and a shielding of the leading part of it, probably by the accretion stream. The amount of shielding varied between 1991 and 1993. The emission-line map showed a consistent picture: The emission was limited to the irradiated hemisphere and was more extended on the trailing half (CAT1999).

In SCHW2000 these results were combined with the analaysis of the emission lines in the range from 4200 Å to 5000 Å and of polarimetric data. From the analysis of the sodium absorption lines and the He II NEL they determined a spectroscopic ephemeris: $T_0(HJD) = 2448446.47105(48) + E \times 0.15452011(11)$. The system parameters determined by Doppler-tomography are $Q = 1.5 - 2.2$ for $i = 50° - 71°$. As origin of the NEL the irradiated photosphere of the secondary was determined, except in the case of the He II emission. There the centroid of the emission is located closer to the L_1-point, which can be explained by emission in an extended quasi-chromosphere.

Analysis of polarimetric data lead to a best fit for $Q = 1.75$ and $i = 60°$ and a magnetic dipole orientation in the white dwarf with colatitude $\delta_\mu = 23°$ and azimuth $\chi_\mu = -50°$, with the azimuth counting from the connecting line of both stars with negative values in the direction of the motion of the secondary. The azimuth of the region, where the accretion stream couples onto the magnetic field was determined as $\chi_\theta = -20°$.

The shape of the He II line in the trailed spectra looked different during each of the periods presented (1986, 1991, 1993). In the Doppler-tomograms the length of the (assumed) ballistic stream varied and it was not detected in 1986. At this time most of the emission seems to have been originating in the magnetically guided stream.

WAT2003 re-analysed the sodium line data presented by CAT1999 and SCHW2000, making use of their Roche-tomography code. They found the best fit at $i = 72°$, $M_1 = 0.66\,\mathrm{M}_\odot$ and $M_2 = 0.42\,\mathrm{M}_\odot$, thus finding $q = 0.63$. The ranges of possible values they give as $M_1 = 0.58 - 0.66\,\mathrm{M}_\odot$ and $M_2 = 0.34 - 0.42\,\mathrm{M}_\odot$, assuming $q = 0.63$.

The Roche-map, calculated with the best-fit values, shows a depletion of sodium absorption on the irradiated hemisphere and a possible shielding of the incident radiation on the leading hemisphere.

The optical light-curves of QQ Vul show a double-hump structure on the orbital period as well as variability on much shorter time-scales. The double-hump is explained by a combination of self-eclipse of the accretion-column by the white dwarf and cyclotron beaming.

Kafka and Honeycutt (2003) give an overview of the observed shapes of optical light-curves and of the reasons to prefer a certain accretion scenario or the other. Based on photometry spanning 10 years, they also see no hints for an asynchronism. Their long-term light-curves show the system to be variable between $V \sim 14\overset{\mathrm{m}}{.}2$ and $16\overset{\mathrm{m}}{.}2$.

The previously described observations indicate that QQ Vul is a highly variable system. Especially the information on the accretion geometry does

Date	Telescope	Filter	UT start	UT end	Exp. time (red/blue resp. I/B)
Aug 4, 2000	CA 3.5m	spectr.	2451761.3710	2451761.6585	180 s / 120,180 s
	AIP 70cm	I/B	2451761.5045	2451761.6008	50 s
Aug 7, 2000	CA 3.5m	spectr.	2451764.3620	2451764.5334	180,120 s / 300 s
	AIP 70cm	I/B	2451764.3364	2451764.5176	40,120 s / 50,120 s

Table 4.1: Log of the observations of QQ Vul used here

not give a consistent picture. Therefore another observation with time-resolved high-resolution spectroscopy was performed.

4.2 The data

QQ Vul was observed on August 4 and 7, 2000, using the TWIN at the Calar Alto 3.5m-telescope. In the blue channel, gratings T01 (Aug. 4, second order) and T05 (Aug. 7) were used, while the red spectra were taken with grating T06. With a 1.5" spectrograph slit, the resulting spectral resolution (measured at the night-sky lines) was 1.1 Å (~ 80 km/s) from 4200 Å to 5000 Å (Aug. 4) or 1.5 Å (~ 110 km/s) from 4000 Å to 5000 Å (Aug. 7) in the blue arm, and 1.4 Å (~ 50 km/s) in the spectral range from 7650 Å to 8650 Å.
The data were calibrated in a standard way, including flat-fielding with dome-flats, wavelength calibration with arc-lamp-spectra, and flux calibration with spectroscopic standard-stars. The time information was converted to the barycentre of the solar system.
For the spectroscopy of QQ Vul no simultaneous photometry is available. The object was flux calibrated with the spectra of a non-variable comparison star also within the spectrograph's slit. Nevertheless, the continuum flux in the spectra still varied a lot – up to $0\overset{\mathrm{m}}{.}5$ at the same phase in different binary orbits, which we assume as the error of our flux calibration, although it could be caused by variations inside the system. But most probably it is due to slit-losses and changing transparency. On August 4 only 38 spectra were taken, covering just one half of a binary orbit. Because of the missing absolute photometry it would have been difficult to justify merging the data of both nights. I decided to analyse only the continuum-subtracted spectra from August 7 in the case of the emission lines, and the merged data set for the absorption lines, since there the variations are lower than the signal-to-noise ratio. For further analysis, the spectra were phase folded with the ephemeris given by SCHW2000.

The orbital mean blue spectrum (Fig. 4.1, top panel) looks similar to the one shown by SCHW2000. The continuum flux level is the same considering the assumed accuracy of the flux calibration. The most prominent lines are these of hydrogen and neutral and ionised helium. But there are also lines of carbon, oxygen, magnesium, and nitrogen. The average line profile seems to be broader in the data from 2000 than in the spectrum shown by SCHW2000. This is intrinsic to the data, because the spectral resolution in 2000 was higher. In the red arm the spectrum (Fig. 4.1, bottom panel) shows larger differences when compared to the one published in CAT1999. The Paschen lines are not as bright as in their mean spectrum, and in the data from 2000 there is an additional blue continuum component, which causes the continuum level to rise below 8000 Å.

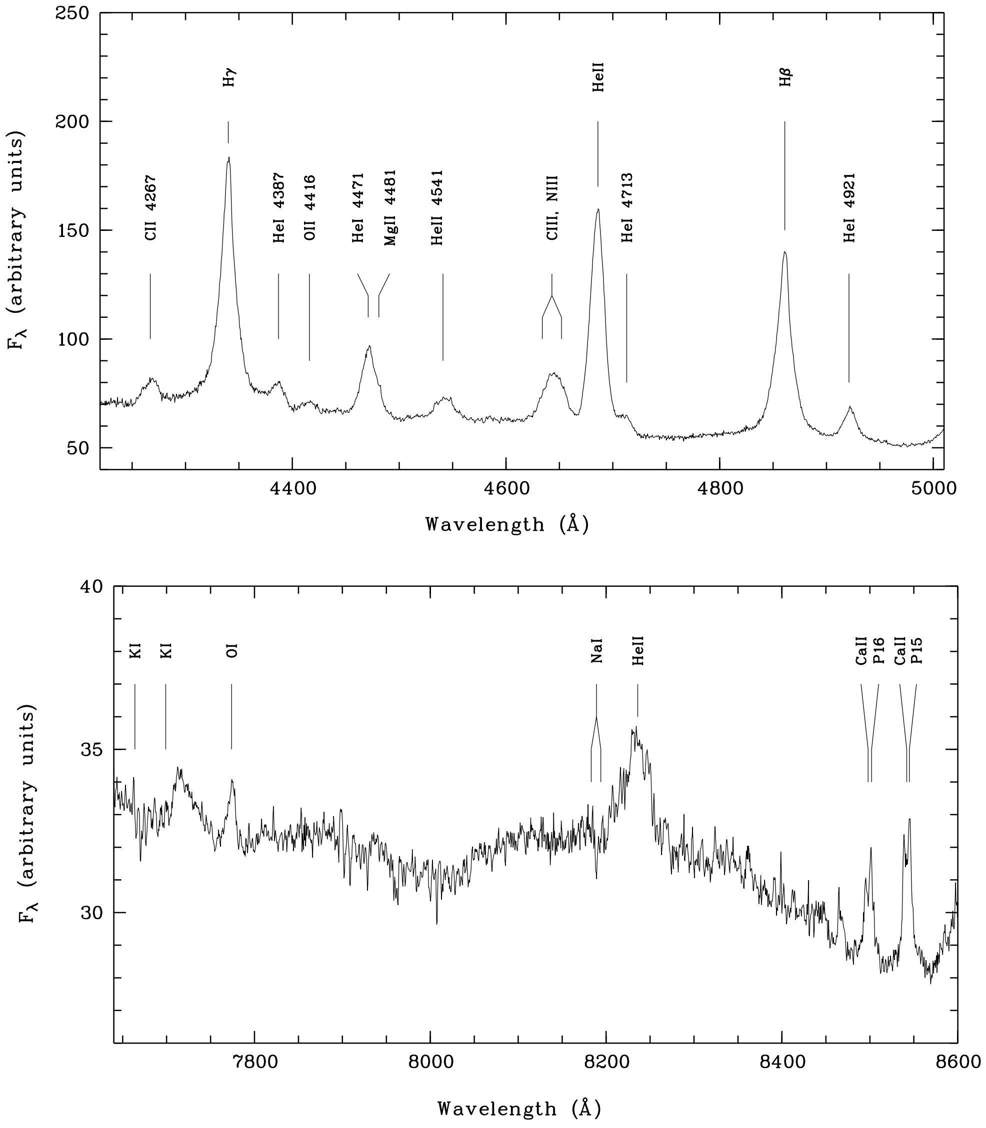

Figure 4.1: QQ Vul: averaged spectra (over the full orbit) from August 7, 2000, *top*: blue arm, *bottom*: red arm

4.2.1 Light curves

The radiation measured from polars consists of multiple components (see section 1.1.3), which show differing behaviour with orbital phase, and whose spectral energy distributions are also different. Thus they have different, variable shares on the over-all flux in a certain band-pass.

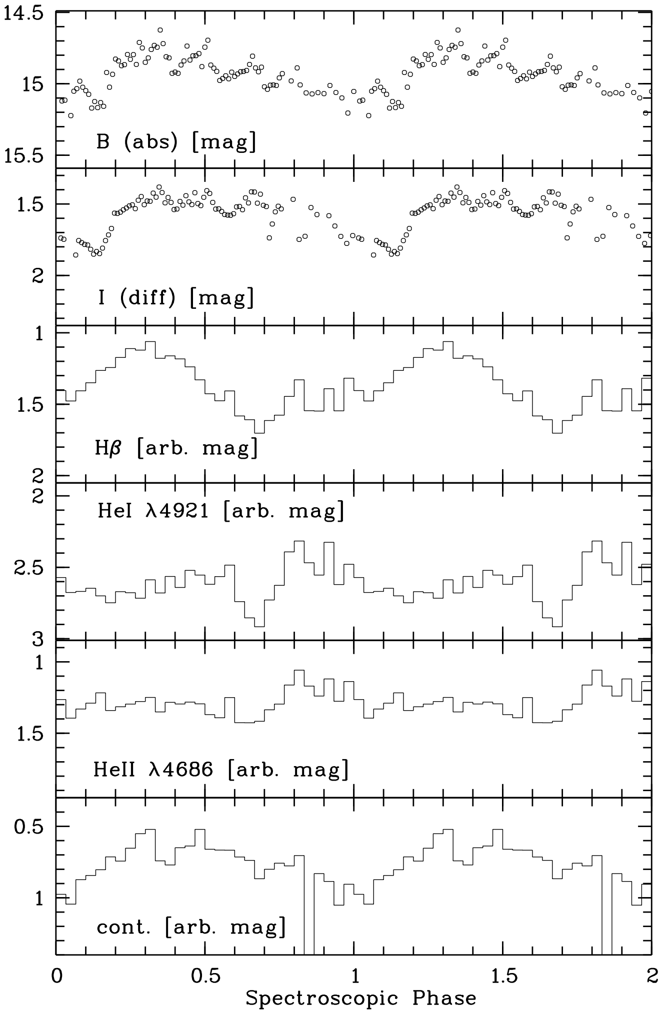

Figure 4.2: QQ Vul: continuum and line light-curves from Aug. 7, 2000. 'Cont.' is an average of the spectral flux in the range 4760 to 4810 Å – at phase 0.85 one data point was rejected because of loo low S/N.

In Fig. 4.2, light-curves of QQ Vul from Aug. 7, 2000 are shown. The light-curves of the emission lines were created from continuum-subtracted spectra by averaging from $v = -1500$ to 1500 km/s with respect to the rest-wavelength of each line. For comparison, the continuum light-curve, as determined from the trailed spectra by averaging from 4760 to 4810 Å, is

shown in the lower panel.
The light-curves created out of the spectra were transformed to arbitrary scaled magnitudes according to $mag = -2.5 * \log_{10}(flux) + 5.2$, to be comparable to the broad-band ones.

As can be seen, 'cont.' strongly resembles the B-band light-curve. This proves that there are no big changes in the spectral flux introduced by varying slit-losses or changing transparency, but all structure seen in the line light-curves is intrinsic to the system.
However, deviations from the broad-band light-curves are expected, because they were not observed fully synchronously.

The broad-band light-curves in the B and I filter are similar in the amount of the variability ($\sim 0\overset{\mathrm{m}}{.}5$) and the position of the primary minimum (at phase 0.15). In the I-band the light-curve is smoother – it doesn't show as strong short-term variations as the B-band light-curve. Also, after the secondary minimum at phase 0.57, the I-band light-curve shows more flux.

The light curves (Fig. 4.2) of Hβ and helium both show a minimum around phase 0.68. But the maxima are at different phases: The ballistic stream in the trailed spectrum of Hβ is brightest before phase 0.5 (at phase 0.3), when the irradiated side is visible. He I and He II are brightest after phase 0.5 (at 0.8), meaning that the unirradiated side is brighter than the irradiated one. The minimum doesn't coincide with either the primary or secondary minimum of the broad-band data.

The combination of the results from the broad-band data with the line light-curve of Hβ leads to the following picture: The maximum of intensity in these three light-curves (at phase 0.3) is caused by the best visibility of the irradiated side of the accretion stream/curtain. Afterwards the brightness of the stream drops to a minimum at phase 0.67, probably because of least projected area or self-absorption in the stream. The additional emission seen in the I and – weaker – in the B-band may be caused by cyclotron emission. This interpretation is supported by the fact that this contribution is smaller in B and not seen in the Hβ at all. The primary minimum, however, seems to have no connection with the accretion stream, so that origin of it in cyclotron beaming and a self-eclipse of the accretion column is likely.

In the case of the light-curves of He I and He II, the flux maximum around phase 0.8 and the – in comparison to Hβ – low flux level at phase 0.3, indicate that their main excitatory mechanism cannot be irradiation by the white dwarf or the accretion column.

4.2.2 Absorption lines

The analysis of the absorption lines of QQ Vul is concentrated on the Na I doublet at 8183/8194 Å (see Fig. 4.3), because it has the highest signal-to-noise level compared to the other ones.

To check the orbital ephemeris used for phase-folding the data, a double

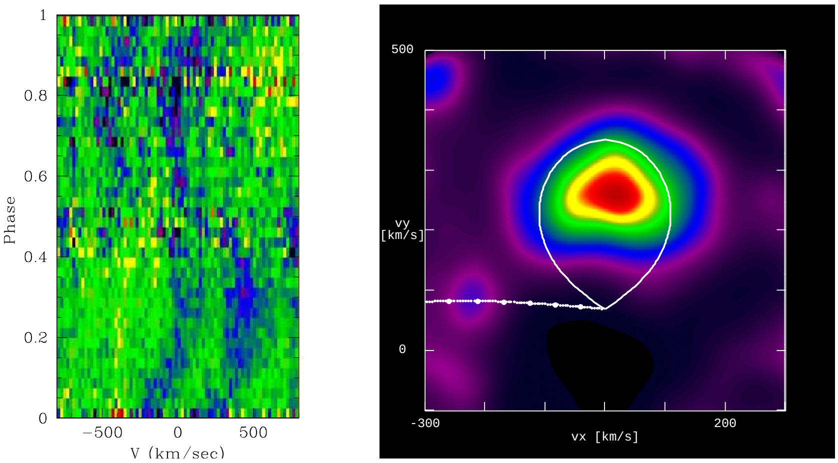

Figure 4.3: QQ Vul: The sodium lines (merged from both nights) and the resulting Doppler-tomogram with the overplotted outline of the secondary and the resulting ballistic stream for $Q = 1.75$, $M_1 = 0.54$, $i = 65°$, the favoured parameters by SCHW2000 (colours: Fig. A.1)

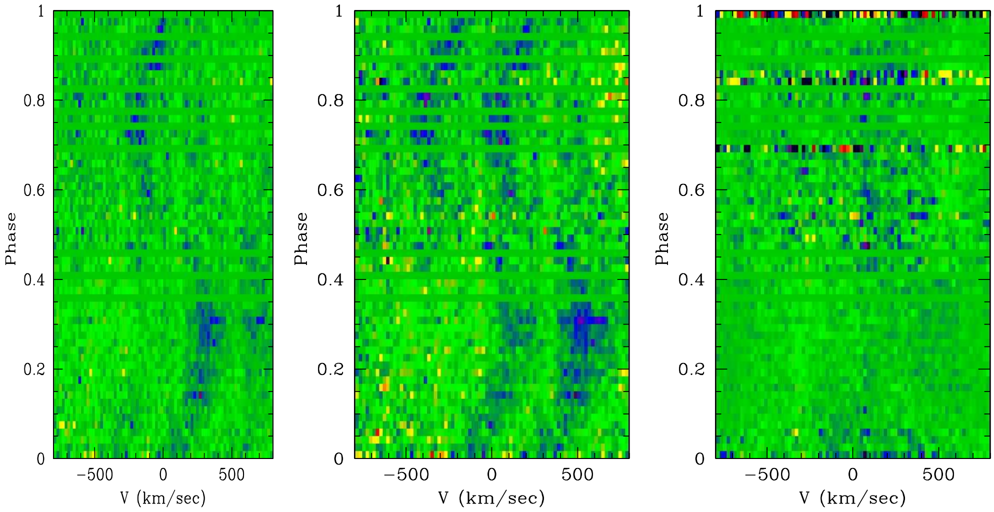

Figure 4.4: QQ Vul: Summation of the sodium lines from Fig. 4.3: *left*: the deconvolved line profile, *middle*: the fit, *right*: the residuals of the fit (colours: Fig. A.1)

Gaussian with fixed intensity-ratio and distance was fitted to the sodium doublet in all spectra. The radial velocity curve (Fig. 4.5) was fitted assuming circular orbital motion, i.e. $v(t) = \gamma + K' \sin(\omega(t - t_0))$. The parameter K' is the radial velocity amplitude of the center of light of this spectral line, and is normally deviating from the velocity amplitude of the center of mass.

The derived values are: system velocity with respect to the barycenter γ =1(4) km/s, and $K'_{2,NaI}$=259(5) km/s. The point of blue-to-red zero crossing is shifted to orbital phase 0.044(4). Using this shift, an additional time for a long-term spectroscopic ephemeris was determined:

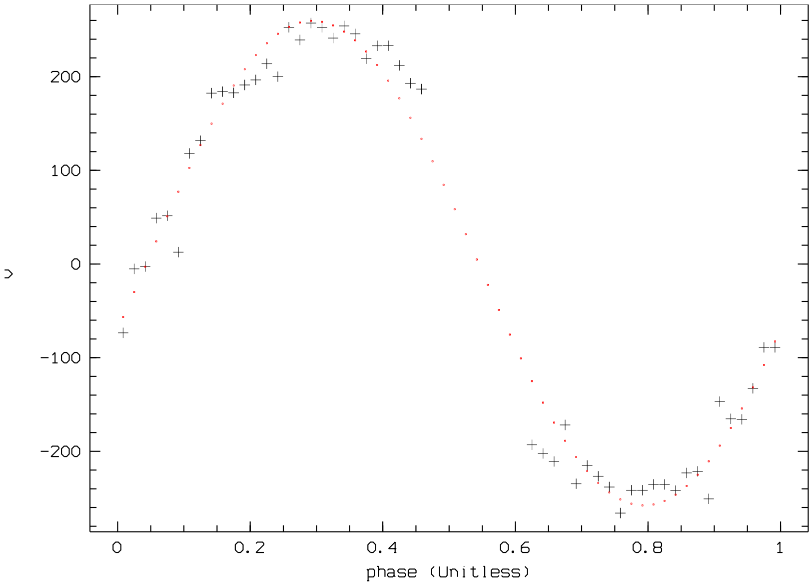

Figure 4.5: QQ Vul: Radial velocity measurements (in km/s) of the sodium doublet (black crosses) and the fitted sine curve (red squares)

$T_0[HJD] = 2451764.4780(10)$. This point is at the edge of the error range of the SCHW2000 ephemeris. From the values of t_0 given in SCHW2000 (their Table 3) and the timing of the blue-to-red zero crossing determined here, a new spectroscopic ephemeris was derived (Eq. 4.1).

$$T_0(HJD) = 2448446.47093(48) + E \times 0.154519983(47) \tag{4.1}$$

The numbers in brackets are the uncertainties in the last digits. Fig. 4.6 shows the values of observed minus calculated timings with respect to this ephemeris.

For phase folding of all the data, the calculation of orbital phase was done with the new ephemeris (Eq. 4.1).

To calculate a Doppler-tomogram of the sodium doublet it was necessary to deconvolve the two lines. This was done the same way as described for the data of AM Her: With Evolution Strategy the line profile is determined for each spectrum, which fits the observed doublet best when summing two of them separated by the distance of 11.568 Å and multiplied with the appropriate factor. The intensity ratio between the blue line and the red line is in the case of QQ Vul again 0.75. The results are shown in Fig. 4.4.

In the Doppler-tomogram (Fig. 4.3) the sodium absorption is located at the expected position of the unirradiated hemisphere of the secondary, when calculated with the system parameters favoured by SCHW2000.

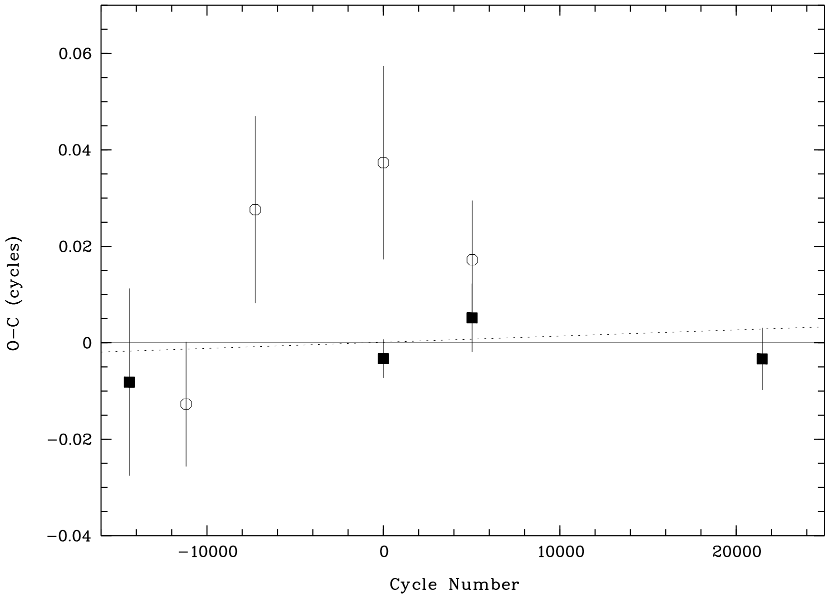

Figure 4.6: QQ Vul: Observed minus calculated timings with respect to the spectroscopic ephemeris given by Eq. 4.1. The filled squares are measurements of the blue-red zero crossing obtained from the sodium lines, the open circles were gained from the NEL of He II. All the data points below cycle 10000 are those from SCHW2000. The dashed line marks their ephemeris.

4.2.3 Emission lines

After reduction of the data it became apparent that the flux of the emission lines in the blue channel varied from one orbit to the next by a factor of 1.2. This may have been caused by slit-losses or intrinsic variability. Since a changing line-flux would prevent using tomographic methods (no intrinsic variations are allowed!), I decided to scale the flux in the last frames to the one at the same orbital phase one orbit ago. This was done using the line-flux of Hγ. With this correction, the continuum light-curve obtained from the blue channel spectra (Fig. 4.2, lower panel) looked similar to the broad-band continuum light-curve, and the corrected spectra are consistent with the photometric data. (Thus slit-losses were dominating.)

In the case of QQ Vul, the emission lines and the resulting Doppler-maps of different species are differing by large amounts. In the following they are described in detail.

The narrow emission line component (NEL)

The Ca II lines at 8498 Å and 8542 Å show nearly no stream emission, but a dominant NEL (Fig. 4.7). The NEL is also prominent in the other atomic lines (hydrogen and He I λ4921), but very faint in the case of He II λ4686 (Fig. 4.8), especially when compared with the spectra from SCHW2000

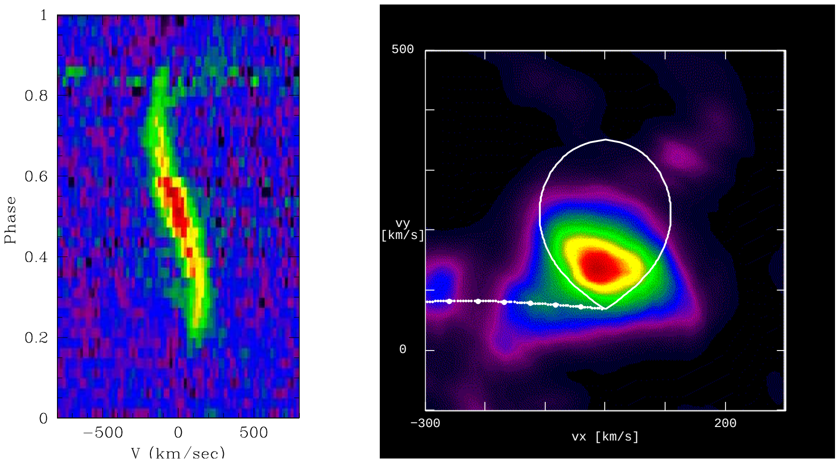

Figure 4.7: QQ Vul: The calcium line at 8542 Å, Ca II $\lambda8498$ looks similar (overplotted the outline of the secondary and the resulting ballistic stream for $Q = 1.75$, $M_1 = 0.54$, $i = 65°$, the favoured parameters by SCHW2000, colours: Fig. A.1)

(Figs. 4.15 to 4.17).

In the tomogram of Ca II, a clear asymmetry is seen between the leading ($v_x < 0$) and trailing hemisphere ($v_x > 0$) . The leading side shows emission extended farther from the L_1 to higher v_y. This result is confirmed by Roche-tomography. In Fig. 4.14 it is seen that the map shows more intensity near the L_1 at phase 0.25. But the emitting region is more extended towards the unirradiated side on the tailing hemisphere, best visible at phase 0.75. This is probably caused by the stream-component, which around this phase is lying parallel to the NEL in the trailed spectra and is thus also fitted, while at phase 0.25 it is crossing with a high inclination and is thus nearly completely neglected.

An asymmetric emission region with a depletion on the leading side is normally explained by shielding of the secondary from the irradiation by the magnetically guided stream/curtain. The case found here is unexpected, because the side where the stream should be is brighter. One explanation could be that the accretion stream irradiates the secondary's surface.

The NEL of $H\beta$ is in the tomogram located on the irradiated surface of the secondary star (Fig. 4.8).

In the case of atomic and ionic helium the NEL is shifted to lower v_y (also Fig. 4.8). In the trailed spectra no clear sine-curve at the position of the expected NEL (marked with a black curve) is detected, but just an emission component at $v_y \sim 0$ between phases 0.4 and 0.6. I want to draw special attention to the lack of NEL emission in the phase range 0.3 to 0.4. It may be possible that the presence of the $v_y \sim 0$-component around phase 0.5 mimics a true NEL in the tomogram.

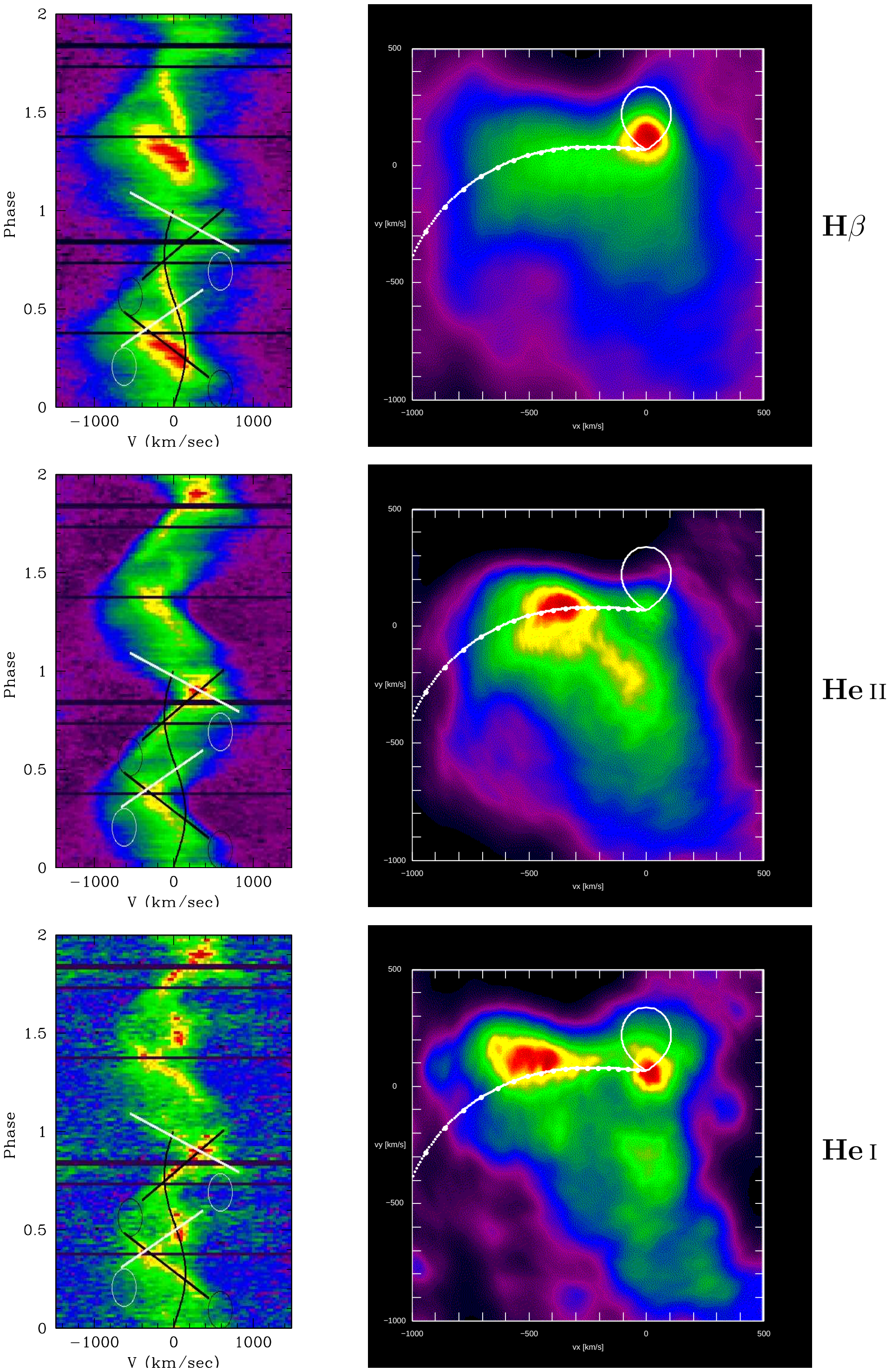

Figure 4.8: QQ Vul: The emission lines Hβ, He II λ4686, and He I λ4921, *left*: phase folded spectra (overplotted the positions of structures seen in the Doppler-tomograms, see text), and *right*: the resulting Doppler-tomograms (overplotted the Roche-lobe contour and the ballistic stream calculated for $Q = 1.85$, $i = 65°$, and $M_1 = 0.54\,M_\odot$, the values from CAT1999) (colours: Fig. A.1)

The stream component

The interpretation of the emission not arising on the secondary star is complicated. As can be seen in Fig. 4.8, the line profile and the resulting Doppler tomograms look different in any of the shown cases. (The other hydrogen lines look similar to Hβ, and the emission lines further detected in the observed wavelength regions have too low a signal-to-noise ratio to yield more information from them or are blended like He I λ4471 with Mg II λ4481.) Emission located at the expected position of a ballistic stream in velocity-coordinates is best seen in the case of Hβ, were it can be detected down to $v_x \sim -800$ km/s, distributed without much substructure. No signature of a well-focussed structure dominated by the magnetic field (a stream, curtain, etc.) is found. Although the NEL is the brightest feature in the tomogram, the over-all flux arising in the stream is much higher, as can be seen also in the line light-curve (Fig. 4.2), which shows the flux maximum of Hβ at $\phi \sim 0.3$ and not around phase 0.5 as would be expected for the NEL. After phase 0.5 the stream component is clearly fainter in Hβ, suggesting that the irradiated side of the stream is much brighter than the unirradiated one.
The other emission lines show more sub-structure within the stream component: There is a peak on the calculated position of the ballistic stream around $v_x \sim -500$ km/s for He I, and around $v_x \sim -400$ km/s for He II. In the tomogram of He II there is a region of enhanced emission extending from the peak in the direction of the lower right quadrant, ending near $v_x = 0$. This feature is not as prominent in the He I tomogram, but there also is some emission near $v_x \sim 0$ and $v_y \sim -300$ km/s. Since it has no v_x, this emission is arising from matter moving nearly perpendicular to the connecting line of both stars (probably in the magnetically guided stream).

In Fig. 4.8, the positions of the tomogram's features in the trailed spectra are schematically overplotted. The black sine-curve follows the NEL, the straight black lines mark the position of the ballistic stream, while the white lines trace the component with $v_x \sim 0$. The circles drawn there show where there is a lack of emission from the two parts of the stream, possibly caused by their small projected area.

The line profile of He I λ4471 (not shown) is similar to the one of He I λ4921. In case of the emission line Mg II λ4481 (not shown), the NEL is the dominating feature, although a stream component is found as well, which has a similar shape as in the He I lines.
Further analysis is complicated by the overlap of both lines in a wide phase range. Thus it is impossible to calculate meaningful Doppler-tomograms or calculate line light-curves.

4.2.4 Roche-tomography

Na I $\lambda\lambda 8183/8194$

To determine the system parameters of QQ Vul, an entropy-grid for the sodium lines was calculated with AStRoTom. The highest entropy at a common level of χ^2 was reached at $Q = 1.5$, $i = 85°$, and $M_1 = 0.6\,M_\odot$. In Fig. 4.9, the slices through the entropy grid containing the best-fit value are shown. The fitted spectrum and the residuals with respect to the observed spectrum are shown in Fig. 4.10, the respective Roche-map in Fig. 4.11.

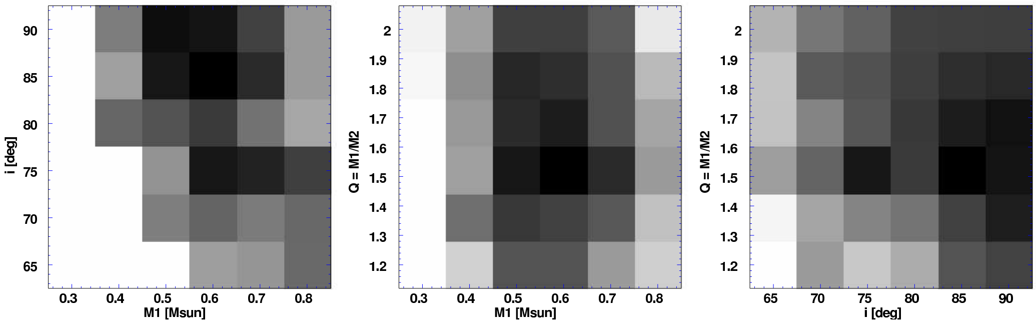

Figure 4.9: The entropy maps for the fits onto the Na I line (Fig. 4.3), with respect to the system parameters Q, i, and M_1 are shown as slices of the data cube, which are containing the best-fit value for each map: $Q = const.$-plane (*left*), the $i = const.$-plane (*middle*), and the $M_1 = const.$-plane (*right*). Black denotes higher entropy.

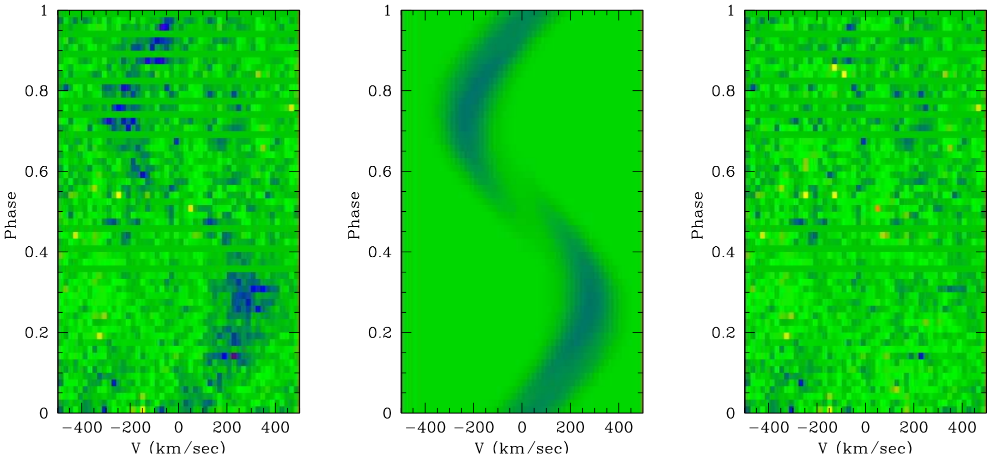

Figure 4.10: The spectrum for the best fit to the Na I line (Fig. 4.3): *left*: observed spectrum, *middle*: fitted spectrum, *right*: residuals (all with the same cut levels, colours: Fig. A.1).

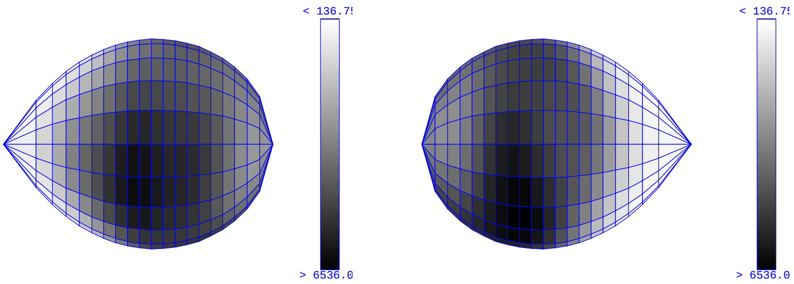

Figure 4.11: The intensity map of the fit shown in Fig. 3.12 shown for $i = 90°$ at phases 0.25 and 0.75.

Ca II 8542

For the emission line of calcium, an entropy-grid was calculated as well. Figs. 4.12, 4.13, and 4.14 show the results. The highest entropy value at roughly the same χ^2 was found at $Q = 1.4$, $i = 85°$, and $M_1 = 0.4\,M_\odot$.

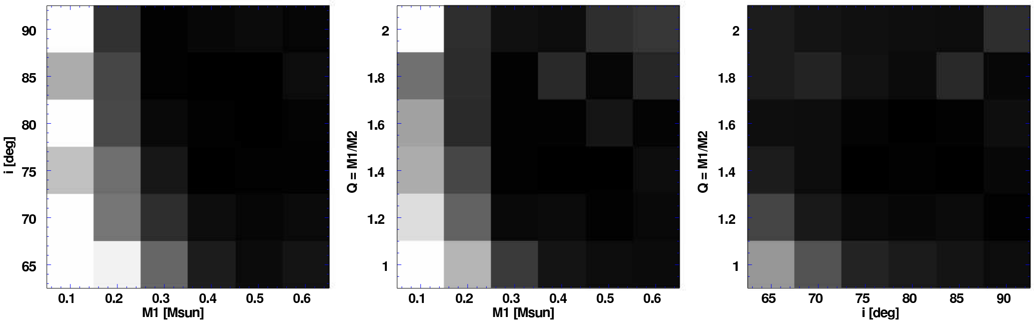

Figure 4.12: The entropy maps for the fits onto the Ca II line (Fig. 4.7), with respect to the system parameters Q, i, and M_1 are shown as slices of the data cube, which are containing the best-fit value for each map: $Q = const.$-plane (*left*), the $i = const.$-plane (*middle*), and the $M_1 = const.$-plane (*right*). Black denotes higher entropy.

Results

As can be seen at the spectra, fitting the data was successful for both, the sodium and the calcium line. Nevertheless, the resulting entropy-grids did not lead to an unambigious parameter determination.

For both lines, the highest entropy was achieved for a parameter set which is clearly ruled out, because an inclination of $i = 85°$ would result in an eclipse of most of the stream (and the white dwarf) by the secondary star, which is clearly not detected.

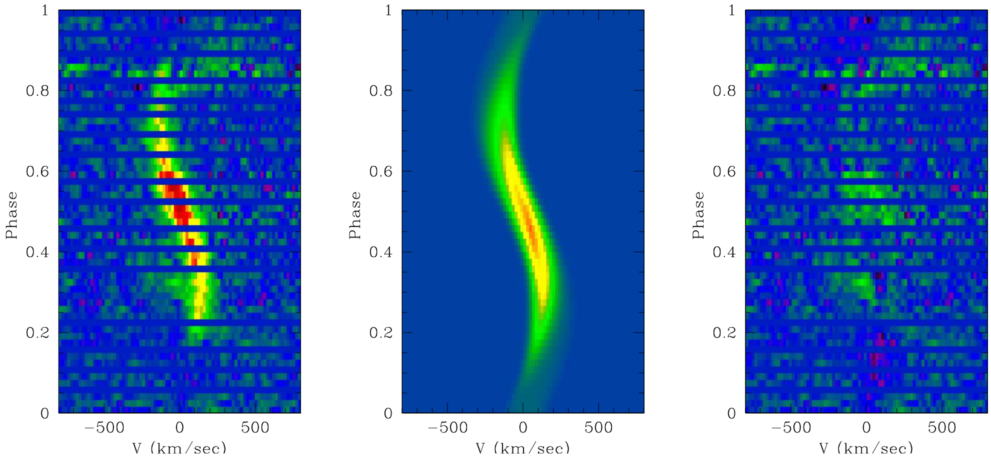

Figure 4.13: The spectrum for the best fit to the Ca II line (Fig. 4.7): *left*: observed spectrum, *middle*: fitted spectrum, *right*: residuals (all with the same cut levels, colours: Fig. A.1).

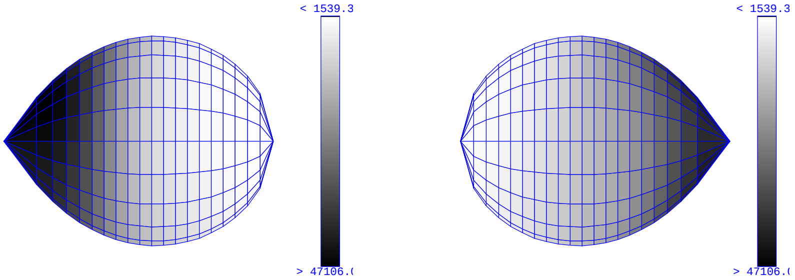

Figure 4.14: The intensity map of the fit shown in Fig. 3.15 shown for $i = 90°$ at phases 0.25 and 0.75.

In the case of the sodium line, the parameter best restricted is the mass of the white dwarf, M_1, to the range 0.5 to 0.6 $\mathrm{M}_\odot$. However, this value cannot be claimed the real one, because all system parameters are linked via the radial velocity of the Roche-lobe. Thus M_1 as well as Q are biased by the too high value for the inclination.

A second, local maximum of the entropy is found at $i = 75°$. Although this value for i would be more reasonable, from the maximum-entropy aspect it is less significant.

With the calcium line, the parameter determination didn't result in a clear entropy maximum, as can be seen in Fig. 4.12. It was not possible to restrict the parameter range. Reasons for this could be the contamination of the NEL in the trailed spectrum with emission from the accretion stream, or the only weak ability to restrict the parameter range with an emission line from the irradiated hemisphere.

4.2.5 Discussion

The system parameters Using Roche-tomography on our data, it was not possible to enhance the accuracy of the system parameter values, because the best fit was achieved for a parameter combination ($Q = 1.4..1.5$, $i = 85°$, and $M_1 = 0.4..0.6\,M_\odot$) which is clearly ruled-out by the non-detection of an eclipse by the secondary in our data.
The Doppler-tomograms of the sodium doublet and the Ca II line are fitting well with the calculated Roche-lobe from the system parameters determined by SCHW2000. Thus these values still seem reasonable.

Compared with the values determined by WAT2003 ($Q = 1.59$, $i = 72°$, and $M_1 = 0.58..0.66\,M_\odot$), the values determined here are still in a reasonable range, with the exception of i.
The larger mass ratio in SCHW2000 is compensated by the higher inclination assumed by WAT2003, so the velocity range covered by the calculated Roche-lobe is similar. With our data it is impossible to favour one of these parameter combinations.

The stream component To simplify the comparison of the spectroscopic data obtained in 2000 with the data published by SCHW2000, I re-present the emission line data from 1986, 1991, and 1993 in Figs. 4.15, 4.16, and 4.17.

The emission lines of QQ Vul observed in 1986, 1991, and 1993 are quite similar for all species at every one epoch. The dominating structure is the NEL. In the tomograms, the accretion stream is located near the expected position of the ballistic stream when calculated with the favoured parameters from SCHW2000. Emission is detected up to velocities $v_x \sim 500..700\,\mathrm{km/s}$. Strongly enhanced emission from the stagnation region is not seen in all three spectral lines. The line light-curves have a double-hump shape (see also SCHW2000, their Fig. 11), where the maxima are located near phase 0.2 and 0.8. In 1986, the maximum near phase 0.8 is clearly fainter than the one at 0.2. This can be explained by excitation of the line emission by irradiation from the white dwarf, with the illuminated side being brighter due to optical thickness of the stream for both, the irradiating continuum and the emitted lines.

In the data from 2000, a behaviour similar to the one at the earlier epochs is found only in the case of the Hβ line. Both, the atomic and ionic helium lines, show a different behaviour in the spectra and in the line light-curves (Fig. 4.2), where there is either no clear maximum (He II), or it is at a different phase (near 0.8 for He I).

Putting together all the information, one can try to get some hints on the excitation mechanisms for the different lines:
The Balmer-lines could be either excited by bound-bound absorption of radiation from the white dwarf or the accretion region, which are thought to emit

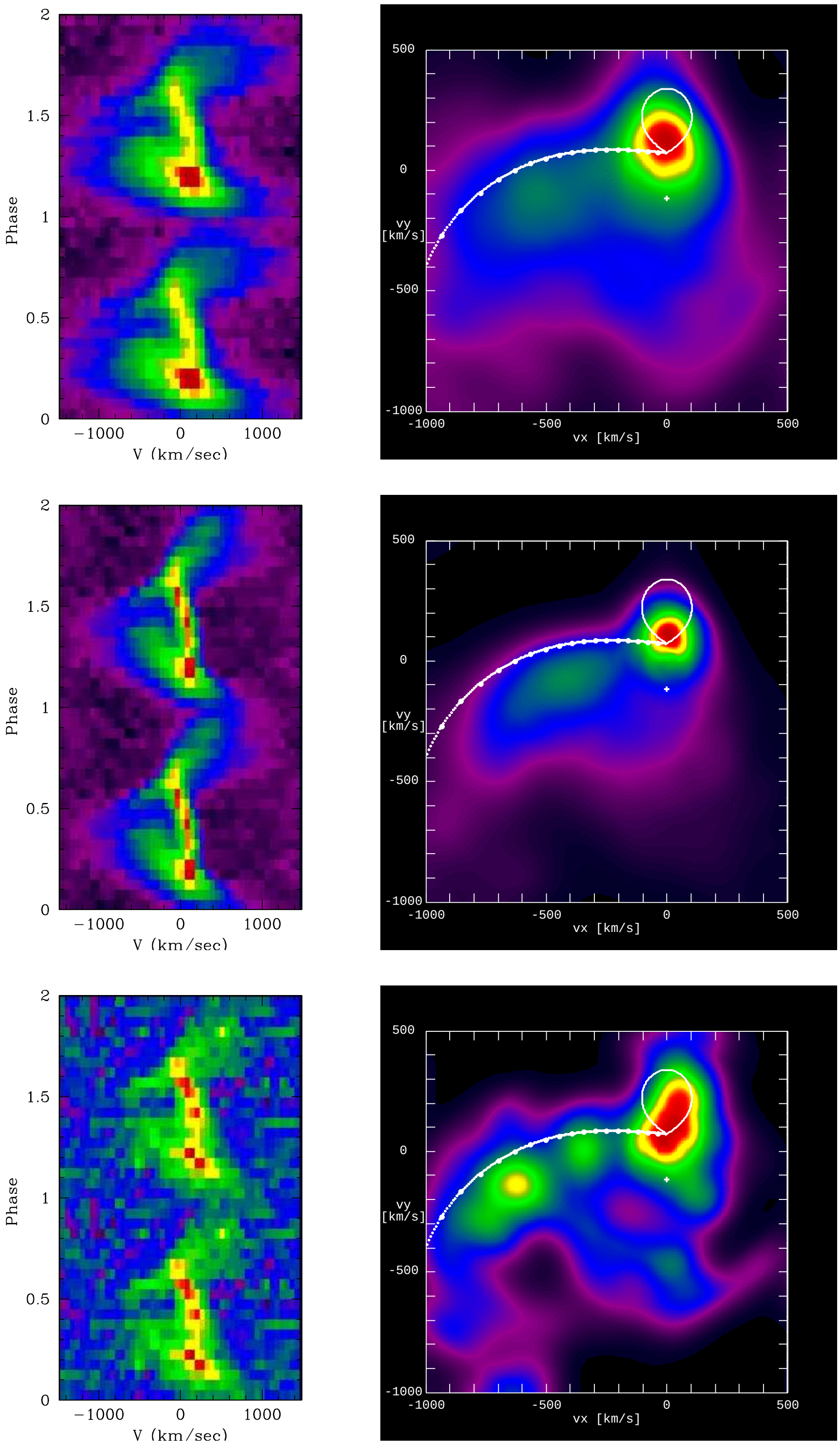

Figure 4.15: QQ Vul: the emission lines from 1986 of Hβ, He II λ4686, and He I λ4921, phase folded spectra and the resulting Doppler-tomograms (colours and contours: see Fig. 4.8)

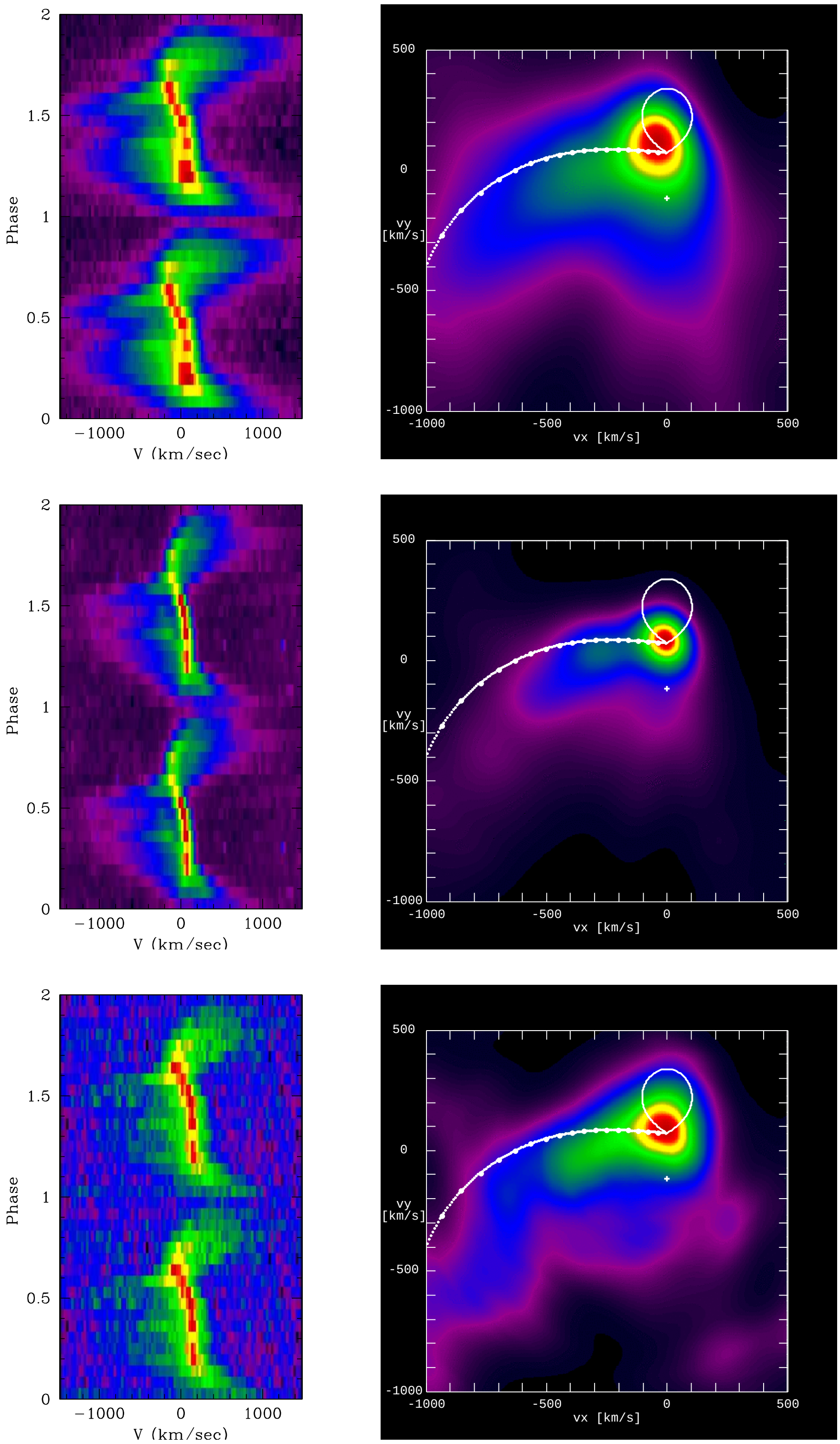

Figure 4.16: QQ Vul: the emission lines from 1991 for Hβ, He II λ4686, and He I λ4921, phase folded spectra and the resulting Doppler-tomograms (colours and contours: see Fig. 4.8)

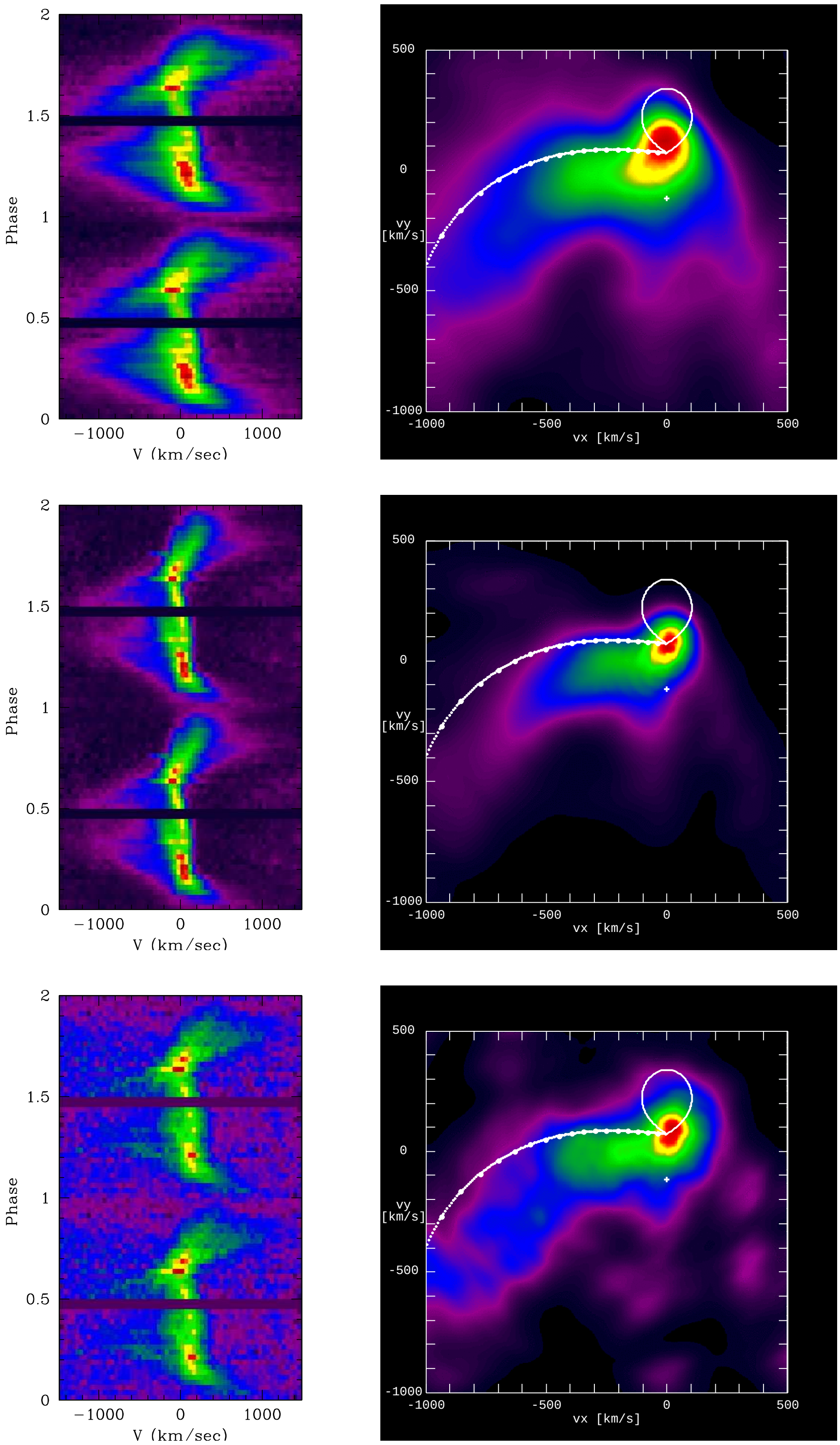

Figure 4.17: QQ Vul: the emission lines from 1993 of Hβ, He II $\lambda4686$, and He I $\lambda4921$, phase folded spectra and the resulting Doppler-tomograms (colours and contours: see Fig. 4.8)

according roughly to a black-body, or as recombination radiation of ionised hydrogen.

The He II emission line shows that there are even photons capable to singly ionise helium (24.6 eV, Sansonetti et al., 2004). The photon energy to get He III (54.4 eV) is quite high. Together with the observation that the NEL of He II is comparatevily weak, and its stream emission is highly localised in a region which may be identified with the coupling region, it seems that the main source of excitation of the He II $\lambda4686$ line cannot be recombination of He III. Collisions with free electrons from the hydrogen ions, or additional heating mechanisms have to be effective. Ferrario and Wehrse (1999) calculated spectra of a magnetically guided part of an accretion stream. When taking into account only irradiation with X-rays, they find it difficult to excite helium lines, but strong hydrogen line-emission is found. With additional heating through energy taken out of the magnetic field in the stagnation region, their model creates also helium emission lines of a comparable flux.

The location of the bright emission region in the Doppler-tomogram of He II supports the interpretation of tracing the stagnation region. The polars UZ For and HU Aqr both showed enhanced emission following the expected location of the stagnation region in He II (Schwope et al., 1999). The emission located at $v_x \sim 0$ and $v_y \sim 200..400$ km/s in the tomograms of He I and He II in the data from 2000 can then be interpreted as arising from matter whose velocity is completely redistributed from v_x to v_y due to interaction with the magnetic field. The magnetically guided stream itself is not visible, because there the additional energy source is absent.

The presence of Ca II and Mg II emission lines indicates incoming flux with energies above the first ionisation levels of calcium and magnesium atoms (6.1 eV and 7.6 eV, respectively). Because of the low energies necessary to reach the second ionisation level (11.9 and 15.0 eV), these lines can be excited by recombination of Ca III and Mg III, or by collisions with electrons.

The NEL of He I is much brighter compared to the stream emission than in the case of He II. Thus bound-bound absorption is likely to be the main excitation source. The stream component shows a bright region near $v_x \sim -500$ km/s, at v_y-velocities slightly larger than expected in a ballistic stream at these x-velocities. The absolute value of the v_x of this bright region is larger than the one observed at the He II line. I have no explanation for this finding, but I think it is worth to be studied further. However, the location near the bright region in He II suggests recombination to be the excitation mechanism.

Chapter 5

Summary and Conclusions

Spectroscopic data obtained in August 2000 for two polars – AM Her and QQ Vul – were analysed with indirect imaging methods.

Roche-tomography, a method to determine the intensity distribution of spectral lines on the surface of the secondary star from time-resolved spectroscopy, was applied to the data in order to determine more precise values of the main system parameters inclination i, mass ratio Q, and the mass of the white dwarf, M_1.
My code used for Roche-tomography – AStRoTom – is calculating intensity maps on the Roche-lobe, which is assumed to be the location of the photosphere of the secondary star in the case of cataclysmic variables. The maps are modified by Evolution Strategy until a fit of the projected spectra to the data is achieved. Due to the low signal-to-noise ratio of the input data and the fact that the problem is underdetermined, some kind of entropy has to be introduced as an additional regularisation parameter. This entropy, in turn, can be used to get information on the system's parameters. For this purpose, intensity maps are calculated for different values of the system parameters, whose projected spectra fit the input data to the same χ^2-level and have maximum entropy. The parameter combination corresponding to the map with the maximum reached entropy can be considered as the most probable one.
AStRoTom performed well in reproducing synthetic maps and the corresponding initial system parameters. With observational data for both, AM Her and QQ Vul, intensity maps of emission lines arising on the irradiated hemispheres of the secondary (Ca II), and absorption lines originating on the undisturbed one (Na I), were calculated for pre-defined parameter values. The determination of system parameter values from the spectral data with AStRoTom was not successful. For AM Her, the maximum entropy solution was found at the edge of the parameter range allowed by physical considerations. Thus the parameters could not be restricted. In the case of QQ Vul, the highest entropy was reached at an inclination $i = 85°$, which is ruled out by the non-detection of an eclipse by the secondary star in the observational data.
Most likely the problems with the parameter determination are caused by a too low quality of the input spectra.

There are also several possibilities to improve AStRoTom, which will be implemented in the future.

To analyse the time-resolved emission lines arising in the accretion stream of both systems, another indirect imaging method was used – Doppler-tomography. In this approach all variations in the spectral line shape and flux are attributed to changing projections of the system due to its orbital motion. The projected velocities of the system's constituents onto the line-of-sight are thus resulting in time-dependent Doppler-shifts of the lines emitted there. From time-series of spectra, a map can be calculated, which shows the intensity distribution in velocity space, projected onto the system's orbital plane.

The emission line data of AM Her show details which are likely not compatible with the standard Roche-lobe overflow model. I suggest a model with the accretion stream starting somewhere else than at the Lagrange-point from the secondary, taking effects of a non-vanishing velocity-component perpendicular to the orbital plane, v_z, into account. The emission lines in the trailed spectra show large variations within the three consecutive nights. It has to be studied further, how these changes can be interpreted in terms of enhanced models for the accretion in magnetic CVs.

In the case of QQ Vul, the emission lines of hydrogen and atomic and singly ionised helium exhibit large differences in the time-dependent line-profiles and the resulting Doppler-tomograms. Over-all, the data of this object are consistent with the standard model of polars, although they show details which were not reported before. The emission of the hydrogen lines is consistent with being mainly excited by irradiation with high-energy photons. In the case of the ionised helium line, irradiation seems to play a minor role, whereas it is likely that the necessary energy is provided by the magnetic field in the region where the free-falling matter is captured by the white dwarf's magnetic field. The behaviour of the lines of atomic helium is consistent with being excited by a mixture of both, irradiation and recombination of ionised helium.

New data sets obtained even for well-studied polars show that our understanding of these systems is still highly limited. A better knowledge of this rare species of binaries would give insights in stellar evolution and high-energy physics, which is not possible to be obtained from more 'ordinary' stars.

The data presented in this work revealed details in the emission line profiles of the two polars AM Her and QQ Vul, which showed that the processes of accretion and line excitation in these systems is much more complicated than described by the simple models available today. New models should be able to describe the interaction of charged matter in a complicated magnetic field, like the superposition of the ones of the white dwarf and the secondary star. Since the plasma is in turn influencing the magnetic field structure, a magneto-hydrodynamic approach is needed for the accretion stream. It may be necessary to create a model also of the Roche-lobe filling secondary star, because due to its deviation from spherical symmetry and its fast rotation, the assumptions of stars with main-sequence properties may be inappropriate. An adequate model would have to describe the transport of energy and matter from the inner parts up to the outer layers of the stellar atmosphere.

To understand the details of the intensity distribution in the accretion stream, the mechanisms of line excitation and energy transport have to be modelled.

The success of attempts of determining the spatial structure of these systems from geometrical considerations (e.g. with Roche-tomography) is limited by the signal-to-noise ratio of the data, because a number of free parameters have to be linked by additional regularisation terms (entropy). These additional assumptions are nevertheless also required by the fitting problem itself, because certain locations on the star's surface cannot be distinguished from each other in velocity space. In systems showing an eclipse by the secondary star (i.e. system inclination $i \gtrsim 75°$), more information on the position is included in the line profiles.

With data having a higher signal-to-noise ratio, the geometry could be determined better. Hopefully we will get access to data obtained with 8m-class telescopes with an at least comparable spectral resolution in the future, especially at the LBT, a project in which the AIP is involved.

Data of much higher quality may make purely geometrical approaches like Roche-tomography obsolete, because the effects explicitely neglected (the variation of the line profile with changing aspect angle of the emitting region, the changes of the temperature structure and thus the line profile due to the deformed secondary star and its irradiation) should not be ignored anymore. It will be necessary to create a model of the structure of the donor star, which takes into account the deformation, fast rotation, and irradiation of the star while solving the equations of state and of energy transport.

Appendix A

The colour map

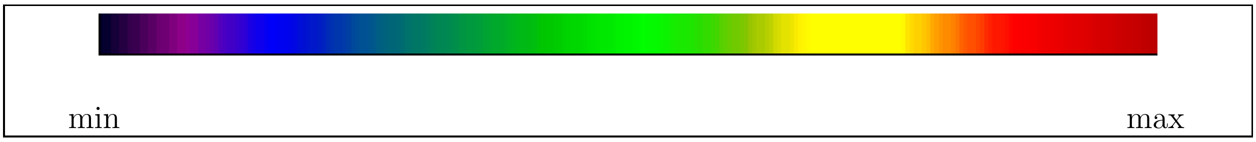

Figure A.1: The lookup-table (LUT) used to code intensities as colours.

List of Figures

List of Tables

Bibliography

Andronov, N. and Pinsonneault, M. H.: 2004, *ApJ* **614**, 326 15

Bailey, J., Ferrario, L., and Wickramasinghe, D. T.: 1991, *MNRAS* **251**, 37P 67

Barman, T. S., Hauschildt, P. H., and Allard, F.: 2004, *ApJ* **614**, 338 28, 36

Beardmore, A. P., Ramsay, G., Osborne, J. P., Mason, K. O., Nousek, J. A., and Baluta, C.: 1995, *MNRAS* **273**, 742 90

Berg, R. A. and Duthie, J. G.: 1977, *ApJ* **211**, 859 66

Beuermann, K.: 1997, in *Perspectives in High Energy Astronomy & Astrophysics*, Proceedings of the International Colloquium to Commemorate the Golden Jubilee of TIFR, Mumbai, India, August 12 – 17, 1996 20

Beuermann, K. and Thomas, H.-C.: 1990, *A&A* **230**, 326 87

Bobinger, A.: 2000, *A&A* **357**, 1170 22

Boffin, H., Steeghs, D., and Cuypers, J. (eds.): 2001, *Astrotomography: Indirect Imaging Methods in Observational Astronomy*, No. 573 in Lecture notes in physics, Springer-Verlag (Berlin/Heidelberg/New York) 23

Catalán, M., Schwope, A., and Smith, R.: 1999, *MNRAS* **310**, 123 62, 73, 90, 91, 93, 100

Chanmugam, G. and Wagner, R. L.: 1977, *ApJ* **213**, L13 66

Cropper, M.: 1998, *MNRAS* **295**, 353 90

Davey, S. and Smith, R.: 1996, *MNRAS* **280**, 481 22, 62, 68

Davey, S. and Smith, R. C.: 1992, *MNRAS* **257**, 476 62

de Martino, D., Matt, G., Gänsicke, B. T., Silvotti, R., Bonnet-Bidaud, J. M., and Mouchet, M.: 2002, *A&A* **396**, 213 67, 71

Efron, B. and Tibshirani, R.: 1993, *An Introduction to the Bootstrap*, Chapman & Hall (London, U.K.) 54

Ferrario, L. and Wehrse, R.: 1999, *MNRAS* **310**, 189 109

Gänsicke, B. T., Beuermann, K., and de Martino, D.: 1995, *A&A* **303**, 127 67

Gänsicke, B. T., Fischer, A., Silvotti, R., and de Martino, D.: 2001, *A&A* **372**, 557 67, 71

Gänsicke, B. T., Hagen, H.-J., Kube, J., Schwarz, R., Staude, A., Engels, D., Nogami, D., and Kuduz, M.: 2002, in *ASP Conf. Ser. 261: The Physics of Cataclysmic Variables and Related Objects*, p. 623 11

Gänsicke, B. T., Hoard, D. W., Beuermann, K., Sion, E. M., and Szkody, P.: 1998, *A&A* **338**, 933 67

Gänsicke, B., Beuermann, K., and Reinsch, K. (eds.): 2002, *The Physics of Cataclysmic Variables and Related Objects*, No. 261 in ASP Conference Series 20

Götz, W.: 1993, *AN* **314**, 69 18, 66, 71

Gull, S. and Skilling, J.: 1991, *Quantified Maximum Entropy: MemSys5 Users' Manual*, Maximum Entropy Data Consultants Ltd. (Royston, UK) 46

Hadrava, P. and Kubát, J.: 2003, in I. Hubeny, D. Mihalas, and K. Werner (eds.), *Stellar Atmosphere Modeling*, Vol. 288 of *ASP Conference Series*, p. 149 36

Hakala, P., Cropper, M., and Ramsay, G.: 2002, *MNRAS* **334**, 990 22

Hakala, P. J.: 1995, *A&A* **296**, 164 22

Harrop-Allin, M. K., Cropper, M., Hakala, P. J., Hellier, C., and Ramseyer, T.: 1999a, *MNRAS* **308**, 807 22

Harrop-Allin, M. K., Hakala, P. J., and Cropper, M.: 1999b, *MNRAS* **302**, 362 22

Harrop-Allin, M. K., Potter, S. B., and Cropper, M.: 2001, *MNRAS* **326**, 788 22

Heerlein, C., Horne, K., and Schwope, A.: 1999, *MNRAS* **304**, 145 22

Heise, J., Brinkman, A. C., Gronenschild, E., Watson, M., King, A. R., Stella, L., and Kieboom, K.: 1985, *A&A* **148**, L14 66, 67

Heise, J. and Verbunt, F.: 1988, *A&A* **189**, 112 67

Hellier, C.: 2001, *Cataclysmic Variable Stars*, Springer-Verlag (London, UK) 20

Hessman, F., Gänsicke, B., and Mattei, J.: 2000, *A&A* **361**, 952 18, 20

Horne, K.: 1985, *MNRAS* **213**, 129 21, 37, 38, 54

Horne, K.: 1994, in P. Gondhalekar, K. Horne, and B. Peterson (eds.), *Reverberation mapping of the broad-line region in active galactic nuclei*, No. 69 in ASP Conference Series, p. 23 46

Hudec, R. and Meinunger, L.: 1976, *Informational Bulletin on Variable Stars* **1184**, 1 66

Hutchings, J. B., Fullerton, A. W., Cowley, A. P., and Schmidtke, P. C.: 2002, *AJ* **123**, 2841 67

Kafka, S. and Honeycutt, R. K.: 2003, *AJ* **125**, 2188 91

Kube, J.: 2002, *Ph.D. thesis*, Georg-August-Universität Göttingen 22

Lamb, F. K., Pethick, C. J., and Pines, D.: 1973, *ApJ* **184**, 271 66

Marsh, T. and Horne, K.: 1988, *MNRAS* **235**, 269 24, 25

Matt, G., de Martino, D., Gänsicke, B. T., Negueruela, I., Silvotti, R., Bonnet-Bidaud, J. M., Mouchet, M., and Mukai, K.: 2000, *A&A* **358**, 177 67

McCarthy, P., Bowyer, S., and Clarke, J. T.: 1986, *ApJ* **311**, 873 90

McDermott, P. N. and Taam, R. E.: 1989, *ApJ* **342**, 1019 14

Mukai, K. and Charles, P. A.: 1987, *MNRAS* **226**, 209 90

Nousek, J. A., Takalo, L. O., Schmidt, G. D., Tapia, S., Hill, G. J., Bond, H. E., Grauer, A. D., Stern, R. A., and Agrawal, P. C.: 1984, *ApJ* **277**, 682 90

Nugent, J. J., Jensen, K. A., Nousek, J. A., Garmire, G. P., Mason, K. O., Walter, F. M., Bowyer, C. S., Stern, R. A., and Riegler, G. R.: 1983, *ApJS* **51**, 1 90

Olson, E. C.: 1977, *ApJ* **215**, 166 71

Orosz, J. A. and Hauschildt, P. H.: 2000, *A&A* **364**, 265 36

Osborne, J. P., Beuermann, K., Charles, P., Maraschi, L., Mukai, K., and Treves, A.: 1987, *ApJ* **315**, L123 90

Patterson, J.: 1984, *APJS* **54**, 443 87

Potter, S. B., Romero-Colmenero, E., Watson, C. A., Buckley, D. A. H., and Phillips, A.: 2004, *MNRAS* **348**, 316 32

Radon, J.: 1917, *Berichte über die Verhandlungen der Königlich Sächsischen Gesellschaft der Wissenschaften zu Leipzig, Mathematisch-Physikalische Klasse* **69**, 262 21

Rechenberg, I.: 1973, *Evolutionsstrategie*, Fromman–Holzboog (Stuttgart, Germany) 39

Robinson, E. L., Marsh, T. R., and Smak, J. I.: 1993, *The Emission Lines from Accretion Disks in Cataclysmic Variable Stars*, pp 75–+, Accretion Disks in Compact Stellar Systems 25

Rutten, R. and Dhillon, V.: 1994, *A&A* **288**, 773 32, 62

Salvi, N., Ramsay, G., Cropper, M., Buckley, D. A. H., and Stobie, R. S.: 2002, *MNRAS* **331**, 488 22

Sansonetti, J., Martin, W., and Young, S.: 2004, *Handbook of Basic Atomic Spectroscopic Data*, National Institute of Standards and Technology, Gaithersburg, MD, USA, version 1.1 edition, [Online] Available: http://physics.nist.gov/Handbook 109

Schmidt, G. D., Stockman, H. S., and Margon, B.: 1981, *ApJ* **243**, L157 67

Schwarz, R., Hedelt, P., Rau, A., Staude, A., and Schwope, A.: 2002, in B. Gänsicke, K. Beuermann, and K. Reinsch (eds.), *The Physics of Cataclysmic Variables and Related Objects*, No. 261 in ASP Conference Series, p. 167 69

Schwarz, R., Schwope, A. D., Beuermann, K., Burwitz, V., Fischer, J.-U., Fried, R., Lehmann, I., Mantel, K.-H., Mengel, S., Metzner, A., Misselt, K., Notni, P., Reinsch, K., Shafter, A., and Thomas, H.-C.: 1998, *A&A* **338**, 465 87

Schwope, A.: 2000, *Indirect imaging of polars*, Habilitation thesis, TU Berlin 16, 17

Schwope, A.: 2001, in H. Boffin, D. Steeghs, and J. Cuypers (eds.), *Astrotomography: Indirect Imaging Methods in Observational Astronomy*, No. 573 in Lecture notes in physics, Springer-Verlag (Berlin/Heidelberg/New York) 23

Schwope, A., Catalán, M., Beuermann, K., Metzner, A., Smith, R., and Steeghs, D.: 2000, *MNRAS* **313**, 533 19, 90, 91, 92, 93, 96, 97, 98, 99, 105

Schwope, A., Hambaryan, V., Staude, A., Schwarz, R., Kanbach, G., Steinle, H., Schrey, F., Marsh, T., Dhillon, V., Osborne, J., Wheatley, P., and Potter, S.: 2004, in *ASP Conf. Ser. 315: Magnetic Cataclysmic Variables*, p. 92 20

Schwope, A. D., Schwarz, R., Sirk, M., and Howell, S. B.: 2001, *A&A* **375**, 419 18

Schwope, A. D., Schwarz, R., Staude, A., Heerlein, C., Horne, K., and Steeghs, D.: 1999, in *ASP Conf. Ser. 157: Annapolis Workshop on Magnetic Cataclysmic Variables*, p. 71 81, 109

Sirk, M. M. and Howell, S. B.: 1998, *ApJ* **506**, 824 67

Skilling, J. and Bryan, R.: 1984, *MNRAS* **211**, 111 46

Southwell, K., Still, M., Smith, R., and J.S., M.: 1995, *A&A* **302**, 90 22, 62, 68, 69, 73

Spruit, H.: 1998, *Fast maximum entropy Doppler mapping*, astro-ph/9806141 31, 75

Spruit, H. C. and Rutten, R. G. M.: 1998, *MNRAS* **299**, 768 11

Staude, A., Schwope, A., Hedelt, P., Rau, A., and Schwarz, R.: 2004, in *ASP Conf. Ser. 315: Magnetic Cataclysmic Variables*, p. 251 69

Staude, A., Schwope, A. D., and Schwarz, R.: 2001, *A&A* **374**, 588 73

Steeghs, D.: 2003, *MNRAS* **344**, 448 49

Stockman, H. S., Schmidt, G. D., Angel, J. R. P., Liebert, J., Tapia, S., and Beaver, E. A.: 1977, *ApJ* **217**, 815 66

Szkody, P. and Brownlee, D. E.: 1977, *ApJ* **212**, L113 71

Tapia, S.: 1977, *ApJ* **212**, L125 66

Tinney, C. G. and Reid, I. N.: 1998, *MNRAS* **301**, 1031 83

Vrielmann, S. and Schwope, A. D.: 2001, *MNRAS* **322**, 269 22

Walker, M. F.: 1954, *PASP* **66**, 230 17

Warner, B.: 1995, *Cataclysmic Variable Stars*, No. 28 in Cambridge Astrophysics Series, Cambridge University Press (Cambridge, UK) 15, 20

Watson, C. and Dhillon, V.: 2001, *MNRAS* **326**, 67 32, 36, 37, 46, 48, 52, 54, 55, 63, 64

Watson, C., Dhillon, V., Rutten, R., and Schwope, A.: 2003, *MNRAS* **341**, 129 32, 38, 46, 48, 49, 55, 63, 68, 86, 87, 91, 105

Weicker, K.: 2002, *Evolutionäre Algorithmen*, B. G. Teubner (Stuttgart/Leipzig/Wiesbaden, Germany) 46

Wickramasinghe, D. T., Bailey, J., Meggitt, S. M. A., Ferrario, L., Hough, J., and Tuohy, I. R.: 1991, *MNRAS* **251**, 28 67, 71

Wolf, M.: 1925, *AN* **220**, 255 66

Young, P., Schneider, D. P., and Shectman, S. A.: 1981, *ApJ* **245**, 1043 68

Publications

Refereed papers:

Schwarz R., Schwope A. D., Staude A. : *Photometry of the low accretion rate polar HS 1023+3900*, A&A, 374, 189 (2001)

Staude A., Schwope A. D., Schwarz R. : *System parameters of the long-period polar V 1309 Ori*, A&A, 374, 588 (2001)

Schwope A. D., Thomas H.-C., Häfner R., Mantel K.-H., Staude A. : *Cyclotron spectroscopy of HU Aquarii*, A&A, 402, 201 (2003)

Staude A., Schwope A. D., Krumpe M., Hambaryan V., Schwarz R. : *1RXS J062518.2+733433: A bright, soft intermediate polar*, A&A, 406, 253 (2003)

Hambaryan V., Staude A., Schwope A. D., Scholz R.-D., Kimeswenger S., Neuhäuser R. : *A new strongly X-ray flaring M9 dwarf in the solar neighborhood*, A&A, 415, 265 (2004)

Schwope A. D., Staude A., Vogel J., Schwarz R. : *Indirect imaging of polars*, AN, 325, 197 (2004)

Conference proceedings:

Schwope A. D., Schwarz R., Staude A., Heerlein C., Horne K., Steeghs D.: *Tomography of Polars*, Annapolis Workshop on Magnetic Cataclysmic Variables, ASP Conference Series, Vol. 157. Edited by K. Mukai and C. Hellier, p. 71 (1999)

Friedrich S., Schwarz R., Schwope A. D, Staude A., Geckeler R., Staubert R.: *Doppler-mapping of the Asynchronous Polars BY Cam and V1432 Aql*, Astronomische Gesellschaft Abstract Series, Vol. 17. Abstracts of Contributed Talks and Posters presented at the Annual Scientific Meeting of the Astronomische Gesellschaft at Bremen, September, 18-23, 2000. (2001)

Schwope A. D., Brunner H., Hambaryan V., Schwarz R., Staude A., Szokoly G., Hagen H.-J.: *LARPs - Low-Accretion Rate Polars*, The Physics of Cataclysmic Variables and Related Objects, ASP Conference Series, Vol. 261. Edited by B. T. Gänsicke, K. Beuermann, and K. Reinsch., p. 102 (2002)

Schwarz R., Hedelt P., Rau A., Staude A., Schwope A. D.: *Tomography of AM Herculis*, The Physics of Cataclysmic Variables and Related Objects, ASP Conference Series, Vol. 261. Edited by B. T. Gänsicke, K. Beuermann, and K. Reinsch., p. 167 (2002)

Gänsicke B. T., Hagen H.-J., Kube J., Schwarz R., Staude A., Engels D., Nogami D., Kuduz M.: *HS 0455+8315: A new eclipsing novalike variable*, The Physics of Cataclysmic Variables and Related Objects, ASP Conference Series, Vol. 261. Edited by B. T. Gänsicke, K. Beuermann, and K. Reinsch, p. 623 (2002)

Staude A., Schwarz R., Schwope A. D., Rau A.: *Photometry with the Potsdam 70cm-telescope*, The Physics of Cataclysmic Variables and Related Objects, ASP Conference Series, Vol. 261. Edited by B. T. Gänsicke, K. Beuermann, and K. Reinsch, p. 680 (2002)

Schwope A. D., Hambaryan V., Staude A., Schwarz R., Kanbach G., Steinle H., Schrey F., Marsh T., Dhillon V., Osborne J., Wheatley P., Potter S.: *Multiwavelength observations of eclipsing polars*, Magnetic Cataclysmic Variables, ASP Conference Series, Vol. 315. Edited by S, Vrielmann and M. Cropper, p. 92 (2004)

Staude A., Schwope A.D., Hedelt P., Rau A., Schwarz R.: *Tomography of AM Her and QQ Vul*, Magnetic Cataclysmic Variables, ASP Conference Series, Vol. 315. Edited by S, Vrielmann and M. Cropper, p. 251 (2004)

Acknowledgements

In the first place I would like to thank Axel Schwope for being my supervisor during all these years. Without his inspiration and his support I would have never come so far.

I want to thank Prof. Erwin Sedlmayr for being referee of this work, and Prof. A. Hese for being the chairman of the 'Promotionsausschuß'.

Many thanks to Robert Schwarz, who shared a room with me for many years, and who helped me a lot since my first days at the AIP.

I further want to thank Justus Vogel for the fruitful exchange of knowledge and the nice time as room-mates, and all the other people who have been or are still working in the former X-ray group for the good collaboration.

And, last but not least, thanks to all the people working at the AIP for making it such an informal and enjoyable place.

The spectroscopic data presented here were observed by Arne Rau and Robert Schwarz and were partly reduced by the latter and Pascal Hedelt. Parts of the photometry were observed by Janina Werner and Jürgen Schmoll.

My work at the AIP was financially supported by the Deutsche Forschungsgemeinschaft (DFG) under grant SCHW536/20-1.